SPATIALLY-ADAPTIVE WAVELET-BASED TECHNIQUES FOR DESPECKLING OF SYNTHETIC APERTURE RADAR AND MEDICAL ULTRASOUND IMAGES

Mohammed Imamul Hassan Bhuiyan

A thesis
in
The Department
of
Electrical and Computer Engineering

Presented in Partial Fulfillment of the Requirements
For the Degree of Doctor of Philosophy
Concordia University
Montréal, Québec, Canada

September 2007

Your file Votre référence
ISBN: 978-0-494-31142-4
Our file Notre référence
ISBN: 978-0-494-31142-4

Abstract

Spatially-Adaptive Wavelet-based Techniques for Despeckling of Synthetic Aperture Radar and Medical Ultrasound Images

Mohammed Imamul Hassan Bhuiyan, Ph.D.

Concordia University, 2007

Synthetic aperture radar (SAR) and ultrasound imaging systems are widely used for applications in remote sensing and medical diagnosis, respectively. However, the SAR and ultrasound images get corrupted by speckle noise during the process of image generation. The presence of speckle gives these images a granular appearance, thus hampering the interpretation of the image and reducing the efficiency of the algorithms in performing tasks such as compression, segmentation and classification. Hence, it is crucial to reduce the speckle from the SAR and ultrasound images before performing analysis or processing of these images.

The objective of this thesis is to develop efficient wavelet-based methods for an improved reduction of the speckle from SAR and medical ultrasound images at a reduced computational cost. It is shown that the symmetric normal inverse Gaussian (SNIG) distribution is highly suitable for modelling the wavelet coefficients of the log-transformed reflectivity. Bayesian minimum mean absolute error, minimum mean squared error and maximum a posteriori estimators are developed using the SNIG PDFs. Fast and efficient techniques are introduced to estimate the model parameters from the noisy wavelet coefficients. A fast and efficient technique is presented to calculate the Bayesian minimum mean absolute error and minimum mean squared error estimators, while closed-form expressions are obtained for the Bayesian maximum a posteriori estimators. New methods of reduced complexity are proposed to incorporate the spatial dependencies of the wavelet coefficients with the Bayesian

estimation processes. Extensive simulations using synthetically-speckled, SAR and medical ultrasound images are carried out to study the performance of the proposed techniques and the results show that they perform better than several existing techniques in terms of the peak signal-to-noise ratio, speckle statistics, edge preservation index, structural similarity index, ability to suppress the speckle in the homogeneous regions and visual quality, without an undue increase in computational complexity.

Finally, it is shown that the SNIG PDF can also be used to advantage in developing an efficient method for the classical case of reducing the additive white Gaussian noise from natural images.

Acknowledgments

I would like to express my deep gratitude to my supervisors Dr. M. Omair Ahmad and Dr. M.N.S. Swamy for their guidance, encouragement and support during the span of this research. I am grateful to them for providing me the freedom and motivation to explore new areas of research and new ideas. I also want to thank them for spending so many hours with me in correcting and improving the writing of this thesis. The useful suggestions provided by the committee members are also deeply appreciated.

I want to acknowledge the financial support provided by Concordia University and NSERC, Canada, which was crucial for completing this research.

I wish to thank my colleagues in the Center for Signal Processing and Communication, Mr. S.M.M. Rahman, Mr. S. A. Fattah, Ms. Celia Shahnaz, Dr. Saad Boguezel, Mr. Awni Itradat, Mr. Muhammad Tariqus-Salam, Mr. Nikhil Gupta, Mr. Yan Wu, Mr. Rajeev Yadav, and Mr. Chao Wu for their friendship, fruitful suggestions and constant moral support.

Finally, I would like to express my gratefulness to my parents; without their patience, love and constant encouragement I would not have made it to this point.

Table of Contents

List of Tables

List of Figures

List of Acronyms

AWGN	:	Additive white Gaussian noise
BKF	:	Bessel-K form
CDF	:	Cumulative density function
DICOM	:	Digital imaging and communications in medicine
DWT	:	Discrete wavelet transform
DT-CWT	:	Dual tree complex wavelet transform
ENL	:	Equivalent number of looks
EM	:	Expectation maximization
FFT	:	Fast Fourier transform
GG	:	Generalized Gaussian
GSM	:	Gaussian scale mixture
i.i.d.	:	Independent and identically distributed
JPL	:	Jet propulsion laboratory
LMMSE	:	Linear minimum mean squared error
MAD	:	Median absolute deviation

ML	:	Maximum likelihood
MMAE	:	Minimum mean absolute error
MMSE	:	Minimum mean squared error
MAP	:	Maximum a posteriori
NASA	:	National aeronautics and space administration
PDF	:	Probability density function
PSNR	:	Peak signal-to-noise ratio
QMF	:	Quadrature mirror filter
SAR	:	Synthetic aperture radar
SA-WBMMAE	:	Spatially adaptive wavelet-based method using the Bayesian MMAE estimator
SA-WBMAP	:	Spatially adaptive wavelet-based method using the Bayesian MAP estimator
SABMAP	:	Spatially adaptive method using the Bayesian MAP estimator
SABMMSE	:	Spatially adaptive method using the Bayesian MMSE estimator
SNIG	:	Symmetric normal inverse Gaussian
SNR	:	Signal-to-noise ratio
SSIM	:	Structural similarity
SWT	:	Stationary wavelet transform

List of Symbols

$C(.)$	:	Cost function for the Bayesian estimators
$E(.)$	:	Expectation operator
(k, l)	:	Index of an image pixel
K_λ	:	Modified Bessel function of the second kind of order λ
L	:	Number of looks
M_h	:	The mean of a homogeneous region in a SAR image
(p, m)	:	Index of a wavelet coefficient
Q	:	Order of the Hermite polynomial
R	:	the ratio of the pixel values in the noisy and despeckled images
$sign(.)$	:	The sign of the arguement
V_h	:	The variance of a homogeneous region in a SAR image
$var(.)$	:	Variance operator
α	:	Shape parameter of the SNIG PDF
β	:	The edge preservation index
γ	:	The dispersion parameter of the Cauchy PDF
Γ	:	Gamma function

δ : Scale parameter of the SNIG PDF

ν : Parameter of the Maxwell PDF

σ : Standard deviation of the additive white Gaussian noise

σ_η : Standard deviation of the log-transformed speckle noise

σ_n : Standard deviation of the complex Gaussian random process

$\Theta(x)$: The wavelet function for the DWT

$\Phi(x)$: The scaling function for the DWT

$\psi(.)$: Digamma function

$\psi(i,.)$: Polygamma function of order i

ψ_l : The weight associated with the l-th root of the Hermite polynomial

ω_l : The l-th root of the Hermite polynomial

$*$: Convolution operator

Chapter 1

Introduction

1.1 Introduction

The use of digital images in applications ranging from personal archive to medical diagnosis and remote sensing for the exploration of earth and planetary resources, has now become widespread. A major problem regarding the use of digital images is the corruption of these images by noise during their acquisition and transmission. Among the various types of noise, speckle noise (which is a multiplicative noise) is prevalent in different imaging systems such as the synthetic aperture radar (SAR) and ultrasound [1].

The SAR is widely used in various applications for earth and planetary explorations, for example monitoring of agricultural crops and the effect of deforestation, search and rescue operations, and target detection. The reason for using a SAR imaging system is basically due to its ability to generate images of a wide area terrain irrespective of the weather conditions or the ambient illumination. In addition, with appropriate design, the SAR imaging systems can also be used to image the objects that are underneath the foliage and in some cases, even beneath the earth surface [2]. Speckle noise gets introduced in a SAR image due to the non-coherent

character of the backscattered signals, a consequence of having targets that are small in comparison to the wavelength of the radar signal. It is manifested in a SAR image in the form of a granular pattern, thus making it difficult for the human experts to interpret the image content, and diminishing the efficiency of the algorithms that are employed to perform various image processing tasks such as compression, segmentation and scene classification. Hence, reduction of the speckle noise is often required as a pre-processing step in practical applications involving the SAR images.

Ultrasound is a coherent imaging system like the SAR; however, it uses sound waves instead of microwaves, and is widely used to image muscles and internal organs of the human body for diagnostic purposes. The wide-scale popularity of the ultrasound among the clinicians as well as the patients is due to the various advantages such as non-invasiveness, harmlessness to the human body, cost-effectiveness, reliability, accuracy and portability, that it offers. The speckle noise appears in a ultrasound image, when the scale of the objects (such as liver and kidney) is too small to be resolved by the sound waves having a large wavelength. The speckle noise reduces the contrast of the ultrasound images and obscures diagnostically important details, thus hampering the process of clinical diagnosis. It has been reported that the speckle noise can reduce the ability of the clinicians to detect lesions by a factor of eight [3]. Besides, it reduces the efficiency of the algorithms for automatic processing of ultrasound images. Therefore, suppression of the speckle in ultrasound images is critical in enhancing the diagnostic ability of the clinicians.

1.2 Motivation

A number of methods have been proposed in the literature in order to reduce the speckle in SAR and medical ultrasound images in the spatial domain [4–14]. Although

these methods result in removing the speckle in the homogeneous regions, most of them do so at the expense of blurring the image details. In addition, the performance of these filters are, in general, dependent on the size and orientation of the window used for computing the values of the local statistics that are utilized in the filter functions. The speckle noise is often expressed with a multiplicative model, where the observed image is given by a product of the underlying reflectivity and speckle [15]. The multiplicative model is motivated by numerous observations that in the homogeneous regions of speckled images, the noise variance is a function of the sample mean, indicating that the noise variance is higher when the signal amplitude is higher [15]. The homomorphic scheme for filtering the speckle noise was introduced by Jain [16]. In this scheme, the speckle noise is first converted into an additive noise via a logarithmic transformation of the speckled image, and then Wiener filter is applied on the log-transformed image to reduce the additive noise. The resulting image is subjected to an exponential operation for obtaining an image with reduced speckle. However, this method blurs the important details of the image since the Wiener filter is essentially a low-pass filter. An important feature of the homomorphic approach is the possibility of using it as a general framework for speckle reduction by using more efficient filters in lieu of the Wiener filter.

Recently, the multi-scale wavelet transform has provided a major breakthrough in signal denoising [17–19]. The traditional Fourier transform is basically applicable for periodic signals. In contrast, many practical signals contain jumps and discontinuities. Digital images provide a good example of such a signal, since they contain homogeneous regions separated by edges and line structures. For such signals, the wavelet transform can provide a nearly-optimal sparse representation in the frequency domain. Compared to the traditional Fourier transform, the wavelet representation

requires a fewer number of coefficients due to the local oscillating property of the wavelet transform; large coefficients are generated for the wavelets overlapping the singularities, whereas small-valued coefficients are obtained for the non-overlapping wavelets. Various methods have been proposed in the literature based on an efficient exploitation of the sparsity of the wavelet transform coefficients for despeckling the SAR and medical ultrasound images. Among them, the simplest ones are based on using *ad hoc* thresholding of the wavelet coefficients within a homomorphic framework [20–26]. In general, these methods perform better than the spatial-domain filters. However, these methods depend on parameters such as the threshold that are selected on an *ad hoc* basis, and may provide images with bias in the homogeneous regions. In the past few years, wavelet shrinkage methods based on Bayesian formalism using a prior probability distribution function (PDF) to model the wavelet coefficients corresponding to the log-transformed reflectivity have been successfully applied for the reduction of speckle from SAR and medical ultrasound images [27–29]. However, none of the above methods take into consideration the dependencies of the wavelet coefficients, while it is known that by providing a spatial adaptation to account for these dependencies, a considerable improvement in the performance of the denoising methods can be obtained [30].

A number of spatially-adaptive methods have been proposed in the literature for despeckling SAR and medical ultrasound images [31–43]. Most of these methods are able to provide a sound despeckling performance, at the expense of being computationally intensive, while some of them [31–33] are dependent on parameters selected manually. The high computational complexity of [35] is essentially due to the fact that one has to find the parameters of a two-state Gaussian prior by using a time-consuming expectation-maximization (EM) algorithm. The methods in [36–39] incur

a high computational cost, since one has to obtain the parameters of the prior PDF for each noisy coefficient, and calculate the Bayesian maximum a posteriori (MAP) estimates of the noise-free coefficients using iterative numerical methods. Moreover, the methods in [36–38] produce over-smoothed images, since some of the signal-dominant coefficients are mistaken as that of the noise due to the signal-dependent nature of the noise and thereby, get unduly reduced in magnitudes. It should be mentioned that the methods [36–39] do not actually address the problem of reducing the speckle noise from the medical ultrasound images. Furthermore, the methods in [40], [42] require the estimation of the signal moments through a computationally exhaustive process, while the method in [43] is spatially not fully adaptive, since most of the coefficients are set to zero using the subband-adaptive Bayes-shrink threshold given in [44].

From the above discussion, one can see that there is a scope for further investigation of wavelet-based Bayesian techniques that provide an improved performance in speckle reduction without increasing the computational cost substantially. While for improving the performance, it is necessary to use a better model for the statistics of the wavelet coefficients, it is essential at the same time to develop efficient methods with reduced complexity for obtaining the model parameters and the Bayesian estimates, and to provide spatial adaptation towards the dependencies of the wavelet coefficients in order to reduce the computational time. Both these aspects, should therefore, be considered in developing efficient despeckling methods.

1.3 Scope and organization of the thesis

The objective of the proposed work is to develop new homomorphic spatially-adaptive wavelet-based non-*ad hoc* techniques that have the ability to reduce the speckle noise

from the SAR and medical ultrasound images with an improved performance, while at the same time being computationally less demanding. In order to investigate the suitability of employing the symmetric normal inverse Gaussian (SNIG) PDF in modelling the wavelet coefficients corresponding to the log-transformed reflectivity, studies are undertaken. Based on these studies, several spatially-adaptive despeckling methods are developed using these SNIG PDFs. Extensive simulations are carried out using synthetically-speckled images as well as SAR and medical ultrasound images to study the performance of the proposed methods, and compared the results to those of several existing techniques for despeckling. The thesis is organized as follows.

In Chapter 2, a new wavelet-based spatially adaptive method is proposed for speckle reduction from the SAR images, where a Cauchy PDF is used for modelling the wavelet coefficients of the log-transformed reflectivity image. An efficient and fast method is introduced for obtaining the Bayesian minimum mean absolute error (MMAE) and minimum mean squared error (MMSE) estimates of the noise-free coefficients, while a closed-form expression is obtained for the Bayesian MAP estimator. In addition, a method with a reduced complexity is presented to incorporate the dependencies of the wavelet coefficients with the Bayesian estimation processes.

In Chapter 3, we first show that the SNIG PDF, a generalized version of the Cauchy PDF, is a highly suitable prior for modelling the wavelet coefficients of the log-transformed reflectivity corresponding to the SAR images. Based on this, an improved method is developed by using the SNIG PDF, for despeckling the SAR images. The proposed method is a combination of a local linear MMSE (LMMSE) estimator with a Bayesian MMSE or MAP estimator. The Bayesian estimators are developed employing the SNIG PDF. A fast and efficient technique is proposed to estimate the parameters of the SNIG PDF from the noisy wavelet coefficients.

In Chapter 4, a detailed experimental study is carried out to demonstrate the effectiveness of the SNIG PDF as a prior for modelling the wavelet coefficients of the log-transformed reflectivity corresponding to medical ultrasound images. Based on the results of this study, a fast and efficient spatially-adaptive method using the SNIG PDF is proposed to despeckle the ultrasound images. A spatially-adaptive threshold is obtained using a Bayesian MAP estimator that is developed using the SNIG PDF. An efficient and fast technique is presented to estimate the SNIG parameters from the noisy wavelet coefficients.

An alternative simple and fast method for despeckling the ultrasound images is proposed in Chapter 5, where a Maxwell distribution is employed as a prior to model the noise coefficients to incorporate the heavy-tailed character of the log-transformed speckle noise. Using the assumed Maxwell prior in conjunction with a Gaussian PDF, for modelling the signal coefficients, a Bayesian MAP estimator is developed to denoise the coefficients corresponding to the log-transformed ultrasound images.

Since we assume that the log-transformed speckle noise is Gaussian distributed, the proposed methods can also be adapted to the classical case of reducing additive white Gaussian noise from natural images, and hence, a new and efficient spatially-adaptive wavelet-based method is provided in this regard in Chapter 6. A maximum likelihood (ML)-based technique is proposed to estimate the parameters of the SNIG PDF from the noisy wavelet coefficients.

Finally, some concluding remarks highlighting the contributions of the thesis and suggestions for future work are provided in Chapter 7.

Chapter 2

Despeckling of SAR Images Using Cauchy PDF

2.1 Introduction

SAR images are widely used in various remote sensing applications, such as surface surveillance, earth source monitoring, and mine detection. However, since these images are inherently corrupted by speckle noise, the interpretation of the image content becomes difficult and the efficiency of the algorithms in performing tasks such as compression and segmentation, is reduced. Hence, speckle reduction is a critical step in the processing of SAR images. As explained in Chapter 1, most of the wavelet-based despeckling methods suffer from shortcomings including the dependency on *ad hoc* parameters, over-smoothing of the image, and high computational complexity. In view of this, a spatially-adaptive method using a Cauchy PDF to model the wavelet coefficients of the log-transformed reflectivity, for despeckling the SAR images, is proposed in this chapter [45, 46]. Extensive simulations are carried out using synthetically-speckled images as well as SAR images, and the performance of the proposed method compared with that of several existing techniques. The chapter is organized as follows. Some preliminaries concerning the wavelet transform are provided in Section

2.2. Modelling of the wavelet coefficients using the assumed statistical priors is discussed in Section 2.3, and using these models a method for despeckling the SAR images is developed in Section 2.4. Simulation results are described in Section 2.5, and some conclusions provided in Section 2.6.

2.2 Some Preliminaries on the Wavelet Transform

In this section, a brief introduction to the multi-scale discrete wavelet transform is provided. A multi-scale decomposition of a one-dimensional signal $f(x)$ by the wavelet transform using the scaling function $\Phi(x)$, and the wavelet function, $\Theta(x)$, is given by [1]

$$f(x) = \sum_{v} c_{w_0}(v)\Phi_{w_0,v}(x) + \sum_{w=w_0}^{\infty}\sum_{v} b_w(v)\Theta_{w,v}(x) \tag{2.1}$$

where w_0 is an arbitrary scale, $c_{w_0}(v)$ and $b_w(v)$ represent the approximation and detail coefficients, respectively. The first sum in this equation uses the scaling function to provide an approximation of $f(x)$ at a particular scale w_0, whereas for each higher scale $w > w_0$, the second sum adds a finer resolution to the approximation part to supply an increasing detail [1]. The terms $\Phi_{w_0,v}(x)$ and $\Theta_{w,v}(x)$ are obtained as

$$\begin{aligned} \Phi_{w_0,v}(x) &= \sqrt{2^{-w_0}}\Phi(2^{-w_0}x - v) \\ \Theta_{w,v}(x) &= \sqrt{2^{-w}}\Theta(2^{-w}x - v) \end{aligned} \tag{2.2}$$

where Φ and Θ denote the scale function and the mother wavelet function, respectively. The approximation and detail coefficients are calculated as

$$\begin{aligned} c_{w_0}(v) &= \langle f(x), \Phi_{w_0,v}(x)\rangle \\ &= \int f(x)\Phi_{w_0,v}(x)\, dx \end{aligned} \tag{2.3}$$

$$b_w(v) = \langle f(x), \Theta_{w,v}(x) \rangle = \int f(x)\Theta_{w,v}(x)\, dx \tag{2.4}$$

In practice, one deals with the discrete samples of a continuous function. The wavelet expansion for M discrete samples of $f(x)$ is given by

$$f(x) = \frac{1}{\sqrt{M}} \sum_{v} W_\Phi(w_0, v) + \frac{1}{\sqrt{M}} \sum_{w=w_0}^{\infty} \sum_{v} W_\Theta(w, v)\Theta_{w,v}(x) \tag{2.5}$$

The coefficients $W_\Phi(w_0, v)$ and $W_\Theta(w, v)$ corresponding to the discrete wavelet transform of $f(x)$ are obtained as

$$W_\Phi(w_0, v) = \frac{1}{\sqrt{M}} \sum_{x} f(x)\Phi_{w_0,v}(x) \tag{2.6}$$

$$W_\Theta(w, v) = \frac{1}{\sqrt{M}} \sum_{x} f(x)\Theta_{w,v}(x) \tag{2.7}$$

Mallat [47] has provided an efficient and fast algorithm for computing the discrete wavelet transform coefficients, and a block diagram of this algorithm is shown in Fig. 2.1. The algorithm uses an iterated two-channel filter bank. The two filters h_ϕ and h_θ form a quadrature mirror filter (QMF) bank. The output coefficients of the low-pass filter are called the approximation coefficients, while those of the high-pass filter the detail coefficients. The coefficients at a particular scale w are calculated as

$$W_\Phi(w, v) = h_\phi(-t) * W_\Phi(w + 1, t), \quad t = 2v, \; v \geq 0 \tag{2.8}$$

$$W_\Theta(w, v) = h_\theta(-t) * W_\Theta(w + 1, v), \quad t = 2v, \; v \geq 0 \tag{2.9}$$

Note that $h_\phi(t) = h_\theta(-t)$. A subsampling by a factor of 2 is performed at each level of the decompositions in order to keep the number of coefficients constant and equal to the length of the signal being decomposed throughout the whole decomposition

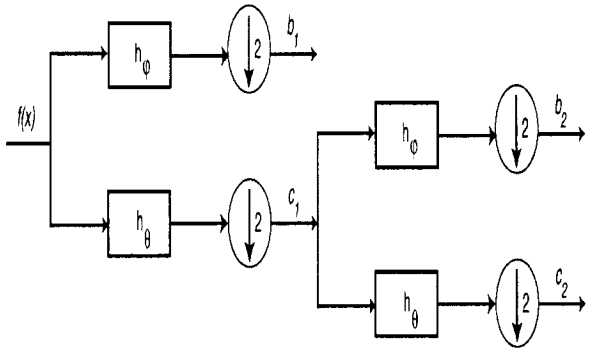

Figure 2.1: Wavelet subbands with 3-level decomposition of a 1-D signal

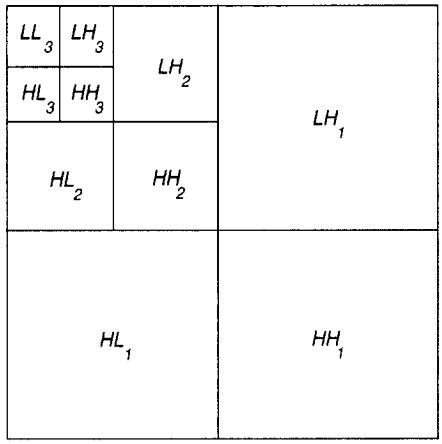

Figure 2.2: Wavelet subbands with 3-level decomposition of a 2-D signal

scheme. A two-dimensional extension of the Mallat's algorithm is straightforward. At each decomposition level, the signal is decomposed along the row and column directions by using low-pass and high-pass filters alternately. At any decomposition level q, the input to the algorithm generates four subbands: an approximation subband LL_q, and three detail subbands LH_q, HL_q and HH_q that are called the horizontal, vertical and diagonal subbands, respectively, which provide information about the signal features in the corresponding directions. The approximation subband LL_q is used to obtain the subbands at level $q+1$. Thus, the decomposition of an input up to a level q generates one approximation subband and $3q$ detail subbands. Fig. 2.2 shows a 3-level decomposition of a 2-D signal.

2.3 Modelling of the Wavelet Coefficients

Let $y(k,l)$ denote the (k,l)-th pixel in a SAR image of intensity format, $s(k,l)$ the corresponding reflectance, and $n(k,l)$ the multiplicative speckle component. Assuming the speckle to be fully developed, $y(k,l)$ is expressed as [16]

$$y(k,l) = s(k,l)n(k,l) + n_a(k,l) \tag{2.10}$$

where n_a represents additive noise (such as thermal noise). Since the additive noise is negligible compared to the multiplicative part [29], we can ignore it and (2.10) becomes

$$y(k,l) = s(k,l)n(k,l) \tag{2.11}$$

It should be noted that the speckle noise n is uncorrelated and independent of y, and follows a particular PDF depending on the type of the SAR image. The intensity-format image is obtained by taking the squared magnitude of the complex backscattered signal [48]. For an L-look SAR image in the intensity format (obtained by averaging L independent intensity-format images of the same scene), the PDF of the speckle noise has a gamma distribution given by

$$P_I(n) = \frac{L^L n^{L-1} e^{-Ln}}{\Gamma(L)} \tag{2.12}$$

with $E(n) = 1$ and $var(n) = 1/L$, $E(.)$ and $var(.)$ being the expectation and variance operators, respectively [48].The image in amplitude format can be obtained by square root of the corresponding image in intensity format. The speckle noise in an amplitude-format image can be obtained as

$$\begin{aligned} P_A(n) &= 2nP_I(n^2) \\ &= \frac{2L^L n^{2L-1} e^{-Ln^2}}{\Gamma(L)} \end{aligned} \tag{2.13}$$

Note that (2.13) is basically the Nakagami distribution whose mean is 1 and the variance is given by $\frac{4-\pi}{\pi L}$ [49]. With the log-transformation, (2.11) becomes

$$Y(k,l) = X(k,l) + N(k,l) \tag{2.14}$$

where $Y = \ln(y)$, $X = \ln(s)$ and $N = \ln(n)$. The mean and variance of N for an intensity-format image are $\psi(0,L) - \ln(L)$ and $\psi(1,L)$, respectively, where $\psi(i,.)$ denotes the i-th polygamma function [49]. For an amplitude-format image, the mean and variance of N are $\frac{1}{2}(\psi(L) - \ln(L))$, and $\frac{1}{4}\psi(1,L)$, respectively [49].

The discrete wavelet transform (DWT) of a two-dimensional image to a level J results in an approximation subband LL_J as well as $3J$ subbands LH_q, HL_q and HH_q with horizontal, vertical and diagonal orientations, respectively, where $q = 1, 2, \cdots, J$ [47]. The approximation subband contains the low-frequency portion of the image, and thus possesses most of the information of the image. On the other hand, the subbands LH_q, HL_q and HH_q respectively provide information about the horizontal, vertical and diagonal features in the image. Since the wavelet transform is a linear operation, after applying the DWT on (2.14), we obtain

$$g_q^i(p,m) = x_q^i(p,m) + \eta_q^i(p,m), \quad i = 1,2,3 \tag{2.15}$$

where $g_q^i(p,m)$, $x_q^i(p,m)$, and $\eta_q^i(p,m)$ denote the (p,m)-th wavelet coefficient, at level q with orientation i, of the log-transformed SAR image, the corresponding log-transformed reflectance and the corresponding speckle noise component, respectively. The values 1, 2, and 3 for i correspond to the horizontal, vertical and diagonal orientations, respectively. For notational simplicity, the subscripts will be dropped, and we will use g, x and η in subsequent discussions.

It has been shown by Mallat [47] that, in general, the distribution of the wavelet image coefficients is non-Gaussian, symmetric, and sharply peaked around zero with

heavy tails. Achim *et al.* [29] have demonstrated that the distribution of the wavelet coefficients of the log-transformed reflectance can be quite accurately described by a symmetric alpha-stable PDF. However, the alpha-stable PDF does not have a closed-form expression. This hampers the estimation of the alpha-stable parameters from noisy data [50], and makes it impossible, even approximately, to obtain a closed-form expression for the Bayesian estimator. In addition, the lack of a closed-form expression for the PDF increases the complexity of obtaining the Bayesian estimates numerically. It may be noted that there are two special cases of the alpha-stable PDF that have closed-form expressions, namely, the Gaussian and Cauchy PDFs. The Gaussian PDF is obviously not suitable for describing the distribution of the wavelet image coefficients. On the other hand, the Cauchy PDF is unimodal and symmetric, having a sharp peak around zero with heavy tails. Thus, in this chapter, the Cauchy PDF given by

$$P_x(x) = \frac{1}{\pi}\frac{\gamma}{\gamma^2 + x^2} \tag{2.16}$$

where γ is the dispersion parameter, is adopted as a simple prior for modelling the wavelet coefficients of the log-transformed reflectance image. It is to be noted that the Bayesian estimation in the wavelet domain with the Cauchy prior has been shown to provide an effective reduction of speckle in SAR images [45]. Note that the Cauchy PDF requires the estimation of the dispersion parameter only.

Several authors have shown that the distribution of the log-transformed speckle can be well-approximated by a Gaussian distribution [49,51]. Hence, the log-transformed speckle noise is assumed to be additive white Gaussian noise (AWGN) with a zero mean and a standard deviation of σ_η. Note that the log-transformed speckle noise remains zero-mean white Gaussian with the same standard deviation in the wavelet

domain due to the orthogonality of the DWT. The corresponding PDF is given by

$$P_\eta(\eta) = \frac{1}{\sqrt{2\pi}\sigma_\eta} \exp(-\eta^2/2\sigma_\eta^2) \tag{2.17}$$

2.4 Proposed Method for Despeckling

In this section, we describe the proposed spatially adaptive wavelet-based method for suppressing the speckle in SAR images. The proposed method utilizes a Bayesian MMAE estimator or a Bayesian MAP estimator, with spatial adaptation towards the dependency of the wavelet coefficients. Both the estimators are developed using the Cauchy PDF. The Bayesian MMAE and MAP estimators are described below.

2.4.1 The Bayesian MMAE and MAP Estimators

The Bayesian estimate is obtained by minimizing the Bayes risk function given by [52]

$$\mathcal{R}(x|g) = \int C[\widehat{x}(g), x] P_{x|g}(x|g) dx \tag{2.18}$$

The Bayesian estimate is obtained as

$$\widehat{x}(g) = \arg\min_{\widehat{x}} \int C[\widehat{x}(g), x] P_{x|g}(x|g) dx \tag{2.19}$$

where the right side of (2.19) is the cost averaged over the conditional distribution of x given g, $P_{x|g}(x|g)$, and $C(.)$ is the cost function. The Cauchy distribution has no finite second order moments. An MMAE estimator is obtained by using the absolute error cost function $|\widehat{x}(g) - x|$ for $C[\widehat{x}(g), x]$ in (2.19). The MMAE estimator can be shown to be a conditional median of x given g [52]. However, the conditional PDF, $P_{x|g}(x|g)$, is symmetric around zero for the assumed prior and hence, the conditional median of x coincides with its conditional mean. The resulting Bayesian estimator is given by

$$\widehat{x}(g) = \int x P_{x|g}(x|g).dx \tag{2.20}$$

Using Bayes' theorem, (2.20) can be written as

$$\begin{aligned}\widehat{x}(g) &= \int x P_{x|g}(x|g)dx \\ &= \frac{\int P_{g|x}(g|x)P_x(x)xdx}{P_g(g)} \\ &= \frac{\int P_{g|x}(g|x)P_x(x)xdx}{\int P_{g|x}(g|x)P_x(x)dx} \\ &= \frac{\int P_\eta(g-x)P_x(x)xdx}{\int P_\eta(g-x)P_x(x)dx}\end{aligned} \tag{2.21}$$

Using the definition of convolution, (2.21) can be written as

$$\widehat{x}(g) = \frac{P_\eta(g) * F(g)}{P_\eta(g) * P_x(g)} \tag{2.22}$$

where $F(x) = xP_x(x)$, and $*$ denotes the convolution operator. Thus, instead of employing direct numerical integration for each coefficient, the Bayesian MMAE estimates of the coefficients of a subband are obtained using the following steps.

1. Let g_{min} and g_{max} denote the minimum and maximum values of the subband, respectively. We define h as

$$h = \frac{g_{max} - g_{min}}{N_b} \tag{2.23}$$

   where $N_b = \sqrt{sz_{sub}}$, sz_{sub} being the number of coefficients in the subband.

2. Obtain the values of $\widetilde{g}_{k_s}$, defined as $\widetilde{g}_{k_s} = g_{kmin} + k_s h$, where $g_{kmin} = g_{min} + h/2$ and $k_s = 0, 1, \cdots, N_b - 1$.

3. Obtain the vector $\eta_g = [\eta_g^1, \eta_g^2, \cdots, \eta_g^{k_s}, \cdots]$, where $\eta_g^{k_s} = P_\eta(g)|_{g=\widetilde{g}_{k_s}}$.

4. Form the vector $\mathbf{x}_g = [x_g^1, x_g^2, \cdots, x_g^{k_s}, \cdots]$, where $x_g^{k_s} = P_x(x)|_{x=\widetilde{g}_{k_s}}$.

5. Obtain the vector $\mathbf{F}_g = [F^1, F^2, \cdots, F^{k_s}, \cdots]$, where $F^{k_s} = F(x)|_{x=\widetilde{g}_{k_s}}$.

6. Obtain the vector $\widetilde{\mathbf{x}} = [\widetilde{x}_1, \widetilde{x}_2, \cdots, \widetilde{x}_{k_s}, \cdots]$ using

$$\widetilde{\mathbf{x}} = (\mathbf{F} * \eta_g)./(\mathbf{x}_g * \eta_g) \tag{2.24}$$

where ./ denotes element-wise division.

7. For any arbitrary g, where $g \in [\widetilde{g}_{k_s-1}, \widetilde{g}_{k_s}]$, the corresponding Bayesian estimate $\widehat{x}$ is obtained using the cubic spline interpolation method [53] and the value of $\widetilde{x}_{k_s}$, the k_s-th element of $\widetilde{\mathbf{x}}$.

Note that the convolution operation is carried out at a limited number of points using the fast Fourier transform (FFT) algorithm [53], thus reducing the computational effort in obtaining the MMAE estimates.

The Bayesian MAP estimate is obtained using the cost function given by $C[\widehat{x}(g), x] = 1$ in (2.19) for $|\widehat{x}(g) - x| > \Delta$ and 0 otherwise, where $\Delta > 0$. The MAP estimate is expressed as

$$\widehat{x}(g) = \arg\max P_{x|g}(x|g) \tag{2.25}$$

Using Bayes' theorem, (2.25) becomes

$$\begin{aligned} \widehat{x}(g) &= \arg\max P_{x|g}(x|g) \\ &= \arg\max \frac{P_{g|x}(g|x).P_x(x)}{P_g(g)} \\ &= \arg\max P_{g|x}(g|x)P_x(x) \\ &= \arg\max P_\eta(g-x)P_x(x) \end{aligned} \tag{2.26}$$

The MAP estimate is obtained by differentiating the logarithm of the argument in (2.26), and setting the derivative to zero:

$$\frac{\partial}{\partial x}[-\frac{(g-x)^2}{2\sigma_\eta^2} + \ln P_x(x)] = 0 \tag{2.27}$$

which results in

$$\frac{x-g}{\sigma_\eta^2} + p'(x) = 0 \tag{2.28}$$

where $p(x) = -\ln P_x(x)$ and $p'(x) = \frac{\partial}{\partial x}p(x)$. A first-order approximation of the MAP estimator is given by [54]

$$\widehat{x} = g - \sigma_\eta^2 p'(g) \tag{2.29}$$

where $p'(x)$ is the derivative of $p(x) = -\ln P_x(x)$. The drawback with the first-order approximation in (2.29) is that the sign of $\widehat{x}$ can be different from that of g, since $p'(g)$ is highly discontinuous near zero. To overcome this problem of over-shrinkage, the following approximate solution for the MAP estimator has been proposed in [54]

$$\widehat{x}(g) = sign(g)\max(|g| - \sigma_\eta^2|p'(g)|, 0) \tag{2.30}$$

With the assumed Cauchy prior, we have $|p'(g)| = |\frac{2g}{\gamma^2+g^2}|$. Thus, we obtain

$$\widehat{x}(g) \;=\; sign(g)\max(0, |g| - \sigma_\eta^2|\frac{2g}{\gamma^2+g^2}|) \tag{2.31}$$

In order to obtain the Bayesian estimates, we need to estimate the parameters γ and σ_η from the noisy coefficients. A computationally simple method has been proposed in [45] for estimating the parameter γ of the Cauchy prior by minimizing

$$\int_{-\infty}^{\infty} |\widehat{\phi}_g(\omega) - \phi_g(\omega)| \exp(-\omega^2)\ d\omega \tag{2.32}$$

where $\widehat{\phi}_g(\omega)$ is the empirical characteristic function corresponding to g, given by

$$\phi_g(\omega) = \phi_x(\omega)\phi_\eta(\omega) \tag{2.33}$$

where

$$\phi_x(\omega) \;=\; \exp(-\gamma|\omega|) \tag{2.34}$$

$$\phi_\eta(\omega) \;=\; \exp(-\frac{\sigma_\eta^2}{2}|\omega|^2) \tag{2.35}$$

The integral in (2.32) is then calculated using the Gauss-Hermite quadrature [53] as

$$\int_{-\infty}^{\infty} \lambda(\omega) \exp(-\omega^2) d\omega \simeq \sum_{l=1}^{l=Q} \psi_l \lambda(\omega_l) \tag{2.36}$$

where $\lambda(\omega) = \widehat{\phi}_g(\omega) - \phi_g(\omega)$, ω_l's are the roots of the Hermite polynomials of order Q, and ψ_l's are the weights associated with these roots. Note that as a consequence of (2.36), the computational complexity for estimating the dispersion parameter is reduced, since the empirical characteristic function is evaluated at a limited number of points. The standard deviation of the log-transformed noise is obtained as [55]

$$\sigma_\eta = \frac{MAD(g(p,m))}{0.6745} \qquad g(p,m) \in HH_1 \tag{2.37}$$

where MAD denotes the median absolute deviation operation.

2.4.2 Incorporation of Spatial Dependence

Both the Bayesian MMAE and MAP estimators assume that the wavelet coefficients are mutually independent. However, the magnitudes of the wavelet coefficients are known to show dependency within the subband as well as across the subbands [30], [56]. Hence, the Bayesian estimators shrink the coefficients without providing any spatial adaptation towards such dependency. In several image coding methods [56], [57], the statistical model of a wavelet coefficient is conditioned on its contextual neighbors. In [56], the dependencies of the wavelet coefficients (both intra-scale and inter-scale) are characterized by a linear predictor of the magnitude of the coefficients residing in a contextual neighborhood comprising adjacent coefficients within the same subband as well as the cousin and parent coefficients. Note that the absolute values or the squared magnitudes of the neighboring coefficients are correlated, and hence, they are useful for providing contextual information [58]. On the other hand, wavelet coefficients, being approximately uncorrelated [56], do

not provide much information about the context. However, Liu and Moulin [30] have observed that the dependency is mostly intra-scale and the additional incorporation of the inter-scale dependency provides a marginal gain in denoising.

In this chapter, we propose a method with reduced complexity to incorporate the intra-scale dependency of the wavelet coefficients with the Bayesian shrinkage process. Let $g(p,m)$ represent the (p,m)-th wavelet coefficient in a subband. The corresponding denoised coefficient obtained via the Bayesian estimator is denoted by $\widehat{x}(p,m)$. The associated shrinkage value $F(p,m)$ is obtained as $\widehat{x}(p,m)/g(p,m)$. In the proposed method, the shrinkage factors of the neighbors of the coefficient $\widehat{x}(p,m)$, within a $D \times D$ neighborhood that have the same sign as $F(p,m)$ are used to form the vector $\mathbf{S}$. The linear predictor of the magnitude of the coefficient $\widehat{x}(p,m)$ can be obtained as $|\widehat{x}(p,m)|_{predicted} = \sum_P W_P C_P$, where C_P and W_P are the P-th element of a $d_c \times 1$ vector $\mathbf{V}$ comprising the amplitudes of the coefficients corresponding to $\mathbf{S}$, and the $d_c \times 1$ weight vector $\mathbf{W}$, respectively [56]. The maximum value of d_c is $D^2 - 1$. The weight vector $\mathbf{W}$ is obtained by minimizing the squared error, i.e., $(|\widehat{x}(p,m)| - \sum_P W_P C_P)^2 = (|\widehat{x}(p,m)| - \mathbf{W}^T\mathbf{V})^2$, where T is the transpose operation. By differentiating the squared error with respect to $\mathbf{W}$ and setting the derivative to zero, we get

$$\mathbf{W} = (\mathbf{V}\mathbf{V}^T)^{-1}\mathbf{V}|\widehat{x}(p,m)| \tag{2.38}$$

The modified shrinkage value $\widetilde{F}(p,m)$ is obtained as

$$\widetilde{F}(p,m) = \frac{\rho \sum_R S_R W_R}{\sum_R W_R} + (1-\rho)F(p,m) \tag{2.39}$$

where S_R and W_R are the R-th element of $\mathbf{S}$ and $\mathbf{W}$, respectively, and ρ is a weighting factor $(0 < \rho < 1)$. The denoised wavelet coefficient is now obtained as

$$\widetilde{x}(p,m) = \widetilde{F}(p,m)g(p,m) \tag{2.40}$$

Note that in [35], the shrinkage values are modified using the optimal hidden states of the wavelet coefficients obtained through a computationally intensive iterative process. The probability of each coefficient having a particular state is maximized. A single cycle of the iterative process consists of maximizing the states for all the coefficients in a subband carried out sequentially. Several cycles are needed for obtaining the optimal hidden states of the coefficients. However, in the proposed method, the shrinkage value of a wavelet coefficient is modified using weights obtained from a closed-form expression that requires the inversion of a small-sized matrix whose maximum size is 8×8, (assuming $D = 3$), thus reducing the corresponding computational complexity. Since most of the noise power is concentrated in the fine scales, namely, the subbands at levels 1 and 2 [59], the modification of the Bayesian estimates is carried out in these subbands only. The values of ρ in (2.39) are set to 0.6 and 0.5 for the subbands at levels 1 and 2, respectively.

2.4.3 Summary of the Proposed Method

In order to get the despeckled image, an exponential operation is performed on the inverse transform of the denoised coefficients obtained from (2.40). Since the mean of the log-transformed speckle noise is biased [49], an adjustment is needed to remove the associated mean-bias for avoiding radiometric distortion, especially for high noise levels [35]. The adjustment is carried out as

$$\begin{aligned} B &= A - \psi(0, L) - \ln(L) \quad \text{for the intensity-format image} \\ &= A - \frac{1}{2}(\psi(0, L) - \ln(L)) \quad \text{for the amplitude-format image} \end{aligned} \tag{2.41}$$

where A denotes the inverse transform of the denoised coefficients. The denoised image $\widehat{y}$ is obtained as $\widehat{y} = \exp(B)$. Note that we need to know the number of looks

(L) to carry out the adjustment. We propose to estimate L as

$$\begin{aligned} L &= \arg\min_{L}(\sigma_\eta^2 - \psi(1, L)) \quad \text{for the intensity-format image} \\ &= \arg\min_{L}(\sigma_\eta^2 - \frac{1}{4}\psi(1, L)) \quad \text{for the amplitude-format image} \end{aligned} \tag{2.42}$$

A block diagram of the proposed method for denoising a SAR image is shown in Fig. 2.3. The shift operator z^r means a positive shift of the log-transformed SAR image by r samples, whereas z^{-r} a negative shift by r samples. The shifting and unshifting operations correspond to the implementation of the proposed method in the cycle-spinning mode, explained later in Section 2.5. A summary of the proposed

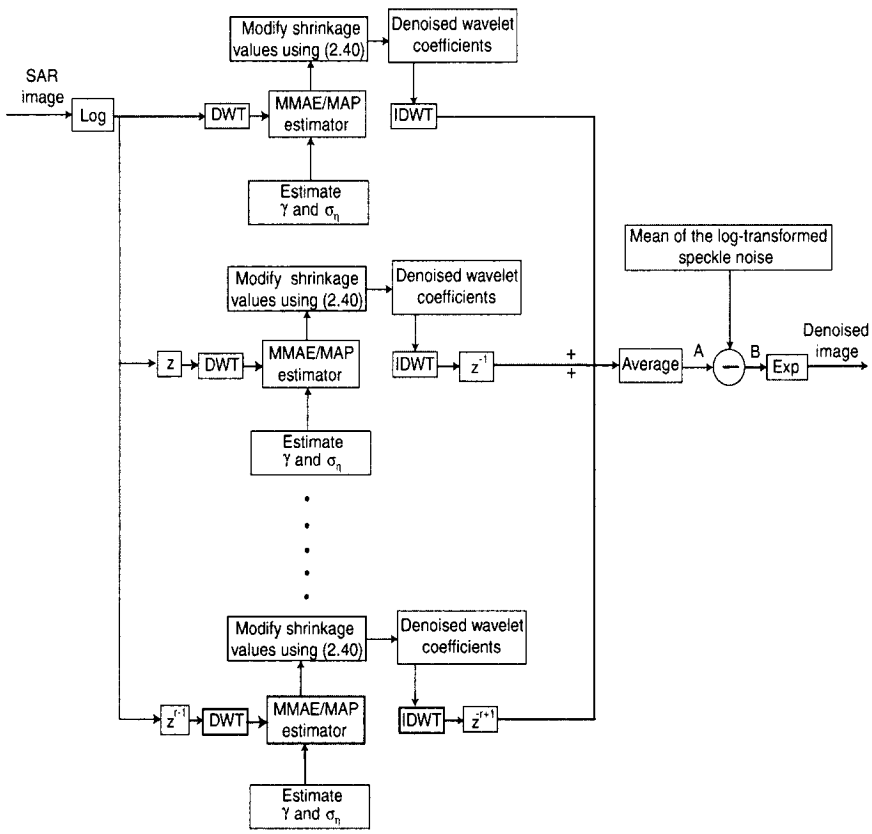

Figure 2.3: Block diagram of the proposed wavelet-based despeckling technique.

despeckling technique is also provided below.

1. Carry out the log-transformation of the SAR image.
2. Apply the DWT on the log-transformed image.
3. Estimate the parameters γ and σ_η using (2.32) and (2.37), respectively.
4. Obtain the estimates using the Bayesian MMAE estimator from (2.22) or the Bayesian MAP estimator from (2.31), and modify them using (2.40).
5. Perform the inverse-transform of the coefficients obtained in Step 4.
6. Subtract the mean of the log-transformed noise from the quantities achieved in Step 5.
7. Perform the exponential transformation of the values obtained in Step 6 to get the denoised image.

2.5 Simulation Results

Extensive simulations are carried out using synthetically speckled and SAR images to investigate the performance of the proposed method. The proposed spatially-adaptive wavelet-based method using the Bayesian MMAE and MAP estimators are referred to as SA-WBMMAE and SA-WBMAP schemes, respectively. The performances of the two schemes are compared with those of the methods of WIN-SAR [29], Fukuda and Hirosawa [31], WBDT [33], Zeng and Cummings [27], and Γ-MAP filter [11], referred to as WIN-SAR, FH, WBDT, ZC, and GMAP methods, respectively. Daubechies' *Symlet* wavelet [60] of order 8 is used for a 4-level decomposition of the images. For estimating the dispersion parameter γ, the value of Q in (2.36) is set to 20. It should

be noted that the DWT is not shift-invariant, resulting in 'specks' in smooth regions and 'ringing' around the edges [61]. However, the lack of the shift-invariance property associated with the DWT can be overcome by using the cycle-spinning technique [61]. It has been shown in [62] that by implementing the DWT-based denoising method in the cycle-spinning mode, a performance equivalent to those using the traditional redundant wavelet transforms, such as the stationary wavelet transform (SWT), can be achieved. Hence, the proposed method is implemented in the cycle-spinning mode with four shifts, where the noisy images are circularly shifted by zero, one, two and three pixels both in the horizontal and vertical directions. Next, these images are processed by the proposed despeckling technique, unshifted by the same number of pixels, and averaged to obtain the despeckled image. It should be mentioned that the parameter γ is estimated for the zero shift only. To ensure a fair comparison, the WIN-SAR, and ZC methods are also implemented in the cycle-spinning mode with the same number of shifts. A 5×5 square window is used in the GMAP method.

2.5.1 Synthetically-speckled Images

In order to study the performance of the proposed schemes in smoothing and edge preservation, two noise-free images, namely, *House* and *Boat* taken from [63] and [64], respectively, are used for generating the synthetically speckled images in intensity format. The images comprise 256×256 and 512×512 pixels, respectively, and are commonly used by the image processing community for evaluating the performance of wavelet-based denoising methods [35], [29]. A synthetically-speckled image is generated by multiplying a noise-free image with speckle noise simulated using (2.12). Five different values of L are considered in this chapter. It should be noted that the lower the value of L, the higher is the level of the noise. The performance criteria used are

the peak signal-to-noise ratio (PSNR), structural similarity index (SSIM) [65], and the statistics of the speckle noise described by the mean and variance of the ratio of the noisy image and the corresponding denoised image. For perfect despeckling, R, the ratio of the corresponding pixel values in the noisy and despeckled images should have a unit mean and a variance equal to $1/L$. The values of the various performance criteria are calculated by repeating the experiments four times that employ the same setting except for the speckle noise which is generated using different random seeds, but with the same distribution, and finally averaging the corresponding values. The PSNR is given by

$$PSNR = 10\log_{10}(\frac{255^2}{MSE}) \tag{2.43}$$

where the MSE is given by

$$MSE = \frac{1}{P \times M}\sum_{k=1}^{P}\sum_{l=1}^{M}(s_{k,l} - \widehat{s}_{k,l})^2 \tag{2.44}$$

and $s_{k,l}$, $\widehat{s}_{k,l}$ and $P \times M$ denote the (k,l)-th pixel of the noise-free image s, its denoised counterpart $\widehat{s}$, and dimension of the image, respectively. Table 2.1 shows the PSNR values (in dB) for the synthetically-speckled images. It can be observed from this table that, for all the images, the proposed SA-WBMMAE scheme provides PSNR values that are larger than those of the other methods, including that of the proposed SA-WBMAP. Table 2.2 illustrates that among all the methods, the value of the mean of R provided by the GMAP method is closest to unity. However, among the remaining methods, SA-WBMMAE provides a mean that is closest to unity. Note that a significant deviation from the unit mean is an indication of the radiometric distortion [48]. Table 2.3 shows the values of the variance of R provided by the different methods. The quantities in the parentheses are the actual values of the variance of R for the various values of L. It is seen that the values of the variance

Table 2.1: Values of PSNR for different images

Method \ L	3	4	5	6	7
House					
SA-WBMMAE	22.39	23.11	23.77	24.40	24.66
SA-WBMAP	20.91	21.88	22.72	23.58	24.01
WIN-SAR	21.48	22.52	23.42	24.19	24.61
WBDT	16.92	17.98	18.82	19.44	19.96
FH	12.53	14.53	16.16	17.66	18.84
ZC	16.95	17.99	18.93	19.72	20.16
GMAP	18.76	19.81	20.36	21.25	21.56
Boat					
SA-WBMMAE	23.65	24.26	24.81	25.12	25.46
SA-WBMAP	21.12	22.18	23.04	23.54	24.16
WIN-SAR	22.14	23.13	23.92	24.42	24.85
WBDT	16.84	17.93	18.75	19.41	19.95
FH	12.51	14.69	16.48	17.96	18.97
ZC	18.78	20.42	21.59	22.37	23.18
GMAP	19.06	20.01	20.77	21.36	21.75

provided by SA-WBMMAE are closer to the actual values than those of the other methods in most of the cases. Thus, in most cases, the proposed SA-WBMMAE scheme yields mean and variance of R that are closer to the actual values than those of the other methods.

Table 2.2: Mean values of R

Method \ L	3	4	5	6	7
House					
SA-WBMMAE	0.9865	0.9869	0.9875	0.9873	0.9877
SA-WBMAP	0.9601	0.9682	0.9731	0.9767	0.9784
WIN-SAR	0.9644	0.9750	0.9839	0.9854	0.9879
WBDT	0.9129	0.9292	0.9393	0.9462	0.9514
FH	0.9417	0.9513	0.9626	0.9599	0.9643
ZC	1.1219	1.0848	1.0630	1.0517	1.0426
GMAP	1.0042	1.0030	1.0022	1.0022	1.0015
Boat					
SA-WBMMAE	0.9971	0.9982	0.9975	0.9966	0.9972
SA-WBMAP	0.9635	0.9734	0.9783	0.9809	0.9833
WIN-SAR	0.9748	0.9803	0.9869	0.9920	0.9917
WBDT	0.9158	0.9321	0.9427	0.9491	0.9548
FH	0.9624	0.9560	0.9600	0.9582	0.9670
ZC	1.1590	1.1144	1.0862	1.0679	1.0599
GMAP	1.0067	1.0065	1.0058	1.0055	1.0053

Table 2.3: Values of variance of R

Method \ L	3	4	5	6	7
	(0.3333)	(0.2500)	(0.2000)	(0.1667)	(0.1429)
House					
SA-WBMMAE	0.3047	0.2271	0.1816	0.1490	0.1263
SA-WBMAP	0.2392	0.1833	0.1480	0.1254	0.1074
WIN-SAR	0.2906	0.2235	0.1800	0.1503	0.1300
WBDT	0.1179	0.0956	0.0811	0.0713	0.0641
FH	0.6643	0.3167	1.6173	0.0760	0.0542
ZC	0.3001	0.2029	0.1498	0.1237	0.1026
GMAP	0.2485	0.1845	0.1462	0.1218	0.1038
Boat					
SA-WBMMAE	0.3256	0.2451	0.1930	0.1589	0.1389
SA-WBMAP	0.2412	0.1855	0.1485	0.1233	0.1077
WIN-SAR	0.3052	0.2318	0.1856	0.1549	0.1340
WBDT	0.1201	0.1247	0.0835	0.0722	0.0653
FH	16.93	0.1132	0.0673	7.0154	0.0548
ZC	0.3800	0.2609	0.1901	0.1469	0.1286
GMAP	0.2463	0.1820	0.1435	0.1174	0.0999

It might be noted that the PSNR is not always a good indication of the visual quality [65]. Recently [65], the SSIM index which is based on measuring the structural similarity between a reference image and its distorted version (e.g., in our case, the despeckled image), has been proposed as a performance indicator, given by

$$SSIM = \frac{(2\mu_s\mu_{\widehat{s}} + C_1)(2\sigma_{s\widehat{s}} + C_2)}{(\mu_s^2 + \mu_{\widehat{s}}^2 + C_1)(\sigma_s^2 + \sigma_{\widehat{s}}^2 + C_2)} \tag{2.45}$$

where C_1 and C_2 are small positive constants and

$$\mu_s = \frac{1}{PM-1}\sum_{k=1}^{P}\sum_{l=1}^{M} s_{k,l} \tag{2.46}$$

$$\mu_{\widehat{s}} = \frac{1}{PM-1}\sum_{k=1}^{P}\sum_{l=1}^{M} \widehat{s}_{k,l} \tag{2.47}$$

$$\sigma_s^2 = \frac{1}{PM-1}\sum_{k=1}^{P}\sum_{l=1}^{M}(s_{k,l} - \mu_s)^2 \tag{2.48}$$

$$\sigma_{\widehat{s}}^2 = \frac{1}{PM-1}\sum_{k=1}^{P}\sum_{l=1}^{M}(\widehat{s}_{k,l} - \mu_{\widehat{s}})^2 \tag{2.49}$$

$$\sigma_{s\widehat{s}}^2 = \frac{1}{PM-1}\sum_{k=1}^{P}\sum_{l=1}^{M}(s_{k,l} - \mu_s)(\widehat{s}_{k,l} - \mu_{\widehat{s}}) \tag{2.50}$$

The SSIM index is reported to be a more reliable metric for assessing the visual quality, and has been used in the literature for comparing the performance of the different denoising algorithms in terms of the visual quality [66]. Hence, we compute the values of the SSIM for the various methods, and list the same in Table 2.4. It can be seen from this table that the proposed SA-WBMMAE scheme performs better than the other techniques in most of the cases, and especially so when the noise level is high. Figs. 2.4 and 2.5 show the noise-free *House* and *Boat* images and the corresponding noisy images for $L = 7$ as well as the despeckled images obtained using the various methods. It can be seen from these figures that SA-WBMMAE provides a despeckled

Table 2.4: Values of SSIM. The optimal value for the SSIM is 1.

Method \ L	3	4	5	6	7
House					
SA-WBMMAE	0.5100	0.5352	0.5532	0.5726	0.5788
SA-WBMAP	0.3952	0.4416	0.4743	0.5058	0.5269
WIN-SAR	0.4787	0.5232	0.5496	0.5790	0.5978
WBDT	0.2188	0.2543	0.2831	0.3083	0.3289
FH	0.1985	0.2424	0.2773	0.3064	0.3354
ZC	0.2812	0.3118	0.3360	0.3547	0.3724
GMAP	0.3644	0.3956	0.4252	0.4580	0.4726
Boat					
SA-WBMMAE	0.5969	0.6223	0.6401	0.6535	0.6707
SA-WBMAP	0.3972	0.4391	0.4775	0.5061	0.5324
WIN-SAR	0.5107	0.5544	0.5864	0.6089	0.6253
WBDT	0.2290	0.2617	0.2883	0.3112	0.3318
FH	0.2065	0.2457	0.2810	0.3097	0.3332
ZC	0.5066	0.5271	0.5402	0.5535	0.5857
GMAP	0.3682	0.4004	0.4298	0.4532	0.4791

image that is of better visual quality than those given by the other methods. It should be mentioned that compared to the proposed schemes, the WIN-SAR method is computationally intensive. For example, the average CPU time to process 256×256 images (in MATLAB) by the WIN-SAR method is 17.61 minutes, whereas the time taken by the SA-WBMMAE and SA-WBMAP are 47.91 secs and 56.54 secs, respectively. For a particular subband of size $S_x \times S_y$, the computational complexity of the SA-WBMMAE and SA-WBMAP schemes are roughly $O(S_k log_2 S_k) + O(S_k) + O(d_c^3 S_x S_y)$, and $O(S_x S_y) + O(d_c^3 S_x S_y)$, respectively, where the maximum value of d_c is 8 and $S_k = \sqrt{S_x \times S_y}$.

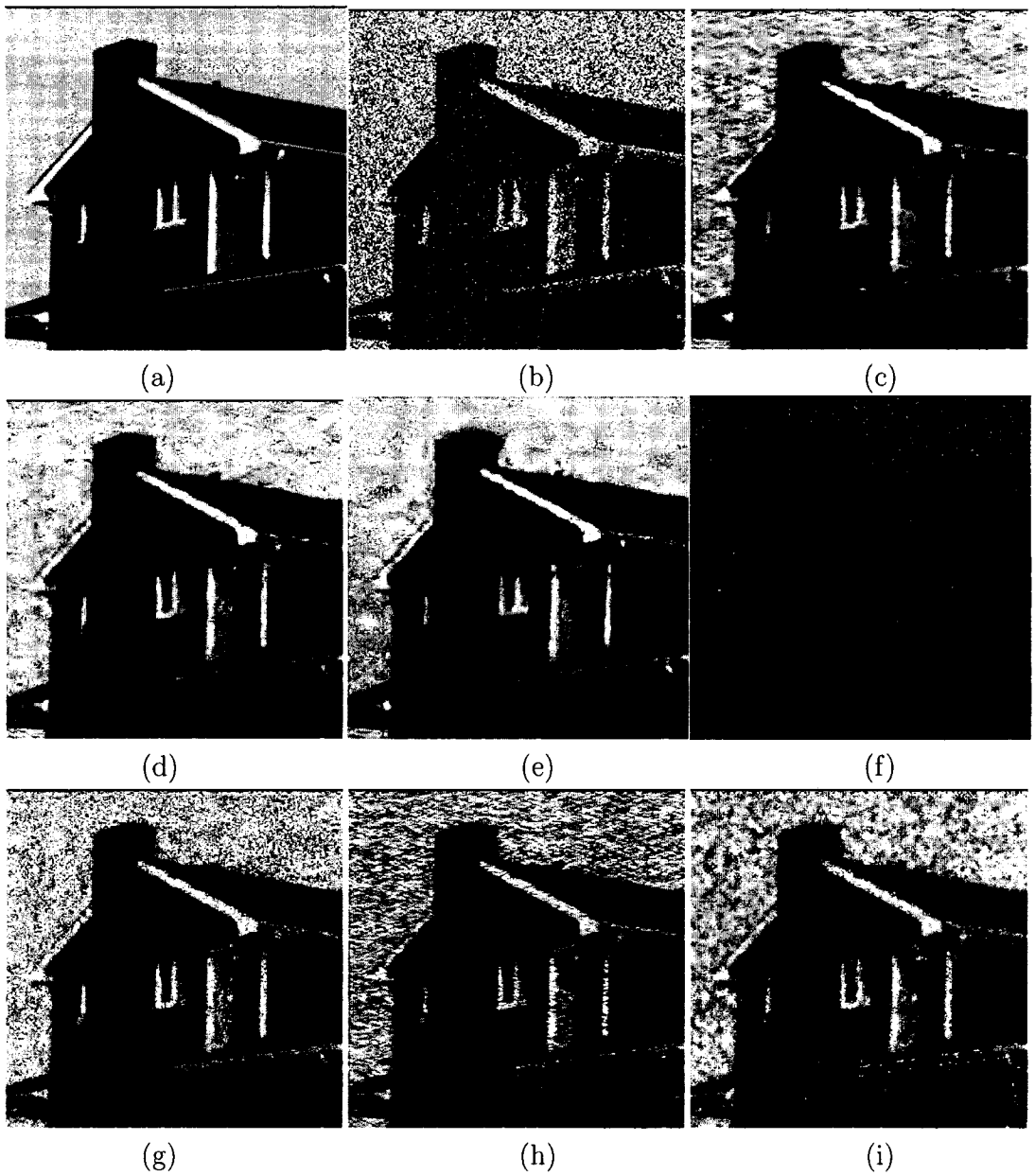

Figure 2.4: (a) noise-free *House* image. (b) noisy *House* image. Denoised images using (c) SA-WBMMAE, (d) SA-WBMAP, (e) WIN-SAR, (f) WBDT, (g) FH, (h) ZC, and (h) GMAP.

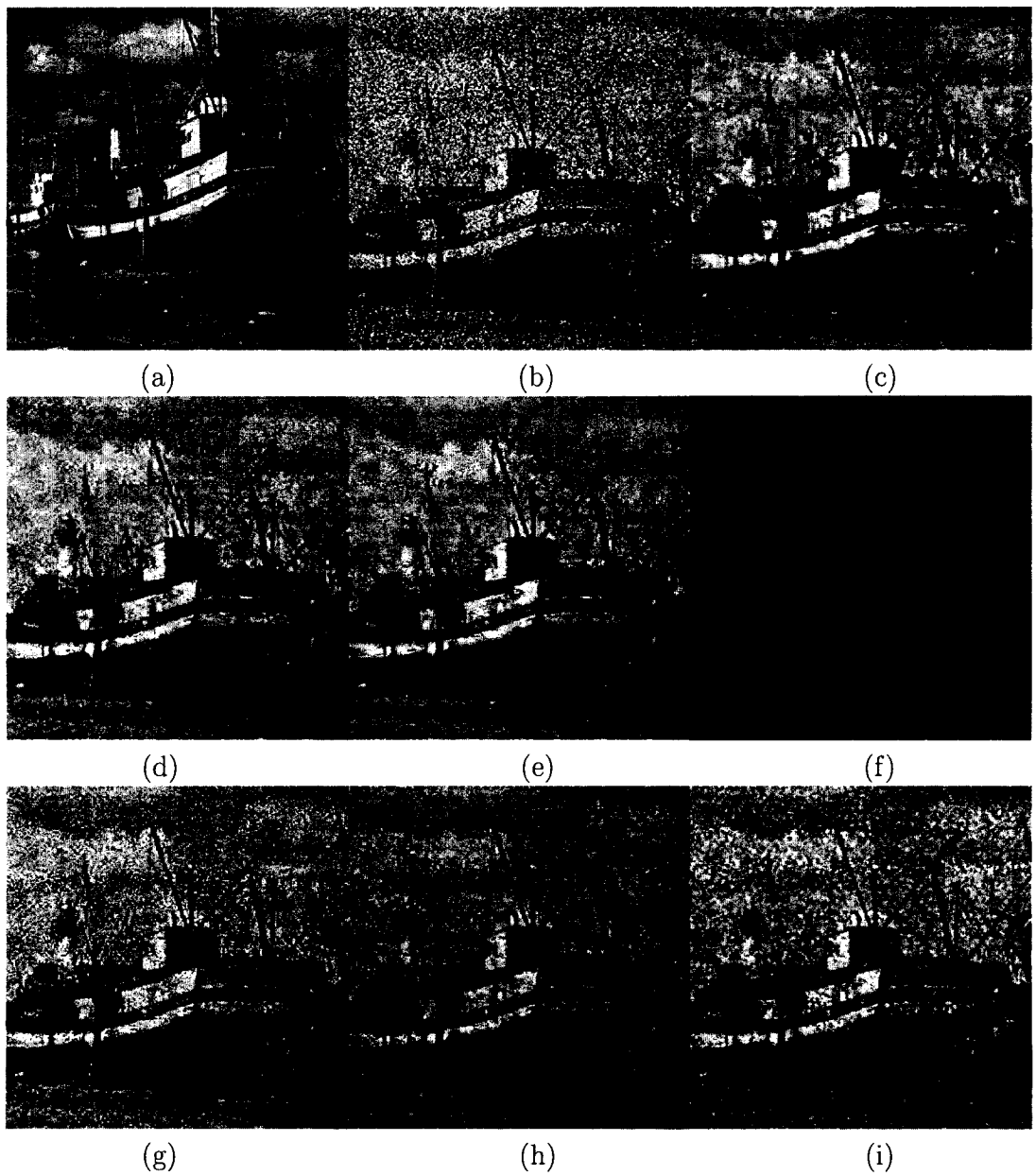

Figure 2.5: (a) noise-free *Boat* image. (b) noisy *Boat* image. Denoised images using (c) SA-WBMMAE, (d) SA-WBMAP, (e) WIN-SAR, (f) WBDT, (g) FH, (h) ZC, and (h) GMAP.

2.5.2 SAR Images

Three AIRSAR images from the NASA/Jet Propulsion Laboratory [67] taken over the *Cooktown*, *Collier*, and *Ajkwa* are used in our experiment. The three images are shown in Figs. 2.6 (a)-(c). The *Cooktown*, *Collier*, and *Ajkwa* images are of 366×364, 651×701, and 421×612 pixels, respectively. Since the noise-free images are not available, the values of the equivalent number of looks (ENL) and mean-bias are used for comparing the performance of the various methods. The ENL is used as an objective measure in the literature to assess the ability of a denoising method in reducing the speckle in the homogeneous regions. For the intensity-format image, the ENL is given by

$$\text{ENL} = \frac{M_h^2}{V_h} \tag{2.51}$$

whereas for the amplitude-format image the ENL is expressed as

$$\text{ENL} = \left(\frac{4}{\pi} - 1\right) \frac{M_h^2}{V_h} \tag{2.52}$$

where M_h and V_h represent the mean and variance computed using the pixels in a homogeneous region of the image [35]. For a particular homogeneous region, the value of the mean-bias is calculated as

$$\text{Mean-bias} = \frac{M_{hn} - M_{hd}}{M_{hn}} \times 100\% \tag{2.53}$$

where M_{hn} and M_{hd} represent the mean value of the region for the noisy image and its despeckled version, respectively. For the ENL calculation, two uniform areas, Regions 1 and 2, have been used in each SAR image (see Figs. 2.6 (a), 2.6 (b), and 2.6 (c)). These regions comprise 29×69 and 22×50 pixels for the *Cooktown*, 54×111 and 25×33 pixels for the *Collier*, and 28×139 and 59×33 pixels for the *Ajkwa*. The ENL values are listed in Table 2.5. It can be seen from this table that SA-WBMMAE

provides larger values of ENL in comparison to the other methods, thus indicating a better ability to suppress the speckle noise in the homogeneous regions. Zoomed-in section of the SAR images (the region within the broken lines in Fig. 2.6 (a)-(c)) and the corresponding zoomed-in sections of the despeckled images using the various methods are shown in Figs. 2.7, 2.8 and 2.9. It can be seen from these figures that SA-WBMMAE not only smooths the speckle noise better than the other techniques, but also retains the edges and line structures well. Although the GMAP method gives images with sharper edges, it introduces 'specks', an undesirable artifact, in the denoised images. Similar artifacts are also present in the despeckled image provided by the WIN-SAR method. Table 2.5 also shows that the mean in the homogeneous regions provided by the proposed method has very little bias.

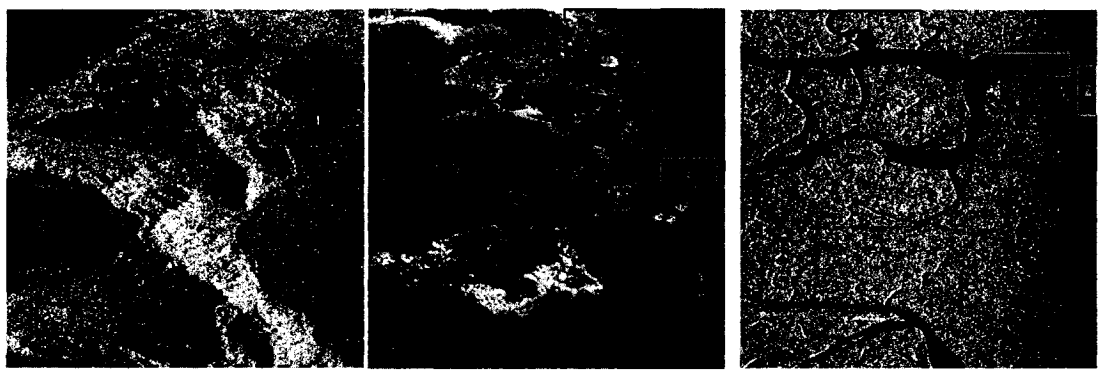

(a) (b) (c)

Figure 2.6: SAR images: (a) *Cooktown* (b) *Collier*, and (c) *Ajkwa*.

Table 2.5: ENL values for Regions 1 and 2 in Figs. 2.6 (a), (b), and (c)

	Region 1		Region 2	
	ENL	*Mean-bias*	ENL	*Mean-bias*
Cooktown				
Before Despeckling	9.10	–	8.16	–
SA-WBMMAE	111.69	0.18	143.44	1.07
SA-WBMAP	73.23	-0.01	77.46	0.71
WIN-SAR	89.43	-0.04	99.87	0.82
WBDT	31.84	0.46	36.69	-0.50
FH	44.85	0.11	43.68	-0.03
ZC	56.28	4.71	59.45	5.45
GMAP	67.23	0.96	71.79	1.44
Collier				
Before Despeckling	6.19	–	6.25	–
SA-WBMMAE	28.60	1.12	33.79	1.13
SA-WBMAP	23.55	0.82	25.39	-0.35
WIN-SAR	25.27	0.82	29.78	0.78
WBDT	10.71	-2.91	28.97	-3.186
FH	13.83	0.46	12.31	-4.85
ZC	22.77	5.79	26.81	5.37
GMAP	17.22	1.59	12.84	1.14
Ajkwa				
Before Despeckling	8.23	–	8.32	–
SA-WBMMAE	55.57	0.38	79.12	0.96
SA-WBMAP	45.40	0.15	55.89	0.48
WIN-SAR	51.16	0.15	65.22	0.48
WBDT	22.92	-9.86	18.68	-5.97
FH	24.36	-0.79	21.27	-2.90
ZC	40.81	4.67	49.18	5.12
GMAP	37.80	1.08	31.53	1.38

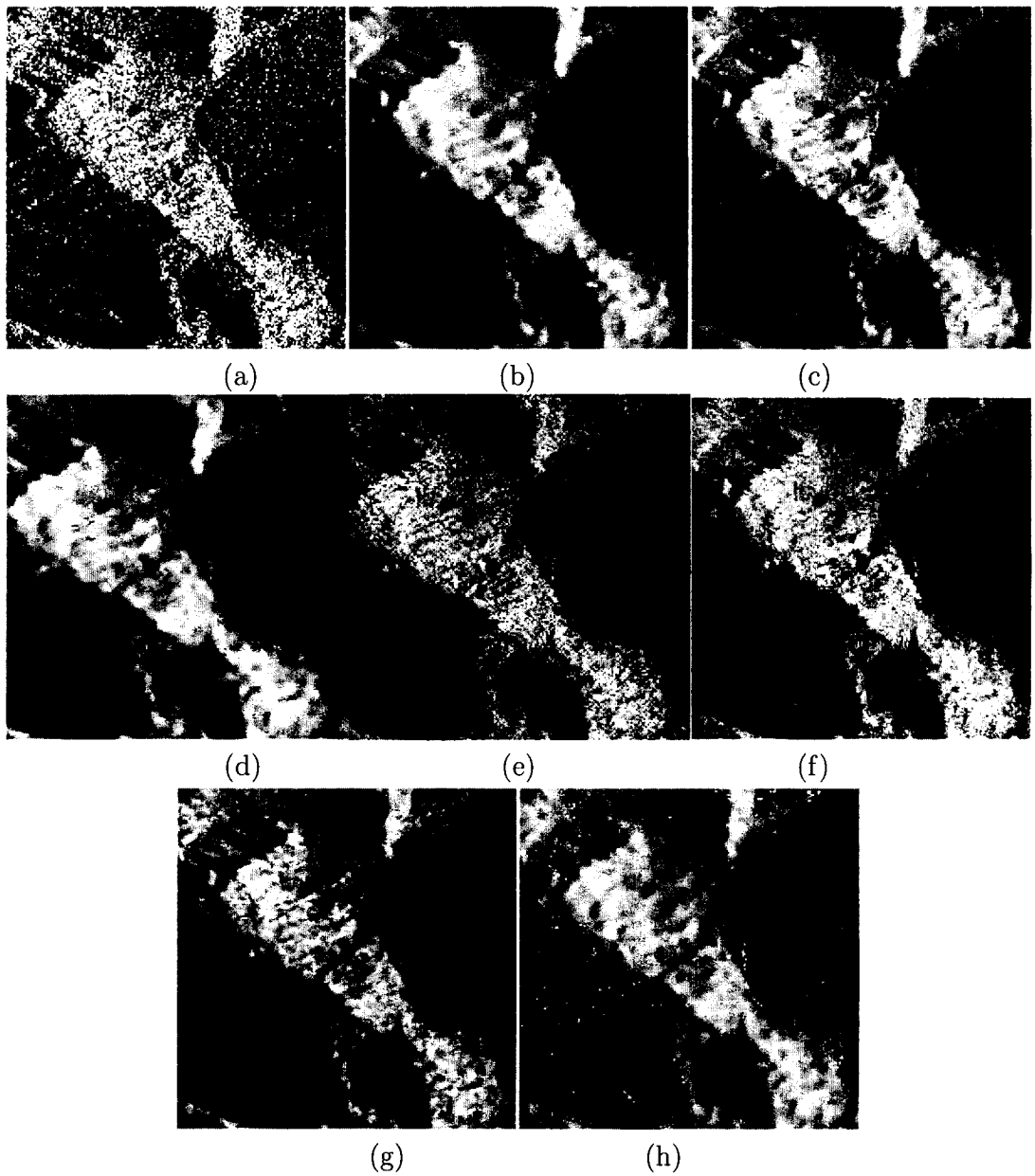

Figure 2.7: (a) Zoomed-in section of the *Cooktown* image. Corresponding denoised images using (b) SA-WBMMAE, (c) SA-WBMAP, (d) WIN-SAR, (e) WBDT, (f) FH, (g) ZC, and (g) GMAP.

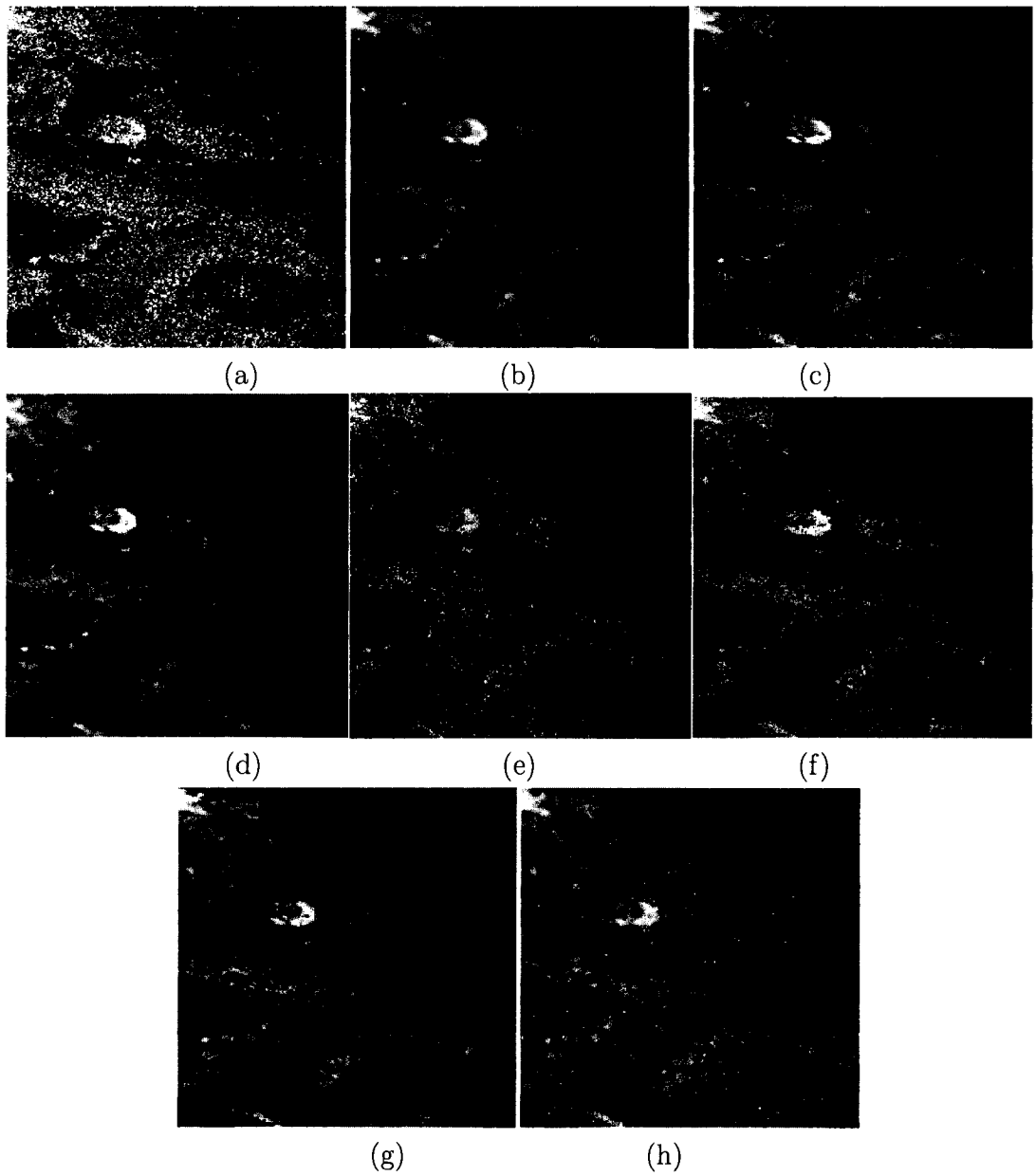

Figure 2.8: (a) Zoomed-in section of the *Collier* image. Corresponding denoised images using (b) SA-WBMMAE, (c) SA-WBMAP, (d) WIN-SAR, (e) WBDT, (f) FH, (g) ZC, and (g) GMAP.

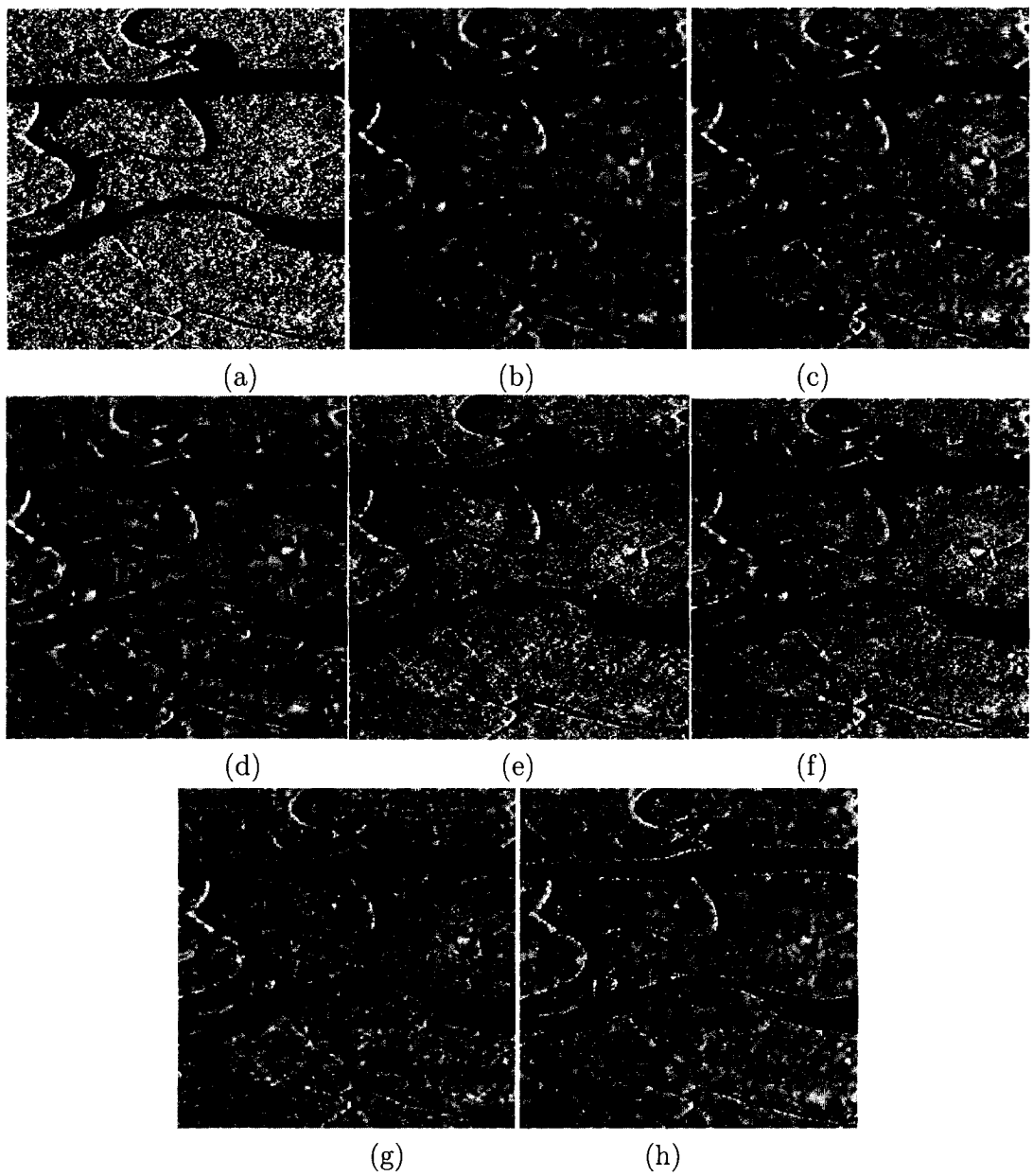

Figure 2.9: (a) Zoomed-in section of the *Ajkwa* image. Corresponding denoised images using (b) SA-WBMMAE, (c) SA-WBMAP, (d) WIN-SAR, (e) WBDT, (f) FH, (g) ZC, and (g) GMAP.

2.6 Conclusion

In this chapter, a new spatially-adaptive homomorphic wavelet-based method has been introduced for the speckle reduction in the SAR images. The SAR images have been logarithmically transformed to convert the speckle noise into an additive noise. The wavelet coefficients of the log-transformed reflectance have been modelled using a Cauchy prior with a zero-valued location parameter. Bayesian estimators, namely the MMAE and MAP estimators, have been developed using the Cauchy prior. A new method, based on a linear predictive model, has been proposed for incorporating the spatial dependence of the wavelet coefficients with the Bayesian estimation process. Simulations have been carried out using synthetically speckled images to investigate the performance of the proposed methods, and compared with that of some of the existing methods. The results have shown that the proposed method using the Bayesian MMAE estimator performs better than the others in terms of the PSNR, speckle statistics, SSIM and visual quality, whereas the proposed method using the MAP estimator gives a performance comparable to that of the former and better than that of some of the other methods considered. Finally, we have presented the results of experiments performed using SAR images, and shown that the proposed method using the MMAE estimator provides a better speckle reduction in the homogeneous regions, while still preserving the edge and line structures well.

Chapter 3

Despeckling of SAR Images Using Symmetric Normal Inverse Gaussian PDF

3.1 Introduction

The technique for despeckling SAR images described in the previous chapter uses a Cauchy PDF to model the wavelet coefficients corresponding to the log-transformed reflectivity. However, since the Cauchy PDF has only one parameter, it may not be possible to capture the statistics of the wavelet coefficients accurately. In this chapter, we consider the symmetric normal inverse Gaussian (SNIG) PDF, a generalized version of the Cauchy PDF, as a prior and show its effectiveness in modelling the wavelet coefficients of the log-transformed reflectivity. An efficient wavelet-based is then developed using the SNIG PDF, to reduce the speckle in the SAR images [68]. Extensive experiments are carried out using synthetically-speckled and SAR images, and the performance of the proposed method compared with that of several existing techniques. The rest of the chapter is organized as follows. In Section 3.2, we consider various estimators and in Section 3.3, we use these estimators to present a method for despeckling. Simulation results are provided in Section 3.4 and some concluding

remarks given in Section 3.5.

3.2 LMMSE, MMSE and MAP Estimators

The proposed denoising method in the wavelet domain involves local LMMSE filtering of the coefficients of the log-transformed SAR image. The second-order signal moments utilized in the LMMSE filtering are obtained from the preliminary estimates of the noise-free coefficients determined by employing a Bayesian MMSE or MAP estimator. We will now discuss the LMMSE and the Bayesian MMSE and MAP estimators.

3.2.1 LMMSE Estimator

Let $y(k,l)$ be the (k,l)-th pixel in a SAR image. Assuming the speckle to be fully developed, $y(k,l)$ can be expressed as [29]

$$y(k,l) = s(k,l)n(k,l) \tag{3.1}$$

where s and n represent the reflectance image and speckle noise, respectively. Upon the logarithmic transformation, (3.1) becomes

$$Y(k,l) = X(k,l) + N(k,l) \tag{3.2}$$

where $Y = \ln(y)$, $X = \ln(r)$, and $N = \ln(n)$. Since the wavelet transform is a linear operation, the wavelet coefficients of the log-transformed SAR image can be expressed as

$$g_q^i(p,m) = x_q^i(p,m) + \eta_q^i(p,m), \quad i = 1,2,3 \tag{3.3}$$

where $g_q^i(p,m)$, $x_q^i(p,m)$ and $\eta_q^i(p,m)$ are the (p,m)-th wavelet coefficients at level q with orientation i of Y, X and N, respectively. The values $1,2,3$ for i correspond

to the horizontal, vertical and diagonal orientations, respectively. For notational simplicity, g, x, and η are used in subsequent discussions. As described in Chapter 2, the noise in the wavelet domain is also zero-mean Gaussian with a variance of σ_η^2. The PDF of the Gaussian noise is given by

$$P_\eta(\eta) = \frac{1}{\sqrt{2\pi}\sigma_\eta} \exp(-\eta^2/2\sigma_\eta^2) \tag{3.4}$$

Let us denote the LMMSE estimate of the noise-free coefficient by $\tilde{x}(g)$. Given that g is the noisy coefficient, one can write [69]

$$\tilde{x}(g) = f.g \tag{3.5}$$

where f is a shrinkage factor, obtained as

$$\begin{aligned} f &= \arg\min_f E[(\tilde{x} - x)^2] \\ &= \frac{E(x^2)}{E(x^2) + \sigma_\eta^2} \end{aligned} \tag{3.6}$$

Since the wavelet filters are high-pass, we assume that $E(x) = 0$. Thus, $E(x^2) = \sigma_x^2$ and (3.6) becomes

$$f = \frac{\sigma_x^2}{\sigma_x^2 + \sigma_\eta^2} \tag{3.7}$$

where σ_x^2 denotes the variance of x. In order to gain optimal performance from (3.5), the local distributions of the wavelet image coefficients are assumed to follow a Gaussian PDF with spatially-varying signal variances [70–72]. Since σ_η^2 can be reliably estimated using the robust method of [55] from the coefficients of the subband with diagonal orientation at level 1, the performance of the LMMSE estimator heavily depends on the knowledge of the signal variances. It has been shown that the performance of the LMMSE estimator can be improved by calculating these variances from

preliminary estimates of the noise-free coefficients obtained by *ad-hoc* thresholding of the noisy coefficients [70, 72]. However, global Bayesian shrinkage methods can provide a better denoising performance as compared to the thresholding techniques [29], and thus can be expected to give more reliable preliminary estimates. Hence, the signal variances are estimated from the denoised coefficients obtained by employing a Bayesian MAP or a Bayesian MMSE estimator globally. These estimators are described in the next subsection. The signal variance of a coefficient can be obtained by employing a sample estimator within a local neighborhood. Given that the size of the neighborhood is $D \times D$, the sample estimator corresponding to the (p, m)-th coefficient in a subband is

$$\sigma_x^2 = \frac{1}{D^2} \sum_{i=-(M)/2}^{(M)/2} \sum_{j=-(M)/2}^{(M)/2} \widehat{x}(p-i, m-j)^2 \tag{3.8}$$

where $M = D - 1$, and $\widehat{x}$ represents the denoised coefficients obtained by using the Bayesian estimator. Note that a large difference between a coefficient and one of its neighbors indicates the presence of an edge, while a small difference indicates that the coefficients belong to the same homogeneous region. Hence, for estimating the signal variance of a coefficient, a weighting function is proposed, in which larger weights are attached to the neighbors that are closer to the central coefficient. The weighting function $W(p, m)$ for the (p, m)-th coefficient is given by

$$W(p, m) = \frac{1}{\sqrt{2\pi}\sigma_s} e^{-\frac{\Delta(p,m)^2}{2\sigma_s^2}} \tag{3.9}$$

where σ_s is a scale factor, and $\Delta(p, m)$ is

$$\Delta(p, m) = \widehat{x}(p, m) - \widehat{x}(p-i, m-j) \tag{3.10}$$

Then, it follows from (3.8) that the corresponding signal variance can be estimated

as

$$\sigma_x^2 = \frac{\sum_{i=-(M)/2}^{(M)/2} \sum_{j=-(M)/2}^{(M)/2} W(i,j)\widehat{x}(p-i,m-j)^2}{\sum_{i=-(M)/2}^{(M)/2} \sum_{j=-(M)/2}^{(M)/2} W(i,j)} \tag{3.11}$$

Since the LMMSE estimates expected to be better denoised as compared to the Bayesian ones, further improvement in the performance of the estimator can be achieved by obtaining σ_x^2 using $\widetilde{x}$ in place of $\widehat{x}$ in (3.10) and (3.11). Since the noise is more dominant in the finer scales such as the subbands at levels 1 and 2, this re-estimation of σ_x^2 is carried out at levels 1 and 2 only.

3.2.2 Proposed Bayesian MMSE and MAP Estimators

The Bayesian estimates are obtained by applying a Bayesian MAP or MMSE estimator globally on the coefficients of the log-transformed SAR image g. For this purpose, we propose to use a symmetric normal inverse Gaussian (SNIG) PDF [73] to model the global distribution of the coefficients in a subband. The SNIG PDF is a mixture of an inverse Gaussian and standard normal distributions, and expressed as

$$P_x(x) = A\frac{K_1(\alpha\sqrt{\delta^2+x^2})}{\sqrt{\delta^2+x^2}} \tag{3.12}$$

where $K_\lambda(\xi)$ denotes a modified Bessel function of the second kind with index λ, given by

$$K_\lambda(\xi) = \frac{1}{2}\int_0^\infty z^{\lambda-1}\exp(-\frac{1}{2}\xi(z+z^{-1}))dz \tag{3.13}$$

and $A = \frac{\alpha\delta\exp(\delta\alpha)}{\pi}$ [73]. The parameter α controls the shape of the SNIG PDF, and δ is a scale parameter. The shape of the PDF is influenced by α in that the steepness of the PDF increases monotonically with increasing α. Fig. 3.1 shows an example of the SNIG PDF for various values of α. It is noted that the parameter α has strong similarity with the parameter α of the alpha-stable PDF. The SNIG PDF results in a Gaussian distribution of variance $\sigma^2 = \frac{\delta}{\alpha}$ when $\alpha \to \infty$ and $\delta \to \infty$ such that $\frac{\delta}{\alpha}$ is

finite, whereas the Cauchy distribution is obtained when $\alpha \rightarrow 0$ [73].

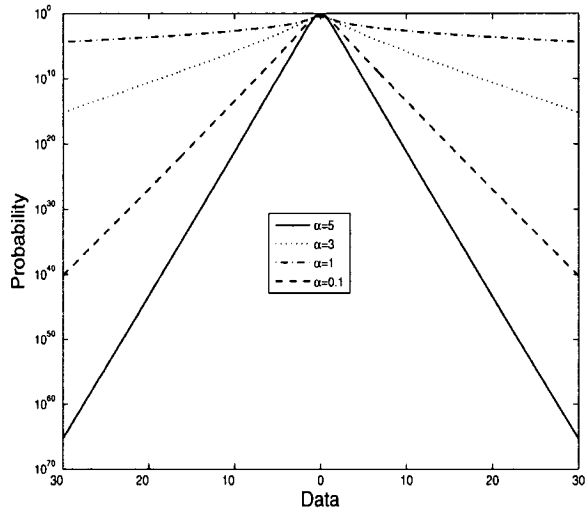

Figure 3.1: Effect of α on the shape of the SNIG PDF, with $\delta = 1$. The vertical axis is shown on log-scale.

The motivation for using the SNIG PDF for describing the global statistics is as follows. First, the global distribution of the wavelet image coefficients are in general symmetric, non-Gaussian with heavy tails [47]. Second, it has been shown in [73] that the NIG PDF can model the heavy-tailed processes more effectively than the well-known alpha-stable PDF. Third, the SNIG PDF has a closed-form expression. On the other hand, the alpha-stable PDF, not having a closed-form expression, hampers the process of estimating the parameters from the noisy data and increases the complexity of the Bayesian estimation process [46]. The effectiveness of the NIG PDF in describing the global distribution of the wavelet image coefficients has also been demonstrated in [37] and [74]. In order to study the goodness-of-fit of the SNIG PDF, the SNIG and alpha-stable PDFs are matched to the empirical PDFs of the coefficients of the various subbands of the log-transformed reflectivity corresponding

to the NASA/JPL SAR images, namely *Sanfrancisco*[1], *Cooktown* and *Collier*. Since the noise-free reflectivity corresponding to the real SAR image is not available, the proposed method for despeckling (using the Bayesian MAP estimator) is applied on the image. The result is considered as a reasonable approximation of the underlying true reflectivity; the resulting reflectivity is then log-transformed and subjected to a 3-level wavelet decomposition. The parameters of the SNIG and alpha-stable PDFs are now estimated using the well-known statistical softwares, *fBasics* [75] and *STABLE* [76], respectively. In order to compare the goodness-of-fit of the PDFs, the variance-stabilized *p-p* plots [77] corresponding to the two PDFs (SNIG and alpha-stable) were obtained. For a particular prior PDF, the variance-stabilized *p-p* plot can be obtained by plotting $F_a(x)^t$ against $F_e(x)^t$, where

$$F_a(x)^t = \frac{2}{\pi} \arcsin(\sqrt{F_a(x)}) \tag{3.14}$$

$$F_e(x)^t = \frac{2}{\pi} \arcsin(\sqrt{F_e(x)}) \tag{3.15}$$

$F_a(x)$ and $F_e(x)$ being the cumulative density function (CDF) corresponding to the prior and empirical PDFs, respectively. The *p-p* plots for the various subbands are shown in Figs. 3.2, 3.3 and 3.4. It can be observed from this figure that the SNIG PDF follows the empirical density more accurately than the alpha-stable PDF does, since the plot of the former is closer to the linear plot than that of the latter; the deviation of the latter is particularly pronounced at the two ends. Based on all the above observations, the SNIG PDF is chosen to describe the global distribution of the wavelet coefficients.

[1]obtained from the authors of [39]

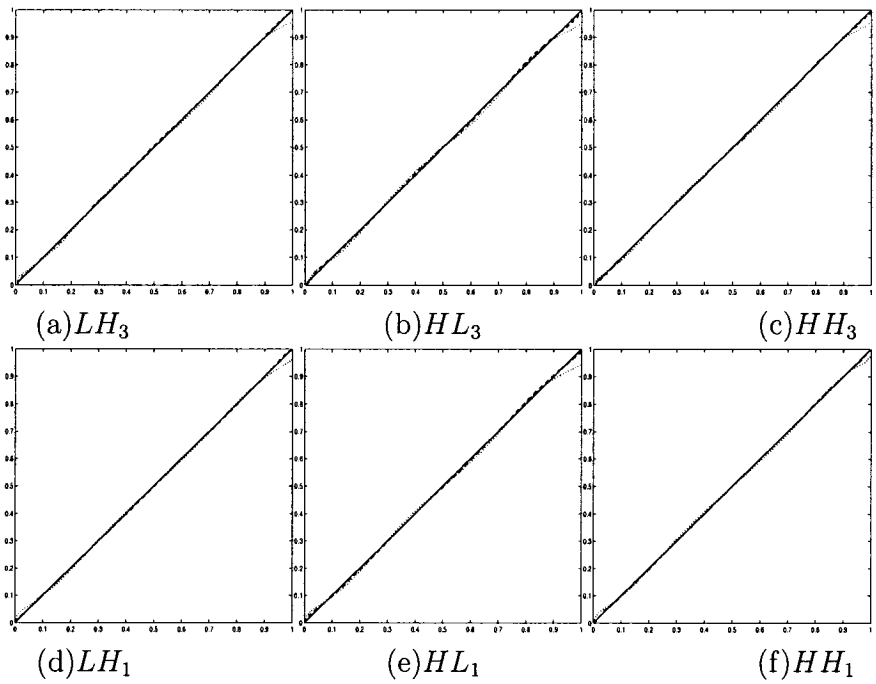

(a)LH_3 (b)HL_3 (c)HH_3

(d)LH_1 (e)HL_1 (f)HH_1

Figure 3.2: The variance stabilized *p-p* plots of the empirical, SNIG and alpha-stable PDFs for the various subbands of the SAR image, *Sanfrancisco*. The solid, broken and dotted lines correspond to the empirical, SNIG and alpha-stable PDFs, respectively. The vertical and horizontal axes correspond to the CDF of the prior and empirical PDFs, respectively.

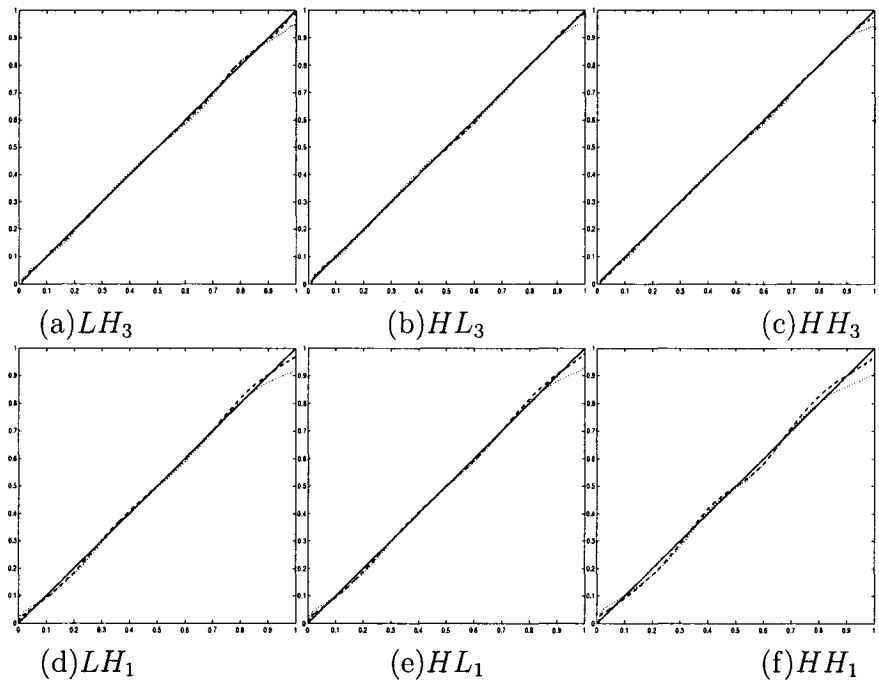

Figure 3.3: The variance stabilized *p-p* plots of the empirical, SNIG and alpha-stable PDFs for the various subbands of the SAR image, *Cooktown*. The solid, broken and dotted lines correspond to the empirical, SNIG and alpha-stable PDFs, respectively. The vertical and horizontal axes correspond to the CDF of the prior and empirical PDFs, respectively.

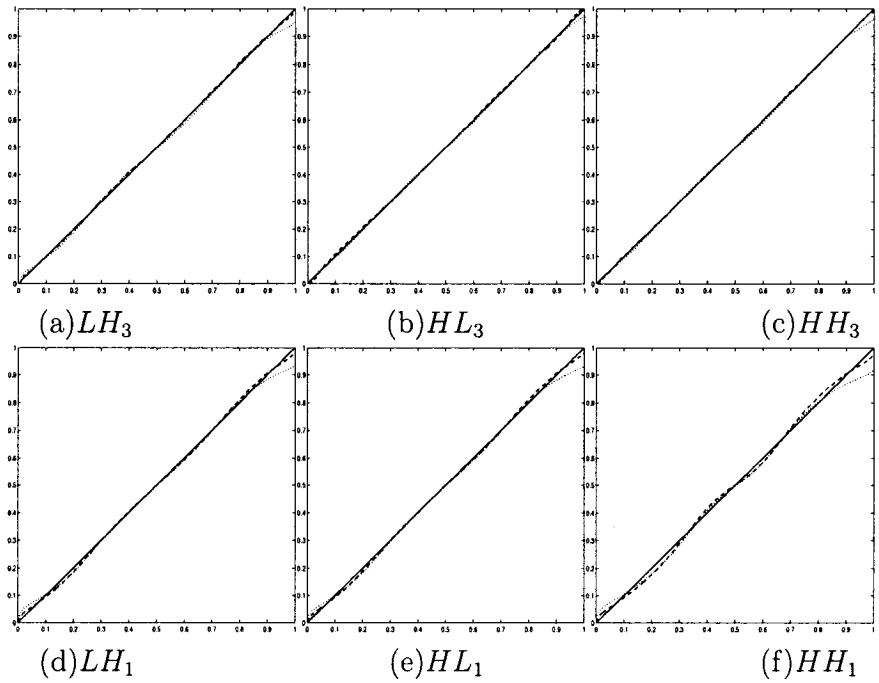

Figure 3.4: The variance stabilized *p-p* plots of the empirical, SNIG and alpha-stable PDFs for the various subbands of the SAR image, *Collier*. The solid, broken and dotted lines correspond to the empirical, SNIG and alpha-stable PDFs, respectively. The vertical and horizontal axes correspond to the CDF of the prior and empirical PDFs, respectively.

The Bayesian MMSE estimate is given by [45]

$$\widehat{x}(g) = \frac{\int P_\eta(g-x)P_x(x)x dx}{\int P_\eta(g-x)P_x(x)dx} \tag{3.16}$$

Since it is not possible to get a closed-form solution for (3.16) when the SNIG density is used, the MMSE estimates are obtained numerically using the method described in the previous chapter. On the other hand, the Bayesian MAP estimate can be obtained using

$$\widehat{x}(g) = \arg\max P_\eta(g-x)P_x(x) \tag{3.17}$$

Using the approach of Hyvarinen [54] described in Chapter 2, an approximate closed-form solution for the MAP estimator can be obtained as

$$\widehat{x}(g) = sign(g)\max(|g| - \sigma_\eta^2|p'(g)|, 0) \tag{3.18}$$

where $p'(x)$ is the derivative of $p(x) = -\ln P_x(x)$. When $P_x(x)$ is the SNIG PDF, we have

$$p'(g) = \frac{2g}{\delta^2+g^2} + \frac{\alpha g}{\sqrt{\delta^2+g^2}}\frac{K_0(\alpha\sqrt{\delta^2+g^2})}{K_1(\alpha\sqrt{\delta^2+g^2})} \tag{3.19}$$

In order to develop the Bayesian estimators, we need to have the values of the parameters of the SNIG PDF. A technique, based on the minimum distance method [78], is proposed to estimate the parameters of the SNIG PDF. Since the log-transformed signal and noise are independent, the characteristic function associated with the noisy wavelet coefficients are given by

$$\phi_g(\omega) = \phi_x(\omega).\phi_\eta(\omega), \tag{3.20}$$

where

$$\phi_x(\omega) = e^{\delta(\alpha-\sqrt{\alpha^2+\omega^2})} \tag{3.21}$$

$$\phi_\eta(\omega) = e^{-(\sigma_\eta^2/2)} \tag{3.22}$$

The parameters of the SNIG PDF are estimated by minimizing the following integral

$$\int_{-\infty}^{\infty} |\widehat{\phi}_g(\omega) - \phi_g(\omega)| \exp(-\omega^2) d\omega \tag{3.23}$$

In the above integral, $\widehat{\phi}_g(\omega)$ is the empirical characteristic function corresponding to the log-transformed noisy image in the wavelet transform domain, and obtained as

$$\widehat{\phi}_g(\omega) = \frac{1}{N_b} \sum_{t=1}^{N_b} \exp(i\omega g(t)) \tag{3.24}$$

where $g(t)$ is the t-th coefficient in a subband having N_b coefficients. The integral in (3.23) can be evaluated approximately by using the Gauss-Hermite quadrature [53] as

$$\int_{-\infty}^{\infty} \lambda(\omega). \exp(-\omega^2) d\omega \simeq \sum_{l=1}^{l=Q} \psi_l \lambda(\omega_l) \tag{3.25}$$

where $\lambda(\omega) = |\widehat{\phi}_g(\omega) - \phi_g(\omega)|$, ω_l's are the roots of the Hermite polynomials of order Q, and ψ_l's are the weights associated with these roots. Note that as a consequence of the approximation, the computational complexity in evaluating the integral in (3.23) for estimating the parameters is considerably reduced. As mentioned earlier, the noise variance, σ_η^2, can be estimated from the coefficients in the finest subband with diagonal orientation using the robust method given in [55].

3.3 Proposed Method for Despeckling

The given SAR image is first log-transformed. The wavelet coefficients of the log-transformed image are denoised by using the LMMSE estimator given in (3.5). The second-order signal moments utilized by the LMMSE estimator are calculated from the approximately noise-free coefficients obtained from a Bayesian MMSE or MAP estimator. These estimators are developed by using a SNIG PDF for modelling the

wavelet coefficients of the log-transformed reflectance. The LMMSE-filtered coefficients are inverse-transformed, followed by an exponential operation to get the despeckled image. It should be noted that the mean of the log-transformed noise is not zero. Therefore, the assumption of a zero-mean Gaussian distribution will introduce a bias in the denoised image. In order to avoid this problem, the mean of the log-transformed speckle is subtracted from the outputs of the inverse transform [35]. It should be mentioned that during LMMSE filtering using the signal moments estimated from the Bayesian MAP estimates, the coefficients that are set to zero according to (3.18) are not changed. The proposed method is given in the form of an algorithm in the following.

Proposed Speckle Reduction Algorithm	
Step 1	Carry out the logarithmic transformation of the SAR image.
Step 2	Perform the wavelet decomposition of the log-transformed noisy image.
Step 3	Obtain the Bayesian MMSE estimates from (3.16) or the Bayesian MAP estimates from (3.18).
Step 4	Once the Bayesian estimates are obtained, find the second-order signal moments using (3.11).
Step 5	Using (3.5) and the values of the signal moments obtained in Step 4, determine the LMMSE estimates of the noise-free coefficients, namely, $\widetilde{x}$.
Step 6	Obtain the estimates of the second-order signal moments of the LMMSE filtered coefficients in subbands at levels 1 and 2 using (3.11), where $\widehat{x}$ is replaced by $\widetilde{x}$.
Step 7	Using (3.5) and the signal moments obtained in Step 6, determine the LMMSE estimates for the coefficients in the subbands at levels 1 and 2.
Step 8	Perform the inverse wavelet transform of the LMMSE filtered coefficients
Step 9	Subtract the mean of the log-transformed speckle from the outputs of the inverse transform obtained in Step 8.
Step 10	Apply an exponential operation on the values obtained in Step 9.

3.4 Simulation Results

Extensive simulations are carried out in MATLAB using synthetically-speckled and SAR images to study the performance of the proposed despeckling method, and compare it with those of several existing methods. The proposed spatially-adaptive method using the Bayesian MAP and MMSE estimators are referred to as SABMAP and SABMMSE schemes, respectively. The performance of these schemes are compared with those of the methods of SA-WBMMAE [46], MAP-UWD [39], WIN-SAR [29], Pizurica *et. al.* [34], and Kuan filter [15], and referred to as SA-WBMMAE, MAP-UWD, WIN-SAR, PZ, and Kuan methods, respectively. The various wavelet-based methods are implemented using a 4-level wavelet decomposition with the *Daubechies* wavelet [60] of order 8. The results of the MAP-UWD method have been provided by the authors of [39]. Since the DWT is not shift-invariant, the denoised image is affected by the pseudo-Gibbs phenomena, resulting in 'specks' in smooth regions and 'ringing' around the edges [61]. To overcome this problem, the proposed method is implemented in the cycle-spinning mode [61] by applying it to several shifted versions of the input noisy image. The corresponding results are then shifted back, and subsequently averaged to obtain the denoised output [61]. It has been shown in [62] that the denoising methods using the orthogonal DWT with *cycle-spinning* can provide a performance equivalent to those employing the shift-invariant wavelet transforms. Furthermore, since in practice the wavelet decomposition is carried out for a few levels [35], it is sufficient to carry out the *cycle-spinning* operation for a limited number of shifts instead of all possible shifts, thus reducing the associated computational complexity. In order to ensure a fair comparison, the SA-WBMMAE, and WIN-SAR methods are also implemented in the *cycle-spinning* mode. For *cycle-spinning*, the

noisy images are circularly shifted both in the row and column directions by zero, one, two and three pixels. However, the parameter estimation is required for the zero shift only. The results of the Kuan method are obtained using a 7×7 square window. The value of M in (3.11) is set to 1.

Table 3.1: Values of PSNR for different images

Method \ L	3	4	5	6	7
House					
SABMAP	26.79	27.63	28.34	28.81	29.21
SABMMSE	26.72	27.64	28.20	28.80	29.24
MAP-UWD	25.28	–	26.63	–	27.75
SA-WBMMAE	25.36	26.06	26.85	27.19	27.64
WIN-SAR	24.90	25.99	26.76	27.39	27.98
Kuan	23.06	23.92	24.60	24.97	25.32
Boat					
SABMAP	26.56	27.42	28.04	28.52	28.93
SABMMSE	26.66	27.41	27.94	28.45	28.83
MAP-UWD	26.76	–	27.92	–	28.91
SA-WBMMAE	26.06	26.68	27.28	27.72	27.99
WIN-SAR	24.95	25.96	26.69	27.24	27.79
Kuan	23.01	23.92	24.63	25.09	25.39

3.4.1 Synthetically-speckled Images

Two noise-free images namely, *House* and *Boat* are used for obtaining synthetically-speckled images in the amplitude format. The *House* image is of 256×256 pixels, and obtained from [63], while the 512×512 *Boat* image is taken from [64]. A synthetically-speckled image is generated by multiplying a noise-free image with simulated speckle noise. Five different values of L are considered for simulating the speckle noise. Table 3.1 shows the PSNR values (in dB) obtained by the various methods for the synthetically-speckled images. It can be seen from this table that in general the SABMAP performs better than the other methods in terms of the PSNR. In order

to compare the performance of the various methods in terms of the visual quality, the noise-free images and their noisy versions (for $L = 7$), and the corresponding despeckled images obtained by the various techniques are shown in Figs. 3.5 and 3.6. From these figures, it is clear that the proposed method provides despeckled images with a visual quality that is better than those provided by most of the other techniques. Both the SABMAP and SABMMSE schemes not only smoothens the speckle noise substantially, but also retain important signal features such as the edges and line structures. In order to substantiate this observation, the values of the edge preservation index (β) proposed in [79] and the structural similarity (SSIM) index introduced in [65] are calculated for the various despeckled images shown in Figs. 3.5 and 3.6, and listed in Table 3.2. Among these two indices, the latter has been defined in Chapter 2, and the former is expressed as

$$\begin{aligned} \beta &= \frac{\Upsilon(s_l - \overline{s_l}, \widehat{s}_l - \overline{\widehat{s}_l})}{\sqrt{\Upsilon(s_l - \overline{s_l}, s_l - \overline{s_l}).\Upsilon(\widehat{s}_l - \overline{\widehat{s}_l}, \widehat{s}_l - \overline{\widehat{s}_l})}} \\ \Upsilon(s_l, \widehat{s}_l) &= \sum_{k=1}^{P}\sum_{l=1}^{M} s_l(k,l).\widehat{s}_l(k,l) \end{aligned} \tag{3.26}$$

where s_l and $\widehat{s}_l$ are the high-pass filtered versions of the noise-free image s and despeckled image $\widehat{s}$, respectively, obtained by using a 3×3 standard Laplacian operator, the overline operator denoting the mean value and $P \times M$ the dimension of the images. It can be seen from Table 3.2 that the proposed method provides larger values for β as compared to those provided by the other methods, indicating a better preservation of the edges. Also, both SABMAP and SABMMSE have SSIM indices that are higher than those of the other techniques except for that of the MAP-UWD [39] for which the values are slightly lower.

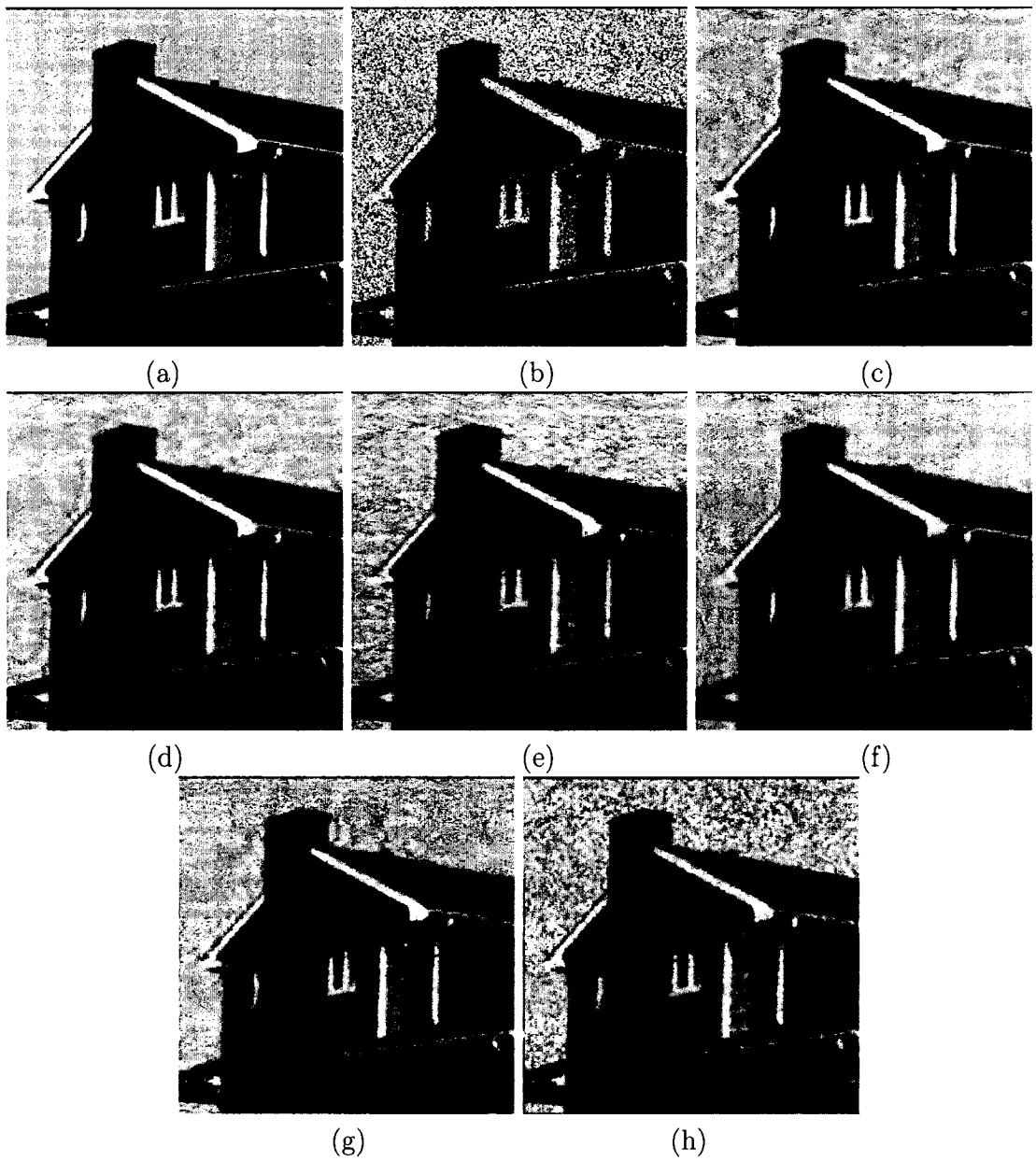

Figure 3.5: (a) Noise-free *House* image. (b) noisy *House* image. Denoised images using (c) SABMAP, (d) SABMMSE, (e) SA-WBMMAE, (f) MAP-UWD, (g) WIN-SAR, and (h) Kuan.

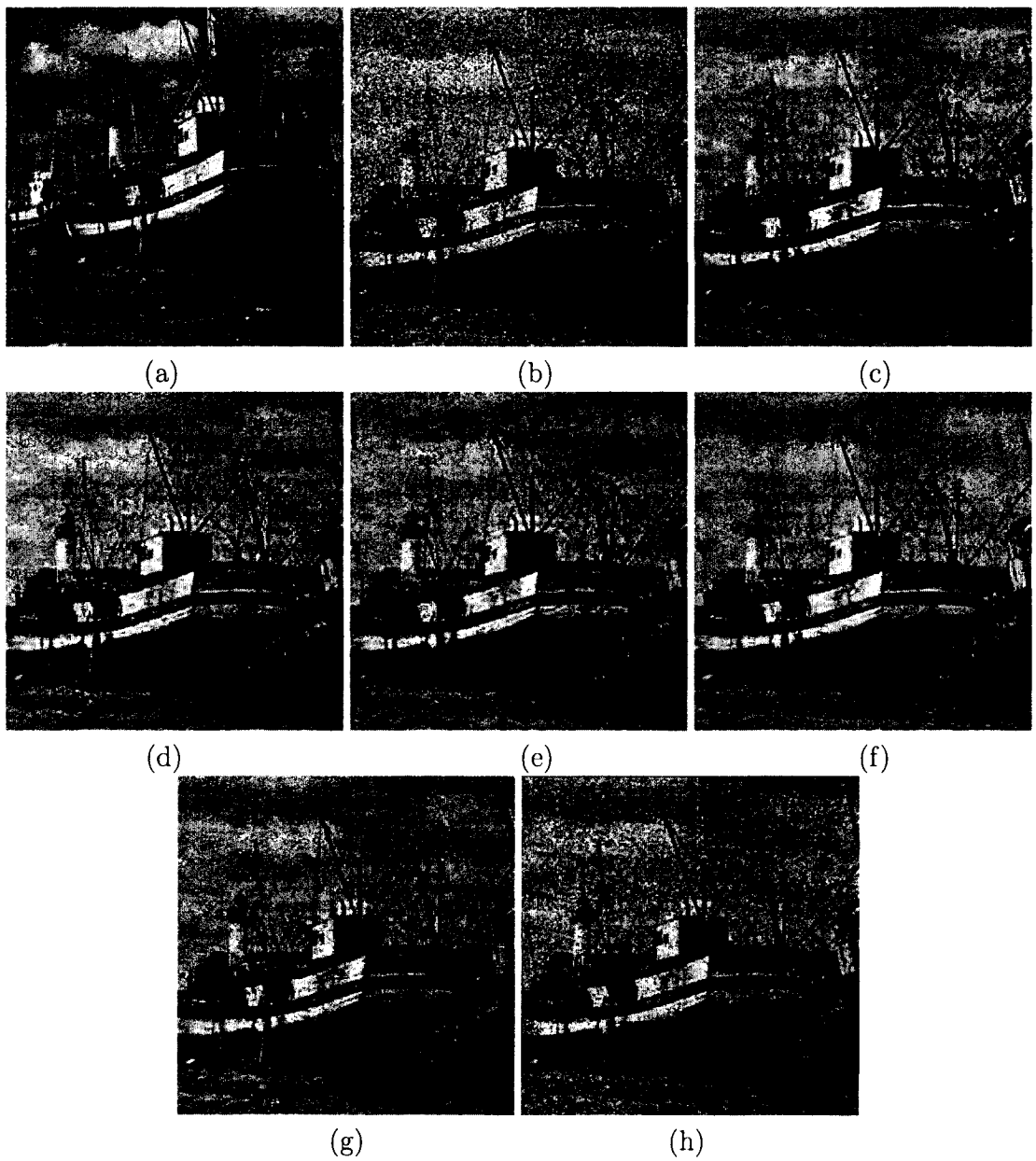

Figure 3.6: (a) Noise-free *Boat* image. (b) noisy *Boat* image. Denoised images using (c) SABMAP, (d) SABMMSE, (e) SA-WBMMAE, (f) MAP-UWD, (g) WIN-SAR, and (h) Kuan.

Table 3.2: Values of the edge preservation index (β) and SSIM for the various methods

House		
Method	β	SSIM
SABMAP	0.7956	0.7793
SABMMSE	0.7999	0.7773
MAP-UWD	0.6381	0.7816
SA-WBMMAE	0.7176	0.6718
WIN-SAR	0.7154	0.7239
Kuan	0.3203	0.6220
Boat		
Method	β	SSIM
SABMAP	0.6833	0.8012
SABMMSE	0.6901	0.8023
MAP-UWD	0.6600	0.8085
SA-WBMMAE	0.6236	0.7644
WIN-SAR	0.5843	0.7568
Kuan	0.2059	0.6424

A legitimate question arises as to how much improvement in denoising can be attributed to the use of the signal variances obtained from the Bayesian estimates and the subsequent incorporation of these variances in LMMSE filtering of the wavelet coefficients, as compared to directly estimating the signal variances from the noisy coefficients. For this purpose, an experiment is performed using the synthetically-speckled *Boat* images for various values of L. The signal variances are estimated directly from the noisy data by

$$\sigma_x^2 = \max(E(g^2) - \sigma_\eta^2, 0) \tag{3.27}$$

and used for the LMMSE filtering of the noisy coefficients, where the values of $E(g^2)$ are obtained by using g instead of $\widehat{x}$ in (3.8). The corresponding values of the PSNR are plotted along with those obtained from the SABMAP and SABMMSE in Fig. 3.7 for various values of L. It is seen from this figure that both SABMAP and SABMMSE

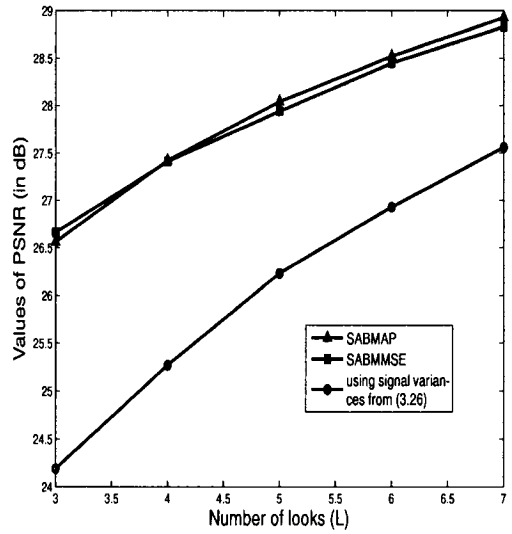

Figure 3.7: Comparison of the PSNR values for LMMSE filtering using signal variances estimated directly from the noisy data using (3.27) with those obtained using the SABMAP and SABMMSE.

provide much better PSNR values as compared to those obtained from the LMMSE filtering with signal variances estimated from the noisy coefficients.

3.4.2 SAR Images

Two amplitude-format 4-look NASA/Jet Propulsion Laboratory (NASA/JPL) images of 512×512 pixels are used in our experiment. The images are provided to us by the authors of [39]. The first image represents an airport in Ontario, while the second the Sanfrancisco Bay area, and are referred to as the *Airport* and *Sanfrancisco* images, respectively. Figs. 3.8 (a) and 3.9 (a) show the *Airport* and *Sanfrancisco*, respectively. The corresponding despeckled images obtained by the various methods are shown in Figs. 3.8 (b)-(h) and 3.9 (b)-(h). It can be observed from these images that the proposed method smoothens the speckle well, and in addition, retains the important signal features such as the edges, textures and strong reflector points.

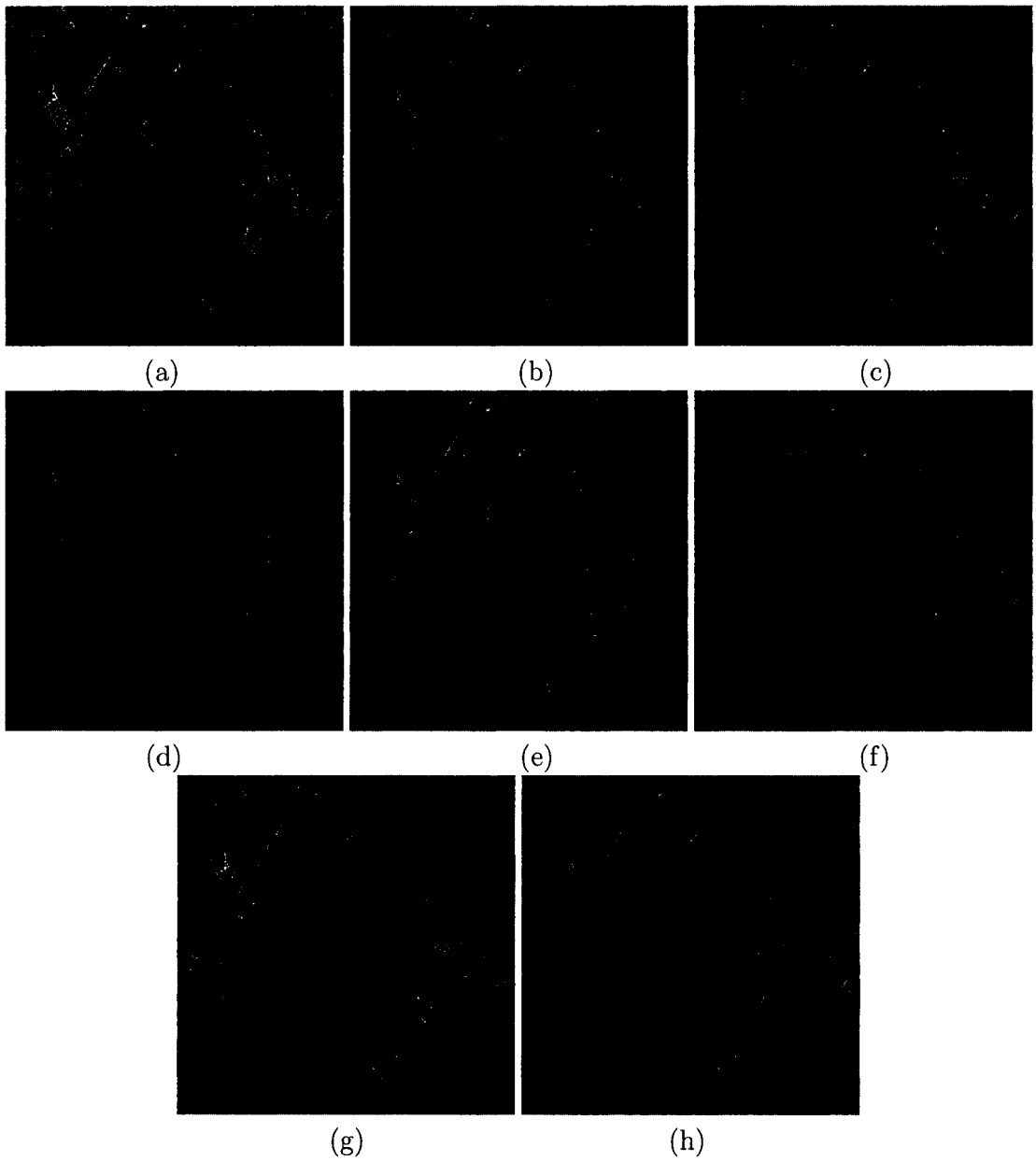

Figure 3.8: (a) The *Airport* image. The corresponding denoised images using (b) SABMAP, (c) SABMMSE, (d) SA-WBMMAE, (e) MAP-UWD, (f) WIN-SAR, (g) PZ, and (h) Kuan.

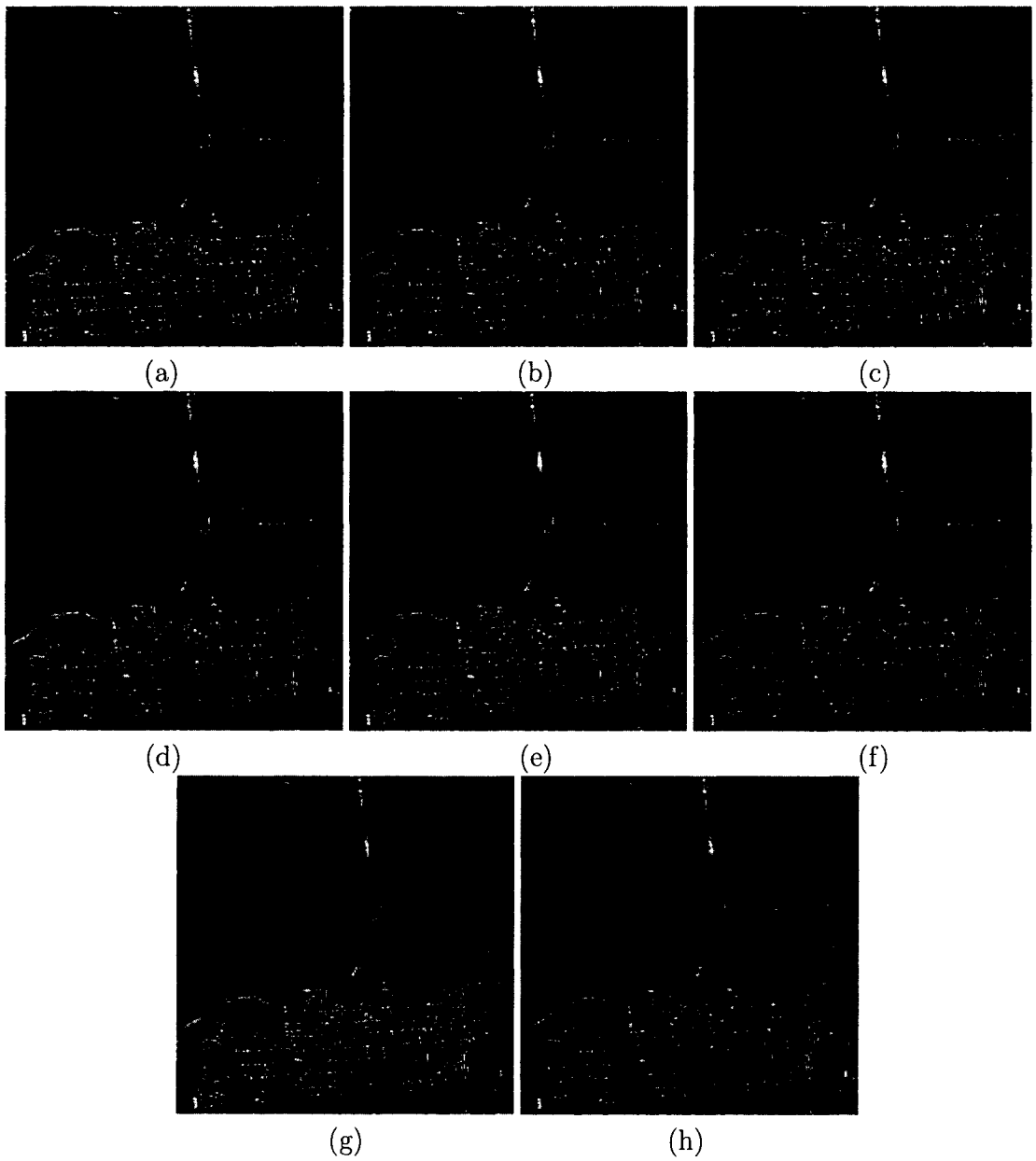

Figure 3.9: (a) The *Sanfrancisco* image. The corresponding despeckled images using (b) SABMAP, (c) SABMMSE, (d) SA-WBMMAE, (e) MAP-UWD, (f) WIN-SAR, (g) PZ, and (h) Kuan.

In order to illustrate further the superiority of the proposed method, we calculate the values of the equivalent number of looks (ENL) and the mean-bias using (2.52) and (2.53), respectively, over several homogeneous regions of the *Airport* image for the various methods. The averages of these values are listed in Table 3.3. From Table 3.3, one can see that the proposed method using either the MAP or MMSE estimator outperforms the other methods in terms of the ENL, thus indicating a better ability to suppress the speckle noise in the homogeneous regions. Also, it is noted that the mean-bias provided by the various methods including the homomorphic ones are negligibly small. This is in conformity with the observation in [37,46] that, in practice, the homomorphic wavelet-based filtering of SAR images using a statistical criterion introduces very little bias in the homogeneous regions.

Table 3.3: Average of the values of ENL and mean-bias calculated over several homogeneous regions for the *Airport* image

	ENL	Mean-bias
Before despeckling	2.74	–
SABMAP	78.48	-1.59
SABMMSE	78.85	-1.58
MAP-UWD	53.55	-4.66
SA-WBMMAE	54.80	-1.65
WIN-SAR	33.53	-1.03
PZ	34.35	-0.02
Kuan	18.70	-0.02

3.4.3 Computational Complexity

The various methods have been implemented in MATLAB on a 2.4 GHz Intel Pentium IV computer. The average CPU time taken by the various methods in order to process the synthetically-speckled images are given in Table 3.4. It is seen from this table that the SABMAP scheme is computationally much less expensive than

Table 3.4: Average CPU time (in seconds) for the synthetically-speckled images

Method	*House*	*Boat*
	(256 × 256)	(512 × 512)
SABMAP	34.07	57.42
SABMMSE	59.92	107.24
SA-WBMMAE	45.48	147.01
WIN-SAR	1052.10	1553.50
Kuan	12.05	48.75

the other techniques for despeckling except for the Kuan method whose performance is well below that of any other methods. It should be mentioned that the time spent for obtaining the parameters of the SNIG PDF remains the same regardless of the size of the image, since the parameters are obtained by minimizing (3.23) for a fixed number of roots of the Hermite polynomial. For a particular subband of size $S_x \times S_y$, the complexity corresponding to the SABMAP and SABMMSE are roughly $O(5S_xS_yD^2) + O(S_xS_y)$ and $O(5S_xS_yD^2) + O(S_k log_2 S_k) + O(S_k)$, respectively, where $S_k = \sqrt{S_x \times S_y}$.

3.5 Conclusion

In this chapter, an efficient wavelet-based spatially-adaptive method for reducing the speckle in SAR images has been presented. The proposed method is a combination of the local LMMSE filtering and global Bayesian estimation that makes use of the SNIG PDF. The global statistics of the wavelet coefficients have been characterized by a SNIG PDF, whereas the local distribution of the coefficients has been described by a Gaussian distribution with locally-varying second-order signal moments. This combination has been used to provide an effective despeckling of the SAR images at a reduced computational cost through an improved LMMSE filtering of the noisy coefficients by utilizing two Bayesian estimates that are approximately noise-free. The

two Bayesian estimators, namely, the MAP and MMSE estimators have been developed using the SNIG PDF. An efficient method with reduced complexity has been provided for estimating the parameters of the SNIG PDF from the noisy data. The performance of the proposed method has been studied using synthetically-speckled and SAR images, and compared with those of some of the existing methods. The results have shown that for the synthetically-speckled images, the proposed method using the Bayesian MAP or MMSE estimator can perform better than the others in terms of the PSNR, edge preservation index, structural similarity index and the visual quality. The results of our experiments with SAR images have shown that the proposed technique can provide a better speckle suppression in the homogeneous regions, while retaining the edges, textures, and strong reflector points. The proposed method has also been shown to be computationally less expensive than the other wavelet-based techniques.

Chapter 4

Despeckling of Medical Ultrasound Images Using SNIG PDF

4.1 Introduction

Ultrasonography is one of the most popular imaging techniques used by the clinicians for medical diagnosis. However, the ultrasound images are inherently corrupted by the speckle noise, which gives the image a granular appearance and obscures the diagnostically important details, thus hampering the detection of the pathologies by an expert human observer. In addition, the speckle noise reduces the contrast of the image and complicates the image processing tasks such as compression and segmentation.

In Chapter 3, an efficient method using the SNIG PDF to reduce the speckle in SAR images was proposed. Since the speckle also occurs in the ultrasound images, it is worth investigating the effectiveness of using the SNIG PDF for despeckling these images. A detailed study is first conducted to determine the appropriateness of the SNIG PDF in modelling the wavelet coefficients of the log-transformed reflectivity corresponding to medical ultrasound images. Based on this study, a computationally fast, spatially-adaptive method for an efficient reduction of the speckle noise

from medical ultrasound images, is proposed in this chapter [80–82]. It employs the Bayesian MAP estimator, developed in Chapter 3, to denoise locally the wavelet coefficients of the log-transformed ultrasound images. A moment-based technique is introduced to estimate the parameters of the SNIG PDF from the noisy wavelet coefficients. The performance of the proposed method is extensively studied using synthetically-speckled and medical ultrasound images, and compared with those of several existing techniques. The chapter is organized as follows. First, the problem of reducing the speckle noise in wavelet domain is outlined in Section 4.2. The Bayesian MAP estimator and a method of estimating the SNIG parameters are described in Section 4.3. Using this estimator, a method for despeckling the ultrasound images is proposed in Section 4.4. Simulation results are presented in Section 4.5 and some conclusions given in Section 4.6.

4.2 Problem Formulation

Let $G(k,l)$, $X_u(k,l)$ and $N_u(k,l)$ denote the (k,l)-th pixel of an ultrasound image, the corresponding reflectivity and the speckle noise, respectively. One can write

$$G(k,l) = X_u(k,l)N_u(k,l) + \xi(k,l) \tag{4.1}$$

where $\xi(k,l)$ is an additive noise (such as the sensor noise) [16]. In practice, the additive noise can be ignored [28], and thus (4.1) becomes

$$G(k,l) = X_u(k,l)N_u(k,l) \tag{4.2}$$

Goodman [83] carried out a detailed statistical analysis of the speckle noise, and showed that the magnitude of a fully-developed speckle noise can be modelled by a Rayleigh distribution. The speckle noise is considered to be fully developed, when the

number of scatterers in the resolution cells is large. Partially-developed speckle can be modelled by using prior distributions such as the Rician, Rician inverse Gaussian and K PDFs [84]. In this work, the speckle noise is assumed to be fully developed and correlated but independent of the reflectivity X_u [28]. The multiplicative noise in (4.2) can be converted to an additive one by log-transformation of the noisy image providing

$$G_l(k,l) = X_l(k,l) + N_l(k,l) \tag{4.3}$$

where G_l, X_l and N_l are the logarithms of G, X_u, and N_u, respectively. It has been demonstrated by a number of authors that the distribution of the log-transformed speckle is close to a Gaussian PDF [49, 51]. In fact, even if the noise is not fully developed, for practical purposes the Gaussian PDF is sufficient for approximating the distribution of the log-transformed speckle [43]. Since the discrete wavelet transform (DWT) is a linear operation, the wavelet coefficients of the log-transformed ultrasound image can be expressed as

$$g_q^i(p,m) = x_q^i(p,m) + \eta_q^i(p,m), \quad i = 1,2,3 \tag{4.4}$$

where $g_q^i(p,m)$, $x_q^i(p,m)$ and $\eta_q^i(p,m)$ are the (p,m)-th wavelet coefficients, at level q of a subband with orientation i, corresponding to G_l, X_l and N_l, respectively. The values $1, 2$, and 3 for i correspond to the subbands with horizontal, vertical and diagonal orientations, respectively. The subbands at the level q with horizontal, vertical and diagonal orientations are denoted by LH_q, HL_q, and HH_q, respectively. For notational simplicity, we will drop the subscripts and use only g, x and η in the subsequent discussion. After the wavelet decomposition, the problem is to reduce the noise term η and preserve the signal x as much as possible. Since the DWT is orthogonal, we assume that the noise η in the wavelet domain follows a Gaussian

distribution with a zero-valued mean and variance σ_η^2. To validate this assumption, the speckle noise is simulated by low-pass filtering a complex Gaussian random field, and then taking the magnitude of the filtered output. The filtering is carried out using a 3×3 window, since such a short-term correlation is sufficient to account for real speckle noise [41]. The simulated noise is subjected to a 3-level wavelet decomposition. The empirical PDFs of the various wavelet subbands are then fitted with a zero mean Gaussian PDF. For a particular subband, the variance of the Gaussian PDF is estimated from the coefficients of that subband. The empirical and fitted Gaussian PDFs for the LH_2 and HL_2 subbands are shown in Fig. 4.1. It can be observed that the Gaussian PDFs closely match the corresponding empirical ones.

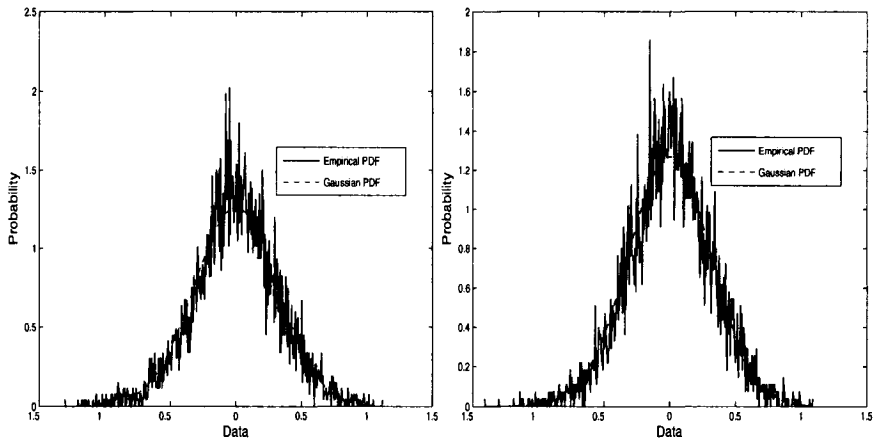

(a)LH_2 (b)HL_2

Figure 4.1: Plots of the empirical and Gaussian PDFs for the LH_2 and HL_2 subbands of simulated noise.

4.3 Bayesian MAP Estimator

In the proposed method, the reduction of the speckle noise in ultrasound images is carried out in the wavelet domain by means of a threshold that is obtained from a Bayesian MAP estimator. In order to develop the MAP estimator, the wavelet coeffi-

cients of the log-transformed reflectivity, x, are modelled by using a SNIG PDF. The efficacy of the SNIG PDF in modelling the wavelet image coefficients is studied using a number of different medical ultrasound images that include the neonatal brain, kidney, gall-bladder, liver, pancreas, heart and breast. These images are obtained from ftp://wuerlim.wustl.edu/pub/dicom/images and http://www.telin.rug.ac.be/ sanja/. Among these two image depositories, the former contains DICOM image files donated by various vendors at the annual meetings of the Radiological Society of North America between 1993 to 1996, and the latter the images used in [34]. DICOM is the acronym for Digital Imaging and Communications in Medicine, and widely accepted by the medical community as a tool for distributing and viewing medical images. Since the original noise-free images are not available for modelling, the ultrasound images are first processed by the GenLik method [41]. The resulting images are considered as reasonable approximations of the respective noise-free images, which are subsequently log-transformed and subjected to a 3-level wavelet decomposition. The distributions corresponding to the wavelet coefficients of the various wavelet subbands are then matched with the SNIG, alpha-stable and GG PDFs. For this purpose, the parameters of the GG PDF are estimated using the method of [85], whereas those of the SNIG and alpha-stable PDFs using the well-known statistical softwares *fBasics* [75] and *STABLE* [76], respectively. The goodness-of-fit provided by the various PDFs are evaluated in terms of the widely used Kolmogorov-Smirnov (KS) statistics, given by

$$d_{KS} = \max_{x \in \mathcal{R}} |F_e(x) - F_a(x)| \tag{4.5}$$

where d_{KS}, $F_a(x)$ and $F_e(x)$ denote the KS statistics, the cumulative density function (CDF) of the prior PDF and the empirical CDF, respectively [53]. The averages of

the values of the KS statistics for the various PDFs are shown in Table 4.1. It can be seen that the SNIG PDF is able to fit the wavelet coefficients more closely than the GG PDF does. Also, it is to be noted that the SNIG PDF fits the coefficients at least as well as the alpha-stable PDF does, and in many cases even better. To substantiate this observation, the empirical, and the corresponding fitted SNIG, alpha-stable and GG PDFs of the LH_2 and HL_2 wavelet subbands for ultrasound *liver* and *neonatal brain* images are shown in Figs. 4.2 and 4.3. It is observed that that the SNIG PDF fits the wavelet image coefficients better than the alpha-stable and GG PDFs do.

Table 4.1: Average values of the KS statistics for various images. For each case, the first, second and third rows show the corresponding average values obtained using the SNIG, alpha-stable and GG PDFs, respectively. The results shown are averaged over 17 images.

Level	LH	HL	HH
3	0.0318	0.0357	0.0318
	0.0256	0.0256	0.0227
	0.0623	0.0712	0.0962
2	0.0272	0.0457	0.0520
	0.0249	0.0795	0.1294
	0.0858	0.1119	0.1650
1	0.0611	0.1134	0.1135
	0.1649	0.3161	0.4715
	0.3053	0.5338	0.3976

The Bayesian MAP estimator is given by [68]

$$\widehat{x}(g) = sign(g)\max(|g| - \sigma_\eta^2|B|, 0) \tag{4.6}$$

where

$$B = \frac{2g}{\delta^2 + g^2} + \frac{\alpha g}{\sqrt{\delta^2 + g^2}} \frac{K_0(\alpha\sqrt{\delta^2 + g^2})}{K_1(\alpha\sqrt{\delta^2 + g^2})} \tag{4.7}$$

Note that (4.6) is basically a thresholding operation, wherein the threshold is $\sigma_\eta^2|B|$.

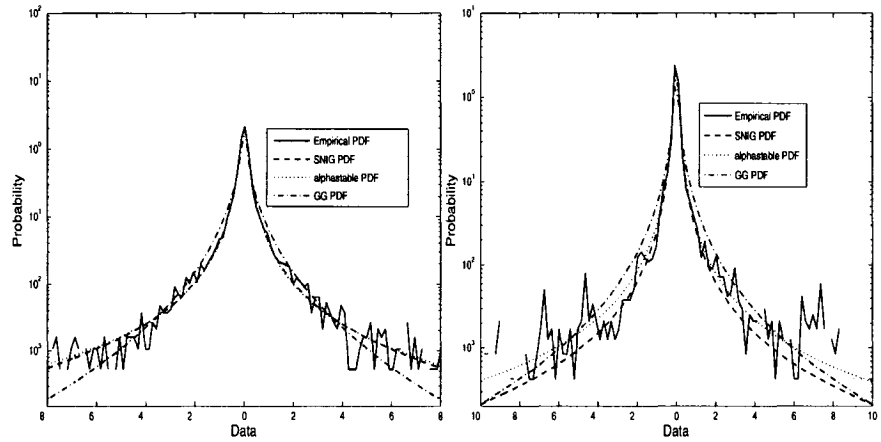

(a) (b)

Figure 4.2: Plots of the empirical, SNIG, alpha-stable and GG PDFs for the LH_2 and HL_2 subbands of an ultrasound *liver* image: (a) LH_2 and (b)HL_2. The vertical axis is on log-scale.

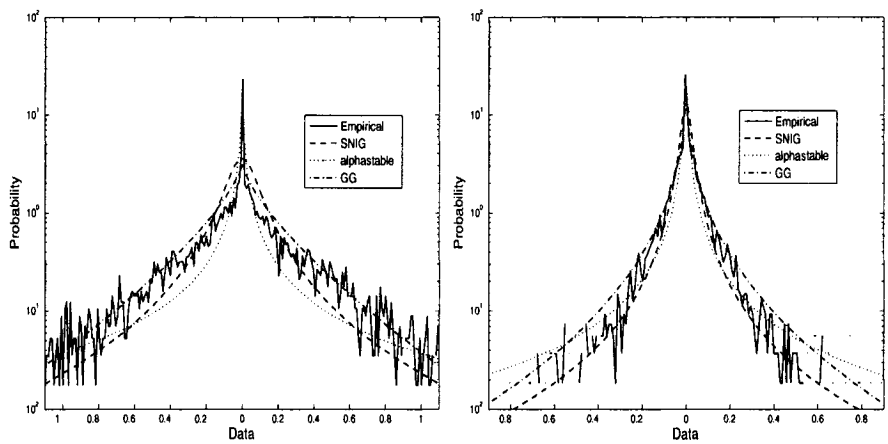

(a) (b)

Figure 4.3: Plots of the empirical, SNIG, alpha-stable and GG PDFs for the LH_2 and HL_2 subbands of an ultrasound *neonatal brain* image: (a) LH_2 and (b) HL_2. The vertical axis is on log-scale.

We will now describe a method for estimating the parameters of the SNIG PDF, i.e., α and δ. The characteristic function of the SNIG PDF is given by [73]

$$\phi_x(\omega) = \exp(\delta\alpha - \delta\sqrt{\alpha^2 + \omega^2}) \tag{4.8}$$

The corresponding cumulant generating function is obtained as

$$\begin{aligned} C_x(\omega) &= \ln \phi_x(\omega) \\ &= \delta\alpha - \delta\sqrt{\alpha^2 + \omega^2} \end{aligned} \tag{4.9}$$

The cumulants of the SNIG PDF can be obtained from (4.9) as

$$\begin{aligned} K_x^n &= (-j)^n \frac{\partial C_x(\omega)}{\partial \omega} \quad \omega = 0 \\ j &= \sqrt{-1} \end{aligned} \tag{4.10}$$

Using (4.10), the first four cumulants are obtained as

$$\begin{aligned} K_x^1 &= 0 \\ K_x^2 &= \frac{\delta}{\alpha} \\ K_x^3 &= 0 \\ K_x^4 &= \frac{3\delta}{\alpha^3} \end{aligned} \tag{4.11}$$

Using (4.11), expressions for the parameters α and δ are obtained as

$$\begin{aligned} \alpha &= \sqrt{3\frac{\widehat{K_x^2}}{\widehat{K_x^4}}} \\ \delta &= \alpha K_x^2 \end{aligned} \tag{4.12}$$

In order to make the Bayesian MAP estimator spatially adaptive, the cumulants are estimated from the local neighbors. For the (p, m)-th coefficient, the second- and

fourth-order signal moments, denoted by $\widehat{m_x^2}(p,m)$ and $\widehat{m_x^4}(p,m)$, respectively, are first estimated as

$$\begin{aligned} \widehat{m_x^2}(p,m) &= \max((\widehat{m_g^2}(p,m) - \sigma_\eta^2), 0) \\ \widehat{m_x^4}(p,m) &= \max((\widehat{m_g^4}(p,m) - 6\widehat{m_x^2}(p,m)\sigma_\eta^2 - 3\sigma_\eta^4), 0) \end{aligned} \tag{4.13}$$

The values of $\widehat{m_g^2}(p,m)$ and $\widehat{m_g^4}(p,m)$ are obtained using a $D \times D$ square window as

$$\widehat{m_g^2}(p,m) = \frac{1}{D^2} \sum_{i=-(M)/2}^{(M)/2} \sum_{j=-(M)/2}^{(M)/2} g(p-i, m-j)^2 \tag{4.14}$$

$$\widehat{m_g^4}(p,m) = \frac{1}{D^2} \sum_{i=-(M)/2}^{(M)/2} \sum_{j=-(M)/2}^{(M)/2} g(p-i, m-j)^4 \tag{4.15}$$

where $M = D - 1$. Next, the corresponding second and fourth order cumulants are obtained as

$$\begin{aligned} \widehat{K_x^2} &= \widehat{m_x^2} \\ \widehat{K_x^4} &= \max((\widehat{m_x^4} - 3\widehat{m_x^2}^2), 0) \end{aligned} \tag{4.16}$$

Simard *et al.* [86] have shown that the speckle noise in practice is correlated, and mostly concentrated at the lowest subbands. In order to take the speckle correlation into account, the value of σ_η is obtained using the coefficients in the lowest subbands with diagonal orientation as

$$\sigma_\eta = C\frac{D_1 + D_2}{2} \tag{4.17}$$

where

$$D_1 = MAD(g(p,m))/0.6745), \quad g(p,m) \in HH_1 \tag{4.18}$$

$$D_2 = MAD(g(p,m))/0.6745), \quad g(p,m) \in HH_2 \tag{4.19}$$

and C is a smoothing factor that can be used by a clinician for controlling the degree of smoothing of the speckle noise in the ultrasound image. To illustrate this, the

shrinkage function corresponding to (4.6) is shown in Fig. 4.4 for several values of C. One can observe that the zero zone of the shrinkage function widens with the increase in C. Thus, the clinician can use C to control the extent of smoothing the speckle noise. This fact is further demonstrated using simulations in Section 4.5.

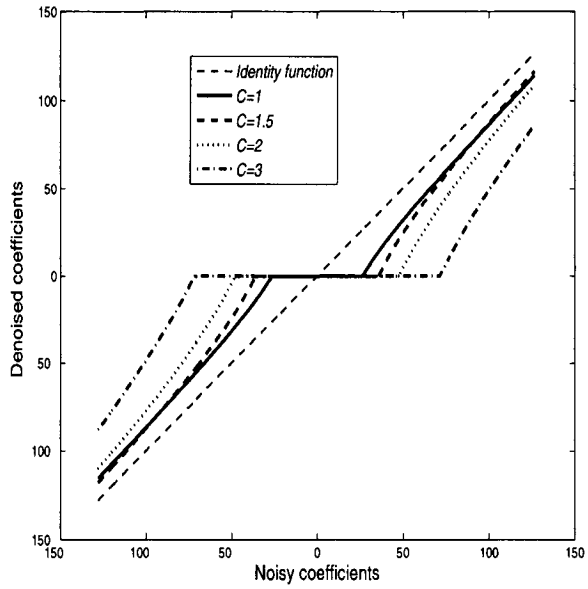

Figure 4.4: Shrinkage function for the proposed MAP estimator for different values of C.

4.4 Proposed Method for Despeckling

In the proposed method, the given ultrasound image is first log transformed. Next, the resulting image is subjected to the wavelet transform, and the corresponding wavelet coefficients processed by using the proposed Bayesian MAP estimator. The resulting coefficients are then inverse transformed, followed by an exponential operation to obtain the despeckled ultrasound image. The proposed method will be called SNIG-shrink, since it carries out a soft-thresholding operation with a threshold obtained from a Bayesian MAP estimator using a SNIG PDF. It should be mentioned

that the DWT is not shift-invariant, thus leading to pseudo-Gibbs phenomena such as *ringing* around the edges, and *specks* in the homogeneous regions [87]. These drawbacks can be overcome by implementing the denoising method using redundant transforms such as cycle-spinning, stationary wavelet transform (SWT), and dual-tree complex wavelet transform (DT-CWT) [61,87]. The DT-CWT [87] is a recently introduced redundant transform, which is nearly shift-invariant and consists of two parallel real DWTs, where the first DWT gives the real part and the second one the imaginary part of the complex coefficients. Thus, a single stage decomposition of an image provides seven subbands with one approximation subband, and six detail subbands, three containing the real parts, and the remaining three the corresponding imaginary parts of the complex wavelet coefficients. The DT-CWT provides a better directional and rotational selectivity than the SWT and DWT do, and is computationally efficient. Due to these advantages, the DT-CWT, in addition to the DWT, is employed for implementing the proposed method. Since the DT-CWT consists of two real orthogonal DWTs, the proposed method can be extended to the DT-CWT domain by implementing it for each of the DWTs. The proposed method is given in the form of an algorithm.

Proposed Algorithm for Despeckling	
Step 1.	Perform log-transformation of the ultrasound image.
Step 2.	Apply the wavelet transform on the log-transformed image.
Step 3.	Find the value of the parameters α and δ using (4.12) that of σ_η with (4.17)
Step 4.	Obtain the Bayesian MAP estimates using (4.6).
Step 5.	Obtain the inverse-transform of the MAP estimates.
Step 6.	Perform an exponential transformation of the values obtained in Step 5.

4.5 Simulation Results

Simulations are carried out in MATLAB in order to study the performance of the proposed method using synthetically-speckled and real medical ultrasound images. The performance of the proposed method is compared with those of GenLik [41], Bayes-shrink [44], and homomorphic Wiener filter [16]. The proposed SNIG-shrink method is implemented with the orthogonal DWT and the redundant DT-CWT using the *Symlet* wavelet of order 8 [60] and *Farras* wavelet [88], respectively; these referred to as SNIG-shrinkI and SNIG-shrinkII schemes, respectively. The value of D in (4.14) and (4.15) is set to 9 and 13 for the subbands at levels 4 and 3, respectively, and to 23 for the subbands at levels 1 and 2. The smoothing factor C in (4.17) is set to 1.5. The synthetically-speckled images are generated by multiplying noise-free reference images with a speckle noise simulated by passing a complex Gaussian random process through a low-pass filter, and then taking the magnitude of the filtered output. The low-pass filtering is performed using a 3×3 window, since a short-term correlation is sufficient to account for real speckle noise [41]. By varying the standard deviation of the complex Gaussian random process, it is possible to generate realistic speckle noise of different strengths. The synthetically-speckled images are obtained by corrupting the widely used *Lena*, *Barbara* and *MRI* images with noise for various standard deviations. The signal-to-noise ratio (SNR) is used as an objective criterion for comparing the performance of the various methods, and can be expressed as

$$SNR = 10\log_{10}(\frac{V_X}{V_E}) \tag{4.20}$$

where V_X and V_E represent the variance of the noise-free image X and E, respectively, where E is the difference between X and its despeckled version. here V_X represents the variance of the noise-free image X, and V_E that of the image $E = X - \widehat{X}$, $\widehat{X}$ being

Table 4.2: Values of the SNR (in dB) for the various methods

Method \ σ_n	0.4	0.5	0.6	0.7	0.8	0.9	1
Synthetically-speckled *Lena* image							
Homomorphic Wiener	13.42	13.10	12.79	12.47	12.13	11.74	11.30
Bayes-shrink	15.72	14.06	12.55	11.24	10.04	9.25	8.41
GenLik	17.30	15.72	14.39	13.29	12.38	11.47	10.61
SNIG-shrinkI	16.91	15.63	14.60	13.66	12.77	12.01	11.44
SNIG-shrinkII	17.89	16.57	15.39	14.53	13.62	12.90	12.18
Synthetically-speckled *Barbara* image							
Homomorphic Wiener	9.74	9.57	9.39	9.18	8.95	8.69	8.44
Bayes-shrink	14.10	12.22	10.70	9.45	8.32	7.35	6.53
GenLik	13.91	12.76	11.87	11.11	10.46	9.82	9.31
SNIG-shrinkI	15.71	14.33	13.19	12.16	11.19	10.32	9.48
SNIG-shrinkII	16.68	15.27	14.08	13.04	12.10	11.22	10.35
Synthetically-speckled *MRI* image							
Homomorphic Wiener	13.31	13.20	12.95	12.80	12.58	12.36	12.18
Bayes-shrink	18.22	16.25	14.69	13.36	12.24	11.25	10.29
GenLik	18.92	17.18	15.90	14.69	13.59	12.75	11.88
SNIG-shrinkI	18.61	17.03	15.74	14.68	13.61	12.68	11.77
SNIG-shrinkII	19.00	17.56	16.20	14.95	13.98	13.21	12.33

the despeckled version of X. The values of the SNR calculated for the various methods for different values of the standard deviation of the complex Gaussian random process, σ_n, are shown in Table 4.2. It should be mentioned that for a particular noise level, the value of SNR is calculated by averaging the values obtained by repeating the experiments four times. It is seen from Table 4.2 that the SNIG-shrinkII scheme outperforms all the other methods including the GenLik.

For a qualitative comparison, the despeckled images obtained by using the various methods on three synthetically-speckled noisy images, for $\sigma_n = 0.7$, are shown in Figs. 4.5, 4.6 and 4.7. It can be observed from these figures that the proposed SNIG-shrinkII scheme suppresses the speckle noise most effectively, preserving at the same time the

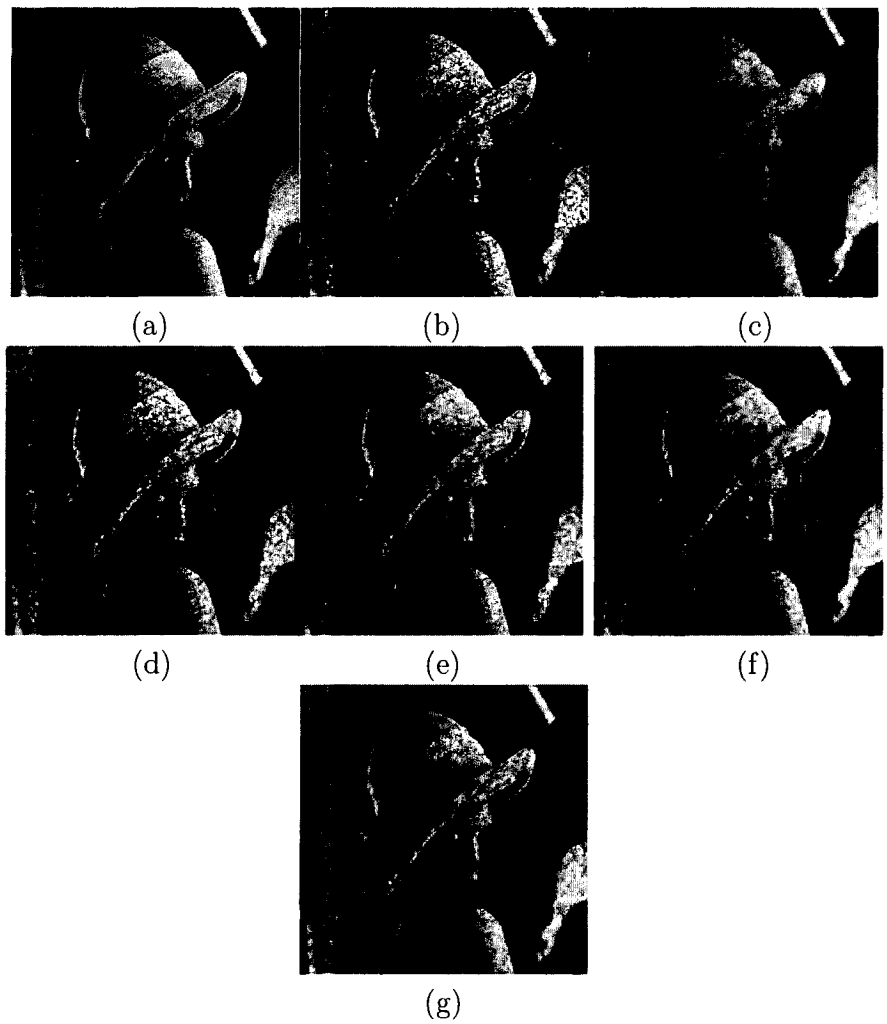

Figure 4.5: (a) Noise-free *Lena* image, (b) the corresponding noisy image for $\sigma_n = 0.7$. Denoised images obtained using the (c) homomorphic Wiener, (d) Bayes-shrink, (e) GenLik, (f) SNIG-shrinkI, and (g) SNIG-shrinkII.

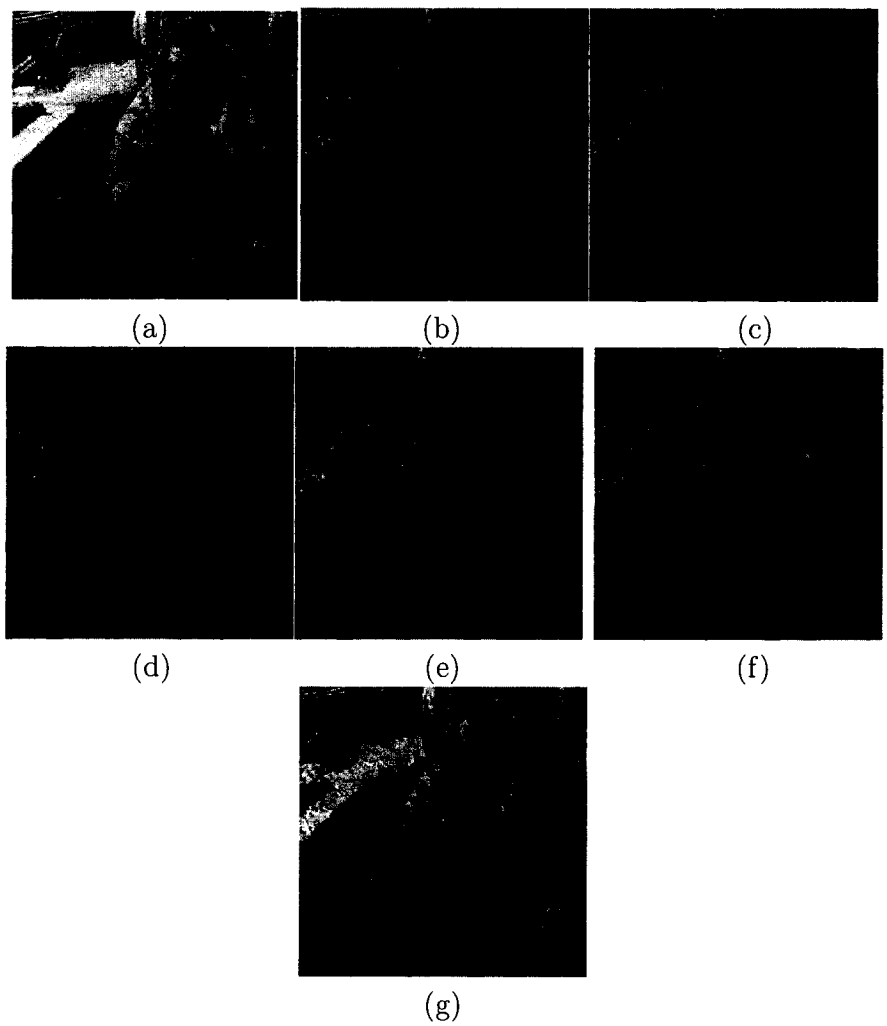

Figure 4.6: (a) Noise-free *Barbara* image, and (b) the corresponding noisy image for $\sigma_n = 0.7$. Denoised images obtained using the (c) homomorphic Wiener, (d) Bayes-shrink, (e) GenLik, (f) SNIG-shrinkI, and (g) SNIG-shrinkII.

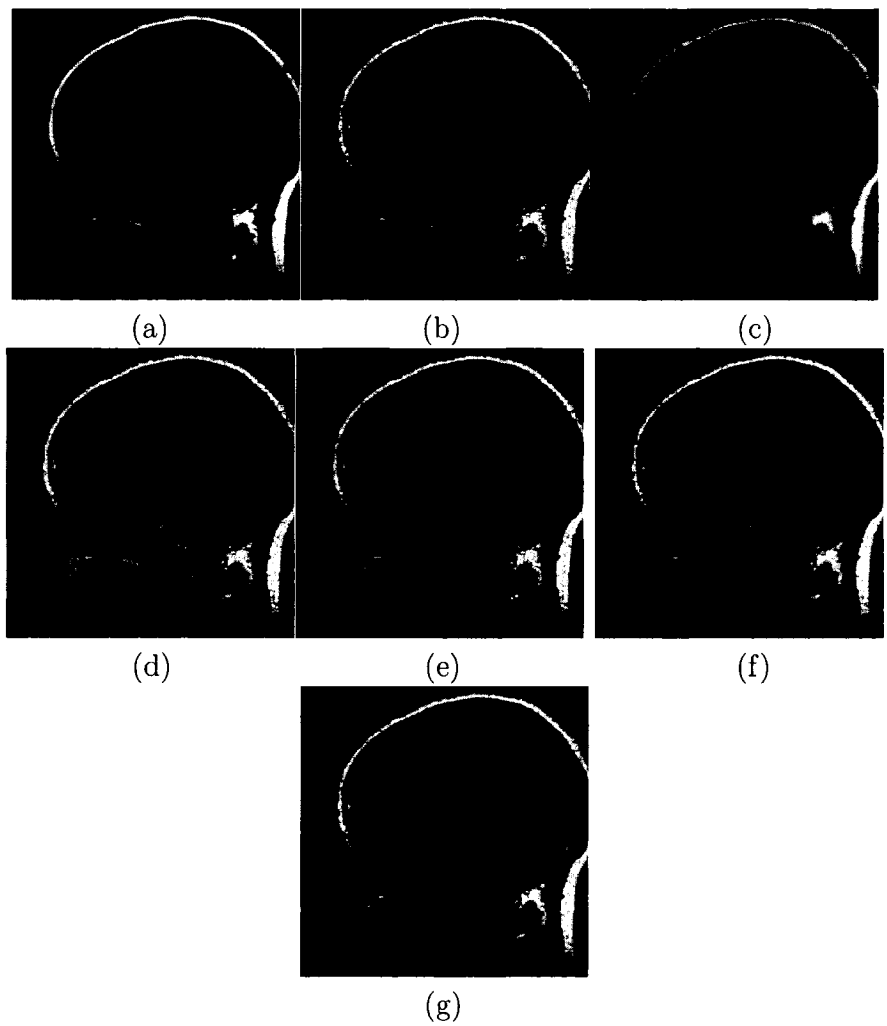

Figure 4.7: (a) Noise-free *MRI* image, and (b) the corresponding noisy image for $\sigma_n = 0.7$. Denoised images obtained using the (c) homomorphic Wiener, (d) Bayes-shrink, (e) GenLik, (f) SNIG-shrinkI, and (g) SNIG-shrinkII.

important details. On the other hand, the homomorphic Wiener filter [16] blurs the important signal features, while the images obtained by the Bayes-shrink [44] method are still noisy. To further substantiate our observations, we calculate the values of the edge preservation index β [79] and the structural similarity (SSIM) index [65] for the various methods using the different images synthetically speckled with a noise simulated for $\sigma_n = 0.7$. Among the two indices, the former is utilized for assessing the ability of a denoising method to preserve the edges, whereas the latter for signifying the visual quality of the denoised image. The optimal value for either of the two indices is unity. The values of these indices for the various methods are listed in Table 4.3. It is seen that SNIG-shrinkII consistently gives a larger value of β compared to the other methods, indicating a better preservation of the edges in the denoised images. In addition, it generally provides a better performance in terms of the SSIM index than the other techniques. To observe the visual performance of the various methods

Table 4.3: Values of the edge preservation index (β) and SSIM for the various methods

Index	Homomorphic Wiener	Bayes-shrink	GenLik	SNIG-shrinkI	SNIG-shrinkII
Lena					
β	0.6443	0.6007	0.6922	0.7565	0.7935
SSIM	0.7794	0.6083	0.7701	0.7692	0.8235
Barbara					
β	0.3618	0.7157	0.7317	0.7576	0.8785
SSIM	0.6130	0.5769	0.7151	0.8015	0.8518
MRI					
β	0.6026	0.6141	0.6640	0.6962	0.7189
SSIM	0.8359	0.8351	0.8748	0.8777	0.8937

on medical images, ultrasound images of *liver*, *obstetric*, *neonatal brain*, *kidney*, and *intraductal papilloma* are used in our experiments. We use the value of 1.5 for the smoothing factor C, since the same value is utilized with the synthetically-speckled images. As no noise-free reference images are available, the performance of the various

methods are compared from a qualitative point of view. For this purpose, the noisy *liver* and *obstetric* images and the corresponding despeckled versions obtained by using the various methods are shown in Figs. 4.8 and 4.9. Similar results are obtained for the *neonatal brain*, *kidney*, and *intraductal papilloma* images, but are not shown here. Note that the SNIGshrink-II not only smooths the noise quite effectively, but also retains the important details such as the edges and textures. In keeping with our previous observations for the synthetically-speckled images, the images obtained by employing the Bayes-shrink [44] are noisy, while those of the homomorphic Wiener filter [16] are blurred.

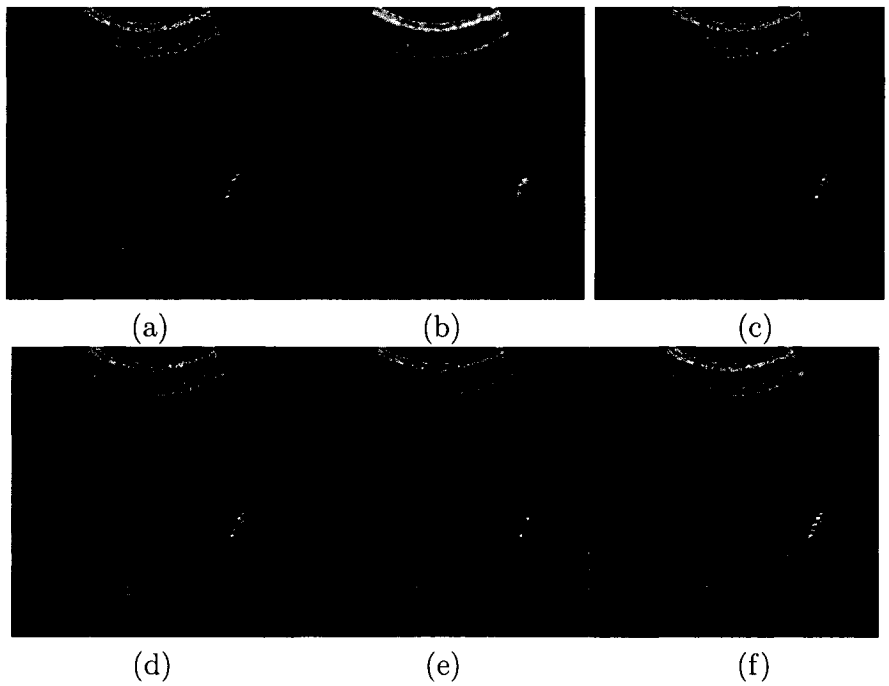

Figure 4.8: (a) An ultrasound *liver* image. Denoised images obtained using the (b) homomorphic Wiener, (c) Bayes-shrink , (d) GenLik, (e) SNIG-shrinkI, and (f) SNIG-shrinkII.

The proposed method is also computationally fast. To illustrate this, the average CPU time to process the different images used in our simulation (carried out on a 2.4

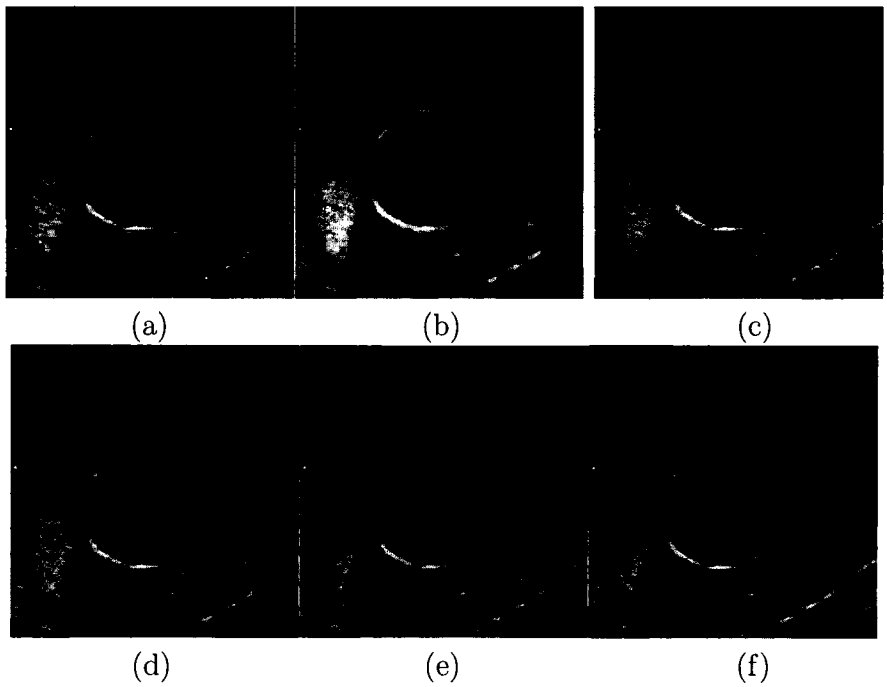

Figure 4.9: (a) An *obstetric* ultrasound image. Denoised images obtained using the (b) homomorphic Wiener, (c) Bayes-shrink, (d) GenLik, (e) SNIG-shrinkI, and (f) SNIG-shrinkII.

GHz Pentium IV computer with 768 MB RAM) are shown in Table 4.4 for the various methods. It is noted that SNIGshrink-II takes, on an average, at least 50% less time as compared to the GenLik method. Although the Bayes-shrink and homomorphic Wiener methods are faster than the other techniques, their performance is also well below that of the others. The bulk of the computational cost of the proposed method can be attributed to the parameter estimation phase. For a particular subband of size $S_x \times S_y$, the corresponding computational complexity of the proposed method can be obtained as $O(4S_xS_yD^2)$.

An interesting aspect of the proposed method is that by changing the value of C in (4.17), it is possible to achieve different levels of noise removal, while maintaining the edges. To illustrate this, the despeckled images obtained by applying the proposed

Table 4.4: CPU time in seconds for the various images

Image	Homomorphic Wiener	Bayes-shrink	GenLik	SNIG-shrinkI	SNIG-shrinkII
Lena (256 x 256)	0.20	0.82	3.87	1.37	1.54
Barbara (512 x 512)	0.28	1.37	17.00	2.95	4.85
MRI (240 x 224)	0.10	0.25	2.84	0.95	1.32
Liver (336 x 384)	0.28	1.12	6.69	2.16	2.46
Obstetric(384 x 448)	0.28	1.37	9.56	2.63	3.24
Neonatal brain (256 x 256)	0.20	0.31	3.88	1.26	1.65
Kidney (256 x 256)	0.29	0.35	3.85	1.26	1.47
Intraductal papilloma (256 x 256)	0.19	0.38	4.36	1.19	1.60

SNIG-shrinkII scheme on the ultrasound image of liver of Fig. 4.8 (a) using various values of C are shown in Fig. 4.10 . Note that with an increase in the value of C, the speckle noise is reduced more, while a stable behavior regarding the retention of strong signal features is maintained. This is an useful feature of the proposed method since it allows a clinician to control the extent of smoothing of the speckle noise as opposed to the diagnostically important details and visual quality, and indicates the robustness of the proposed method with respect to the wide variability of the ultrasound images and the requirement to process the images on a case by case basis [41]. As to the optimal value of C, from our experiments it is found to be in the range of 1.5 to 2.

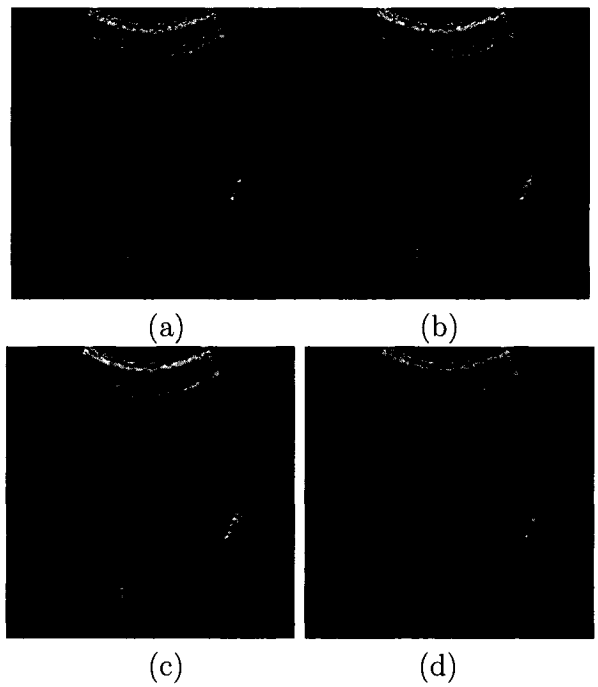

Figure 4.10: Effect of C on the performance of the SNIG-shrinkII using the ultrasound *liver* image: (a) $C = 1$, (b) $C = 1.5$, (c) $C = 2$, and (d) $C = 3$.

4.6 Conclusion

In this chapter, we have proposed a wavelet-based spatially adaptive thresholding technique for reducing the speckle noise from ultrasound images. The threshold has been derived from a Bayesian MAP estimator, which is developed using a SNIG PDF for modelling the wavelet coefficients of the log-transformed reflectivity. The justification for employing the SNIG PDF has been shown through an extensive experimental study using ultrasound images of various organs of the human body. In order to provide a spatial adaptation to the intra-scale dependency of the wavelet coefficients, the parameters of the SNIG PDF have been estimated using the intra-scale neighboring coefficients. For this purpose, a simple and fast method has been presented. The performance of the proposed despeckling method has been extensively investigated using synthetically-speckled and ultrasound images. It has been shown that for the synthetically-speckled images, the proposed method outperforms the conventional techniques as well as the recent GenLik technique, in terms of the SNR, edge preservation index, structural similarity index, and visual quality. For the ultrasound images, it has been observed that the proposed method ensures an effective suppression of the speckle noise while retaining important details such as the edges and textures, thus resulting in despeckled images of good visual quality. In addition, the method offers the examining physician the latitude in balancing the smoothing of the speckle noise against maintaining the diagnostically important details of the ultrasound image.

Chapter 5

Despeckling of Medical Ultrasound Images Using Maxwell PDF

5.1 Introduction

In the despeckling method proposed in Chapter 4, the wavelet coefficients of the log-transformed ultrasound images were denoised employing a Bayesian MAP estimator, developed using the SNIG and Gaussian PDFs, for modelling the coefficients corresponding to the log-transforms of the reflectivity and speckle noise, respectively. However, the distribution of the log-transformed speckle is actually a Fisher-Tippet PDF, which is asymmetric and has heavy tails, indicating the presence of some large-valued noise pixels [89]. Owing to the linearity and orthogonality of the wavelet transform, a similar statistic can be expected for the wavelet coefficients corresponding to the log-transformed noise. Since a Gaussian PDF is symmetric and not heavy-tailed, some large-valued coefficients that actually correspond to noise are misrepresented as signal coefficients due to the modelling of the noise coefficients with the Gaussian PDF [89]. On the other hand, unlike the Gaussian PDF, the Fisher-Tippet PDF is mathematically not tractable. To address this problem, Oleg and Tannenbaum [89] have proposed a pre-processing technique to remove the large-valued noise pixels so

that the log-transformed noise and the corresponding wavelet coefficients can be modelled with a Gaussian PDF. However, this technique is highly heuristic and dependent on the thresholds selected on an *ad hoc* basis.

The objective of this chapter is to develop an efficient and computationally fast technique for despeckling the medical ultrasound images by taking into account the heavy-tailedness of the log-transformed speckle noise [90]. For this purpose, the magnitudes of the wavelet coefficients of the log-transformed noise are modelled by a Maxwell PDF. The Maxwell PDF is chosen for several reasons: it is heavy-tailed, requires the estimation of a single parameter, and offers mathematical tractability. The coefficients corresponding to the log-transformed reflectivity are modelled by a conditional Gaussian PDF. Using the assumed PDFs, a closed-form Bayesian MAP estimator is developed to denoise the wavelet coefficients of the log-transformed ultrasound images. It should be mentioned that the Gaussian PDF is a special case of the SNIG PDF; however, it is not possible to obtain a closed-form expression for the MAP estimator using the SNIG and Maxwell PDFs. Simulations are carried out using synthetically-speckled and medical ultrasound images to study the performance of the proposed method and to compare it with that of several existing methods. This chapter is organized as follows. In Section 5.2, the proposed Bayesian MAP estimator is described, and using this estimator, a method for despeckling medical ultrasound images is introduced in Section 5.3. Simulation results are presented in Section 5.4 and some conclusions provided in Section 5.5.

5.2 Proposed Bayesian MAP Estimator

The proposed Bayesian MAP estimator is developed in the DT-CWT domain [91] in view of its shift-invariance, computational efficiency and improved directional and

rotational selectivity. Using the MAP estimator, the DT-CWT coefficients of the log-transformed ultrasound image are denoised. Let $g_q(p,m)$, $x_q(p,m)$ and $\eta_q(p,m)$ denote the (p,m)-th wavelet coefficient at level q of a particular subband of the DT-CWT of the log-transforms of the ultrasound image, the corresponding reflectivity and speckle noise, respectively. Since the wavelet transform is a linear operation, one can write

$$g_q(p,m) = x_q(p,m) + \eta_q(p,m) \tag{5.1}$$

For notational simplicity, the subscripts and indices are dropped and g, x and η are used in subsequent discussions. In order to develop a Bayesian MAP estimator for denoising the coefficients, we need to assume certain statistics regarding the coefficients corresponding to the signal and noise i.e., x and η. The signal coefficients are assumed to be locally Gaussian distributed with known values for the signal variances. This assumption has been widely adapted by the image processing community [70–72]. To further validate this assumption, an experiment is conducted using a ultrasound *kidney* image. First, the image is despeckled by the GenLik method [41] using the software available in [92]. The resulting image is considered as a reasonable approximation of the underlying reflectivity, and subjected to a DT-CWT up to 3 levels. Next, the values of the kurtosis of the wavelet coefficients are computed within a 3×3 local neighborhood for the various subbands. The average of these values are shown in Table 5.1. It can be observed from this table that the values are very close to 3, the value of the kurtosis of a Gaussian distribution. The assumed Gaussian PDF is given by

$$P_x(x) = \frac{1}{\sqrt{2\pi}\sigma_x} \exp(-x^2/2\sigma_x^2) \tag{5.2}$$

where σ_x^2 is the signal variance. The magnitudes of the noise coefficients are modelled

Table 5.1: Values of average kurtosis calculated for the various wavelet subbands. LH, HL and HH denote the subbands with horizontal, vertical and horizontal orientations, while Re and Im indicate whether the subband contains the real or imaginary part of the complex coefficients.

Level	LH^{Re}	LH^{Im}
1	2.75	2.52
2	2.72	2.76
	HL^{Re}	HL^{Im}
1	2.74	2.68
2	2.71	2.78
	HH^{Re}	HH^{Im}
1	2.99	3.00
2	2.96	2.97

using a Maxwell PDF

$$P_{|\eta|}(|\eta|) = \sqrt{\frac{2}{\pi}} \frac{|\eta|^2 \exp(-\frac{|\eta|^2}{2\nu^2})}{\nu^3} \quad \eta \geq 0 \tag{5.3}$$

The first- and second-order moments of the Maxwell PDF are 1 and $3\nu^2$, respectively. Note that the noise coefficients have positive as well as negative values. We assume that both the types are equally probable. The corresponding prior for modelling the noise coefficients is then given by

$$P_\eta(\eta) = 0.5P_{|\eta|}(|\eta|)I(\eta) + 0.5P_{|\eta|}(|\eta|)I(-\eta) \tag{5.4}$$

where $I(\eta) = 0$ when $\eta < 0$, and 1 otherwise. Using (5.4), the mean and variance corresponding to $P_\eta(\eta)$ can be found to be 0 and $3\nu^2$, respectively. The Bayesian MAP estimator is given by [80]

$$\widehat{x}(g) \quad = \quad \arg\max P_\eta(g-x)P_x(x) \tag{5.5}$$

The MAP estimate is then obtained by differentiating the logarithm of the argument in (5.5), and setting the derivative to zero. The resulting equation is

$$(\sigma_x^2 + \nu^2)x^2 - x(2g\sigma_x^2 + g\nu^2) + \sigma_x^2(g^2 - 2\nu^2) = 0 \tag{5.6}$$

The solution of (5.6) is obtained as

$$\widehat{x} = \max\left(\frac{g(2\sigma_x^2 + \nu^2) \pm B}{2(\sigma_x^2 + \nu^2)}, 0\right) \tag{5.7}$$

where

$$B = \sqrt{\nu^4 g^2 + 8\sigma_x^4 \nu^2 + 8\sigma_x^2 \nu^4} \tag{5.8}$$

Since the noise in the wavelet domain is additive, the final form for the MAP estimate is given by

$$\widehat{x} = sign(g) \max\left(\frac{|g|(2\sigma_x^2 + \nu^2) - B}{2(\sigma_x^2 + \nu^2)}, 0\right) \tag{5.9}$$

In order to obtain the MAP estimates, the parameters σ_x^2 and ν are to be estimated from the noisy coefficients. The signal variance of the (p, m)-the coefficient, $\sigma_x^2(p, m)$, is obtained using the coefficients of a $D \times D$ local neighborhood in (5.10) and (5.11) as

$$\sigma_x^2(p, m) = \max(\sigma_g^2(p, m) - \sigma_\eta^2, 0) \tag{5.10}$$

$$\sigma_g^2(p, m) = \frac{1}{D^2} \sum_{i=-M/2}^{M/2} \sum_{j=-M/2}^{M/2} g(p - i, m - j)^2 \tag{5.11}$$

where σ_η^2 is the variance of the noise and $M = D - 1$. The parameter ν is estimated as

$$\nu = \sqrt{\sigma_\eta^2/3} \tag{5.12}$$

The value of σ_η is obtained by using (4.17). As in the method described in the previous chapter, the parameter C can be used by the clinician to control the degree of smoothing the speckle in the ultrasound images. In order to illustrate this, the shrinkage function corresponding to (5.7) for various values of C is shown in Fig. 5.1. It can be observed that as the value of C increases, so the noisy coefficients are

shrinked more. The use of C in adjusting the extent speckle-smoothing is further demonstrated through simulations in Section 5.5.

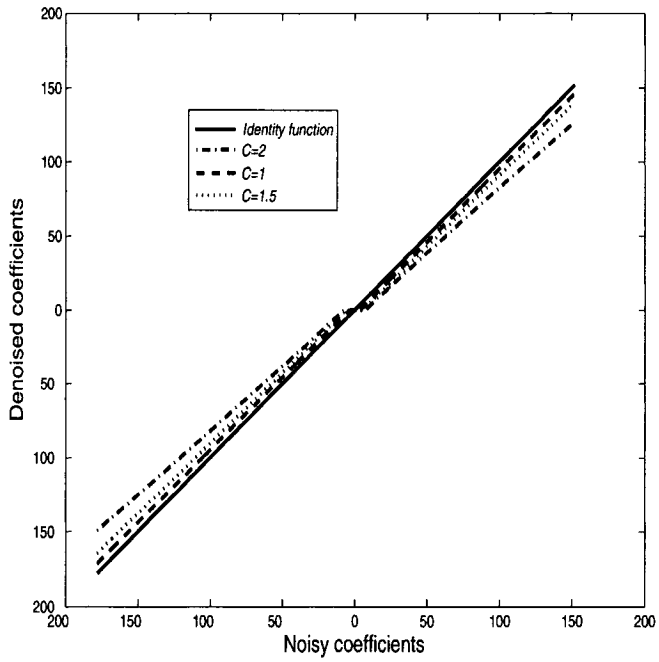

Figure 5.1: Shrinkage function for the proposed MAP estimator for different values of C.

5.3 Proposed Method for Despeckling

The given ultrasound image is first logarithmically transformed and subsequently wavelet-transformed. The corresponding wavelet coefficients are denoised by using the proposed Bayesian MAP estimator. The resulting coefficients are then inverse transformed, followed by an exponential operation to obtain the despeckled image. Since the DT-CWT tree contains two critically sampled branches, the noise standard deviation is calculated for each branch utilizing the coefficients of the corresponding finest subbands in (4.17). The proposed method is given in the following in the form of an algorithm.

Proposed Algorithm for Despeckling	
Step 1	Carry out log-transformation of the ultrasound image.
Step 2	Apply the DT-CWT on the log-transformed image.
Step 3	Estimate the parameters σ_x^2 and ν using (5.10) and (5.12), respectively.
Step 4	Find the value of σ_η using (4.17)
Step 5	Determine the Bayesian MAP estimates employing (5.9).
Step 6	Obtain the inverse-transform of the MAP estimates.
Step 7	Perform an exponential transformation of the values obtained in Step 6.

5.4 Simulation Results

Experiments have been carried out in MATLAB using synthetically-speckled and medical ultrasound images to investigate the performance of the proposed method, and compare it with that of SNIG-shrinkII [81], GenLik [41], Bayes-shrink [44], and homomorphic Wiener filter [16]. The smoothing factor C in (4.17) is set to 1.5. The synthetically-speckled images are obtained by corrupting the widely-used *Lena* and *MRI* images with noise for various values of σ_n, where σ_n denotes the standard deviation of the complex Gaussian random process that is used to generate the noise. The SNR is used as a performance criterion for the synthetically-speckled images. For a particular noise level, it is calculated by repeating the experiments four times and then averaging the corresponding values of SNR. The values of SNR obtained for the various methods are listed in Table 5.2. It is seen that the proposed method performs better than the other techniques in terms of the SNR, especially at high noise levels. For a qualitative comparison, the denoised images obtained by applying the various methods on the *Lena* and *MRI* images synthetically-speckled with a noise simulated for $\sigma_n = 0.8$, are shown in Figs. 5.2 and 5.3. It is seen from these figures that the proposed technique provides images with a better visual quality in comparison to the other methods. In order to substantiate this observation, the values of the

Table 5.2: Values of the SNR (in dB) for the various methods

Method \ σ_n	0.4	0.5	0.6	0.7	0.8	0.9	1
Synthetically-speckled *Lena* image							
Homomorphic Wiener	13.42	13.10	12.79	12.47	12.13	11.74	11.30
Bayes-shrink	15.72	14.06	12.55	11.24	10.04	9.25	8.41
GenLik	17.30	15.72	14.39	13.29	12.38	11.47	10.61
SNIG-shrinkII	17.89	16.57	15.39	14.53	13.62	12.90	12.18
Proposed	17.74	16.66	15.62	14.85	14.08	13.44	12.79
Synthetically-speckled *MRI* image							
Homomorphic Wiener	13.31	13.20	12.95	12.80	12.58	12.36	12.18
Bayes-shrink	18.22	16.25	14.69	13.36	12.24	11.25	10.29
GenLik	18.92	17.18	15.90	14.69	13.59	12.75	11.88
SNIG-shrinkII	19.00	17.56	16.20	14.95	13.98	13.21	12.33
Proposed	17.94	16.88	16.04	15.25	14.58	13.97	13.44

edge preservation index [79] and the SSIM index [65] are calculated for the various methods using the images shown in Figs. 5.2 and 5.3, and the same listed in Table 5.3. It is seen from this table that the values of the indices provided by the proposed method are higher than those of the other techniques, thus indicating its superiority in preserving the edges and in providing better visual quality.

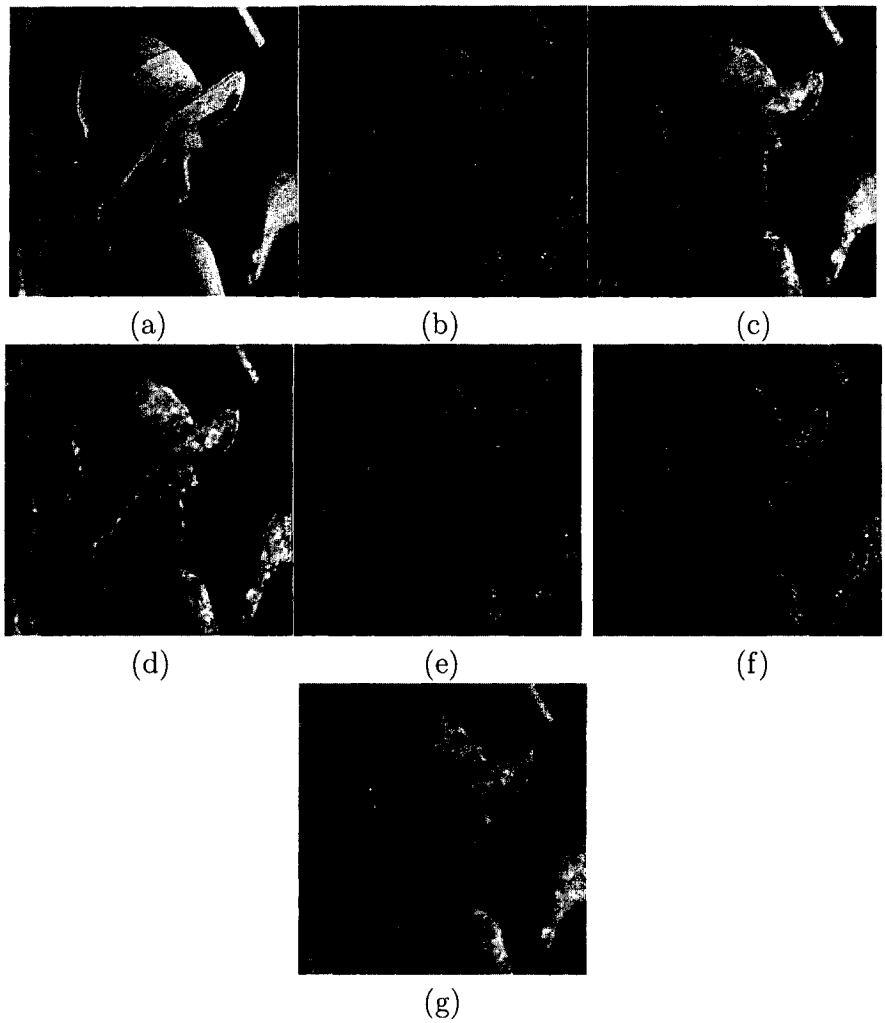

Figure 5.2: (a) Noise-free *Lena* image, (b) the corresponding noisy image for $\sigma_n = 0.8$. The denoised images obtained by using the (c) proposed, (d) SNIG-shrinkII, (e) GenLik, (f) Bayes-shrink, and (g) homomorphic Wiener methods.

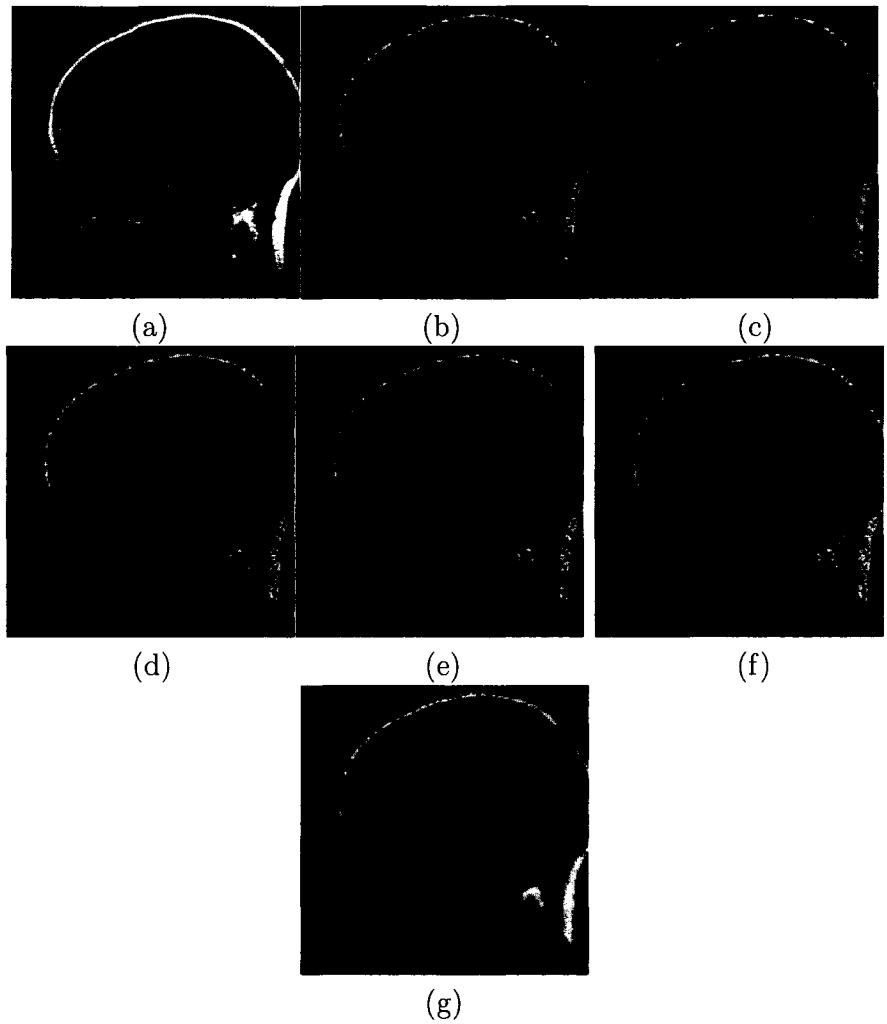

Figure 5.3: (a) Noise-free *MRI* image, (b) the corresponding noisy image for $\sigma_n = 0.8$. The denoised images obtained by using the (c) proposed, (d) SNIG-shrinkII, (e) GenLik, (f) Bayes-shrink, and (g) homomorphic Wiener methods.

Table 5.3: Values of the edge preservation index (β) and SSIM index for the various methods

Method	*Lena*		*MRI*	
	β	SSIM	β	SSIM
Proposed	0.7914	0.8136	0.7066	0.8821
SNIG-shrinkII	0.7630	0.7895	0.6819	0.8757
GenLik	0.6227	0.7443	0.6197	0.8472
Bayes-shrink	0.6000	0.6128	0.5734	0.7937
Homomorphic Wiener	0.6152	0.7339	0.6014	0.8174

Experiments are also carried out with *neonatal brain* and a *obstetric* ultrasound images. The corresponding denoised images obtained employing the various methods are shown in Figs. 5.4 and 5.5. It can be observed from these figures that the proposed method ensures a good balance between effective speckle suppression and the retention of diagnostically important details. On the other hand, the method of homomorphic Wiener provides a good speckle suppression at the expense of blurring the edges of the image, whereas the images obtained using the Bayes-shrink [44] are still noisy.

An important aspect of the proposed method is that by varying the smoothing factor C in (4.17) while estimating σ_η, it is possible for the clinician to choose the level of noise smoothing, preserving the important details of the image as much as is needed according to his expert opinion. To illustrate this, the proposed method is applied to the *obstetric* ultrasound image with different values of C. The resulting denoised images are shown in Fig. 5.6. It can be observed that with increasing C, the speckle noise is reduced more, while the edges and textures of the image are adequately preserved. This is indicative of the robustness of the proposed method in view of the wide variability of the ultrasound images and the need to process them on a case-by-case basis, even for a single patient [41]. The proposed method is also

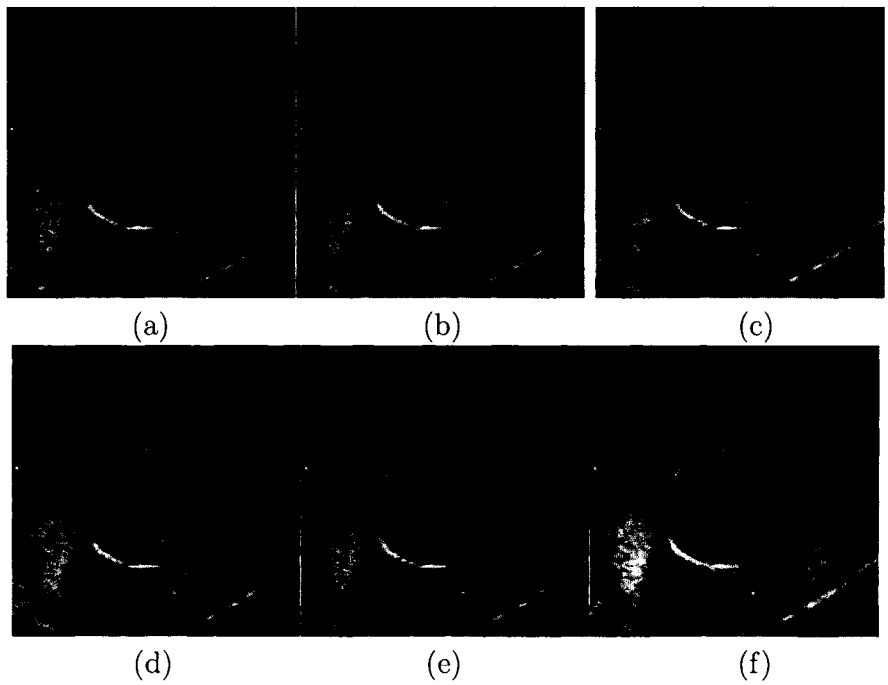

Figure 5.4: (a) An *obstetric* ultrasound image. Denoised images obtained using the (b) proposed, (c) SNIG-shrinkII, (d) GenLik, (e) Bayes-shrink, and (f) homomorphic Wiener methods.

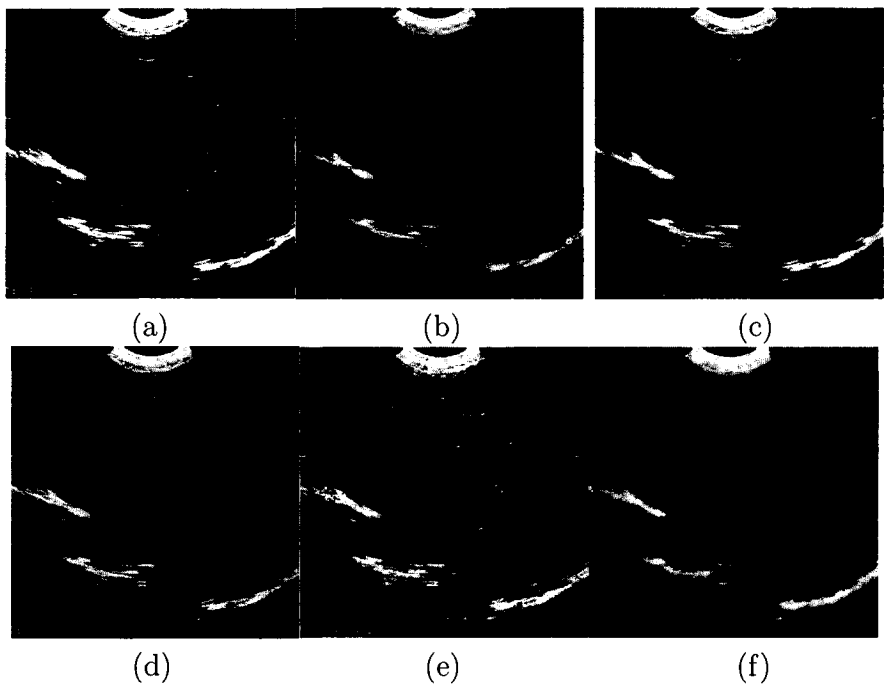

Figure 5.5: (a) An ultrasound *neonatal brain* image. Denoised images obtained using the (b) proposed, (c) SNIG-shrinkII, (d) GenLik, (e) Bayes-shrink, and (f) homomorphic Wiener methods.

computationally fast. To illustrate this, the average CPU time (on a 2.4 GHz Pentium IV computer with 768 Mb RAM) taken by the proposed, SNIGshrink-II and GenLik methods are shown in Table 5.4. It is seen from this table that the proposed technique is faster than the SNIG-shrinkII and GenLik methods. For a subband of size $S_x \times S_y$, the corresponding complexity of the proposed method is $O(2S_xS_yD^2)$.

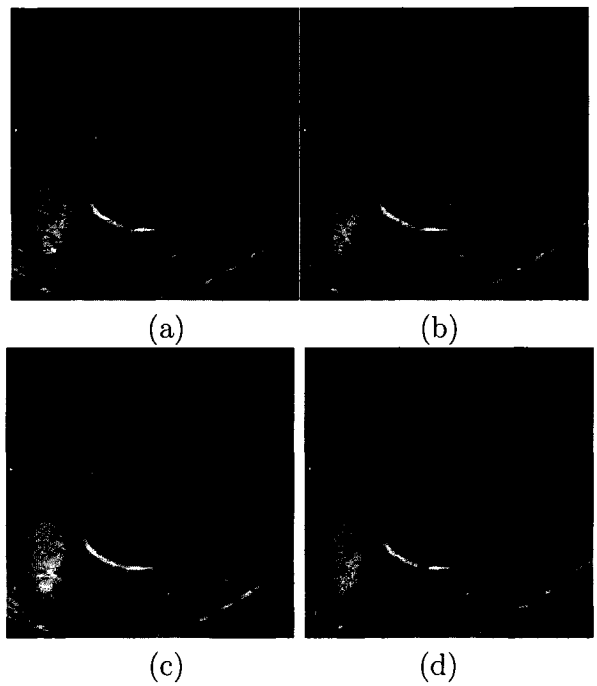

Figure 5.6: Effect of C on the performance of the proposed method using the *obstetric* ultrasound image. (a) $C = 1$, (b) $C = 1.5$, (c) $C = 2$ and (d) $C = 3$.

Table 5.4: CPU time in seconds for the various images

Method	*Lena*	*MRI*	*Obstetric*	*Neonatal brain*
Proposed	0.72	0.67	1.64	0.70
SNIG-shrinkII	1.50	1.32	3.24	1.65
GenLik	3.87	2.84	9.56	3.88
Bayes-shrink	0.82	0.25	1.37	0.31
Homomorphic Wiener	0.20	0.10	0.28	0.31

5.5 Conclusion

In this chapter, a spatially-adaptive wavelet-based method has been proposed for the reduction of speckle in medical ultrasound images. The real and imaginary parts of the dual-tree complex wavelet coefficients corresponding to the log-transform of underlying reflectivity have been modelled with a conditional Gaussian distribution. The coefficients corresponding to the log-transformed speckle have been modelled by a Maxwell distribution. Using the assumed prior models, a Bayesian MAP estimator has been developed with a closed-form expression. The proposed method is self-sufficient, in the sense that the prior parameters are obtained from the noisy data. It is also spatially adaptive, since the signal variances are estimated utilizing the local neighbors. Experiments have been carried out using synthetically-speckled and ultrasound images to compare the performance of the proposed technique with that of several existing techniques. The results have shown that the proposed method is superior to the other techniques in terms of the SNR, edge preservation index and SSIM index. In addition, it is computationally fast and retains diagnostically important features.

Chapter 6

Image Denoising with SNIG PDF and LMMSE Estimator

6.1 Introduction

A classical problem in image processing is the reduction of additive white Gaussian noise (AWGN) from natural images. Numerous methods have been proposed to deal with this problem among which the wavelet-based ones demonstrate the most promising results [44, 93]. Among the various wavelet-based techniques, the incorporation of the spatial dependence of the wavelet coefficients offers a superior performance [58, 59, 62, 70–72, 94–105]. An important class of these methods includes those that assume the local distribution of the wavelet coefficients to be Gaussian with spatially varying variance and employs an LMMSE estimator locally in order to denoise the coefficients [59, 70–72, 100–106]. These methods, in general, provide a sound performance in denoising with low complexity. However, most of them incorporate the intra-scale dependency only and do not actually consider the inter-scale dependency. A few methods incorporate the inter-scale dependency in addition to the intra-scale one at the expense of a substantial increase in the computational complexity [100, 105], whereas the methods of [59] and [106] are dependent on parameters

selected on an *ad hoc* basis.

The despeckling method described in Chapter 3 uses an LMMSE estimator for denoising the wavelet coefficients of log-transformed SAR images. Since the log-transformed speckle noise is modelled as Gaussian, the method proposed in Chapter 3 can be adapted to the case of reducing the AWGN from natural images. However, the LMMSE estimator in Chapter 3 incorporates the intra-scale dependency only. In this chapter, a new LMMSE estimator is proposed that incorporates not only the intra-scale dependency, but also the inter-scale dependency. The signal variances are estimated from the approximately noise-free coefficients obtained using a Bayesian MMSE estimator that is developed employing a SNIG PDF to model the wavelet image coefficients. The use of the SNIG PDF is motivated by the results of an extensive experimental study, which shows that it is highly suitable for modelling the wavelet image coefficients. An ML-based method of moderate complexity is proposed for estimating the parameters of the SNIG PDF from the noisy coefficients. The performance of the proposed method is studied using typical noise-free images for both the orthogonal and redundant wavelet transforms. This Chapter is organized as follows. The proposed LMMSE estimator is discussed in Section 6.2, and the process of obtaining the Bayesian estimates described in Section 6.3. Simulation results are provided in Section 6.4. Finally, some concluding remarks are given in Section 6.5.

6.2 Proposed LMMSE Estimator

In this section, the proposed LMMSE estimator is discussed. Let a noise-free image X be corrupted with i.i.d. additive white Gaussian noise N that has a zero-valued mean and variance σ^2. The corresponding noisy image is denoted by G. One can

write

$$G = X + N \tag{6.1}$$

The DWT of a two-dimensional image up to level J results in the approximation subband LL_J as well as the subbands LH_q, HL_q and HH_q with horizontal, vertical and diagonal orientations, respectively, where $q = 1, 2, \cdots, J$ [47]. Since the wavelet transform is a linear operation, after applying the DWT on (6.1), we get

$$g_q^i(p,m) = x_q^i(p,m) + \eta_q^i(p,m), \quad i = 1,2,3 \tag{6.2}$$

where $g_q^i(p,m)$, $x_q^i(p,m)$ and $\eta_q^i(p,m)$ denote the (p,m)-th wavelet coefficient at level q with orientation i of G, X and N, respectively, and $i = 1, 2, \text{and } 3$ correspond to the horizontal, vertical and diagonal orientations, respectively. Note that, due to the orthogonality of the DWT, η is also i.i.d. white Gaussian with a zero mean value and variance σ^2. The PDF of η is given by

$$P_\eta(\eta) = \frac{1}{\sqrt{2\pi}\sigma} \exp(-\eta^2/2\sigma^2) \tag{6.3}$$

The LMMSE estimate of the (p,m)-th noise-free coefficient, $\widetilde{x}(p,m)$, is obtained as

$$\widetilde{x}(p,m) = \xi(p,m).g(p,m) \tag{6.4}$$

where $g(p,m)$ and $\xi(p,m)$ denote the noisy coefficient and the shrinkage factor, respectively, and the shrinkage factor is given by

$$\xi(p,m) = \frac{\sigma_x^2(p,m)}{\sigma_x^2(p,m) + \widehat{\sigma}^2} \tag{6.5}$$

where $\sigma_x^2(p,m)$ is the variance corresponding to the (p,m)-th noise-free coefficient. Eq. (6.5) can be written as

$$\xi = \frac{1}{1+\phi} \tag{6.6}$$

where

$$\phi(p,m) = \frac{\widehat{\sigma}^2}{\sigma_x^2(p,m)} \tag{6.7}$$

For coefficients that have a large signal content, $\sigma_x^2 >> \widehat{\sigma}^2$, and hence, ϕ is quite small; this results in a negligible shrinkage of these coefficients. On the other hand, for a noise-dominated coefficient, $\widehat{\sigma}^2 >> \sigma_x^2$. Therefore, the corresponding value of ϕ is large resulting in a large shrinkage of the corresponding coefficient. The mean-squared error in estimation corresponding to the LMMSE estimator, $\theta(p,m)$ is given by [107]

$$\theta(p,m) = (1-\xi)^2\sigma_x^2 + \xi^2\widehat{\sigma}^2 \tag{6.8}$$

The first part of the right sight of (6.8) represents the signal distortion while the second the noise residual.

It is known that an LMMSE estimator provides an optimal performance when both the signal and noise are Gaussian distributed [69]. Since the LMMSE estimator is employed locally for noise reduction in wavelet domain, we assume the local distribution of the coefficients to be i.i.d. Gaussian with zero mean and spatially-varying variance. This assumption has been widely employed by the image processing community [70–72, 100–102]. Although the wavelet coefficients show intra-scale dependency, it is highly local and valid only within a narrow local neighborhood, beyond which it diminishes rapidly. The inter-scale dependency is strong only between a scale and its corresponding parent scale, and decreases rapidly for the subsequent scales. In this chapter, the intra-scale dependency is taken into account by obtaining the variance of the Gaussian distribution using the coefficients within a square-shaped window. The inter-scale dependency is included by incorporating it in the LMMSE estimator. As to the size of the window, it is important to choose the one that is most appropriate

for the local Gaussian assumption. For this purpose, we find the values of kurtosis and skewness of the various wavelet subbands corresponding to three representative images, namely *Lena*, *Barbara* and *Boat* using 3×3, 5×5 and 7×7 neighborhoods. It may be noted that the kurtosis defines the peakedness and the skewness the symmetry of a distribution; these are 3 and 0, respectively, for a Gaussian distribution [53]. The average values of the kurtosis and skewness for the various subbands for *Lena*, *Barbara* and *Boat* images are listed in Table 6.1. It is seen from this table that the maximum deviation of the average value of the kurtosis for any of the images from the true value of 3 occurs for the HH_3 subband, and are 0.71, 2.46 and 3.52 for the 3×3, 5×5 and 7×7 window, respectively. The average values of the skewness differ from the actual value of 0 by a small margin for all the three windows, the difference being the least for a 3×3 window. Hence, we consider a 3×3 window for describing the local distribution of the wavelet coefficients, and approximate the local distribution by a Gaussian distribution. This choice has also the added advantage that it results in the smallest computational complexity.

The efficacy of the LMMSE estimator depends heavily on the accuracy of estimating the variance corresponding to a noise-free coefficient [71]. It has been shown that by using variances estimated from coefficients obtained by thresholding the noisy ones with an *ad hoc* threshold, it is possible to enhance the performance of an LMMSE estimator in denoising [70, 72]. It is known that Bayesian shrinkage based on solid statistical modelling of the global distribution of the wavelet coefficients can provide better estimates of the noise-free coefficients [29,93]. In this work, we assume that the coefficients obtained using a Bayesian MMSE estimator are approximately noise-free, and utilize these coefficients in obtaining the variances corresponding to the noise-free coefficients. The validity of this assumption is verified through simulations in the

Table 6.1: Average values of kurtosis and skewness for various wavelet subbands of the *Lena*, *Barbara* and *Boat* images. For each neighborhood size, these values are shown in the first and second rows, respectively.

Neighborhood size	LH_1	LH_2	LH_3	HL_1	HL_2	HL_3	HH_1	HH_2	HH_3
	Lena								
3 × 3	3.08	3.41	3.43	3.06	3.26	3.16	3.12	3.42	3.66
	-0.0236	-0.0123	0.0084	-0.0183	-0.0037	0.0211	0.0002	-0.0098	-0.0124
5 × 5	3.49	4.16	5.15	3.48	3.90	4.82	3.46	3.93	5.26
	-0.0383	-0.0274	-0.0126	-0.0226	0.0013	0.0696	0.0122	-0.0051	-0.0147
7 × 7	3.93	4.83	5.99	3.88	4.89	5.62	3.75	4.62	6.52
	-0.0457	-0.0446	0.0457	-0.0288	-0.0181	-0.0073	0.0086	0.0019	0.0020
	Barbara								
3 × 3	2.95	3.30	3.34	2.86	3.22	3.15	2.93	3.33	3.58
	0.0578	0.0159	-0.0017	-0.0066	0.0233	0.0416	-0.0035	0.0173	-0.0086
5 × 5	3.37	4.05	5.15	3.44	3.98	4.77	3.17	4.03	5.56
	0.0877	0.0177	-0.0306	-0.0171	0.0260	0.0994	-0.0073	-0.0314	-0.0447
7 × 7	3.75	4.73	5.50	3.99	4.77	5.06	3.36	4.68	5.96
	0.1063	0.0843	0.0755	-0.0274	-0.0124	-0.0076	-0.0090	-0.0208	-0.0233
	Boat								
3 × 3	2.98	3.32	3.22	3.10	3.46	3.41	3.02	3.53	3.71
	-0.0135	0.0052	-0.0104	-0.0135	-0.0235	0.0467	0.0001	0.0069	-0.0133
5 × 5	3.42	4.23	4.68	3.75	4.36	5.20	3.26	4.23	5.46
	0.0116	-0.0089	0.0093	-0.0349	-0.0268	0.0801	0.0101	0.0238	-0.0025
7 × 7	3.84	4.88	4.97	4.30	5.32	5.61	3.49	5.10	5.87
	0.0186	0.0174	0.0195	-0.0616	-0.0589	-0.0442	0.0199	0.0221	0.0154

next section. Let us denote the Bayesian MMSE estimates with $\widehat{x}(p,m)$. The signal variance for the (p,m)-th coefficient is estimated as

$$\sigma_x^2(p,m) = \frac{1}{M} \sum_{i=-W}^{W} \sum_{j=-W}^{W} \widehat{x}^2(p-i, m-j) \tag{6.9}$$

where $M = (2W+1)^2$. Note that the LMMSE estimator in (6.4) incorporates the intra-scale dependency only since the variance of a coefficient is obtained using local neighbors within a square window.

It is well known that the magnitudes of the wavelet coefficients are strongly correlated across the scales. If a coefficient is large, the corresponding coefficients of the parent subband are more likely to have large magnitudes rather than small ones. Since the strength of a signal depends on its standard deviation, it is likely that the standard deviations of the coefficients may also show a similar behavior across the scales [106], [100]. Thus, if a coefficient has a large standard deviation, the corre-

sponding coefficient of the parent subband may also have large standard deviations. On the contrary, the standard deviation of the noise coefficients rapidly decays as one goes up through the scales, indicating a poor parent-child correlation [106] and the prominency of the noise in the finer scales. The correlation between the parent and the corresponding children coefficients across the scales, being essentially due to the images being piecewise smooth (that is, the homogeneous regions are separated by edges), represents the edges of an image in the multi-scale wavelet domain [106]. The reduction of the signal distortion is important as it affects the quality of the denoised image considerably. Since such a distortion is often caused by the distortion of the edges in the wavelet domain, one can exploit the parent-child correlation to reduce it. For this purpose, we propose to use the standard deviation of the parent coefficient to modify the shrinkage factor ξ. The modified shrinkage factor, $\widehat{\xi}$, is given by

$$\widehat{\xi} = \frac{1}{1+\widehat{\phi}} \tag{6.10}$$

where

$$\widehat{\phi} = \frac{\widehat{\sigma}^2}{\sigma_x^2(p,m) + \sigma_x(p_1,m_1)}, \; p_1 = \lceil p/2 \rceil, \; m_1 = \lceil m/2 \rceil \tag{6.11}$$

$\sigma_x(p_1,m_1)$ being the standard deviation of the (p_1,m_1)-th coefficient in the parent subband. The modified shrinkage factor, $\widehat{\xi}$, is finally written as

$$\widehat{\xi} = \frac{\sigma_x^2(p,m) + \sigma_x(p_1,m_1)}{\sigma_x^2(p,m) + \sigma_x(p_1,m_1) + \widehat{\sigma}^2} \tag{6.12}$$

and thus, the LMMSE estimates of the noise-free coefficient $\widetilde{x}(p,m)$ becomes

$$\widetilde{x}(p,m) = \widehat{\xi}(p,m).g(p,m) \tag{6.13}$$

The corresponding mean-squared error in estimation, $\widehat{\theta}(p,m)$, is given by

$$\widehat{\theta}(p,m) = (1-\widehat{\xi})^2\sigma_x^2(p,m) + \widehat{\xi}^2\widehat{\sigma}^2 \tag{6.14}$$

From (6.7), (6.11), (6.6) and (6.12), it is noted that $\widehat{\phi} < \phi$ and hence, $\xi < \widehat{\xi}$. This results in a decrease of the signal distortion at the expense of increasing the noise residual, as seen from (6.8) and (6.14). However, this is acceptable for signal-dominant coefficients since the magnitudes of such coefficients are generally much larger than the corrupting noise. It is also acceptable for the noise-dominant coefficients since the shrinkage factor is still large, the parent-child correlation is quite weak, and the value of the standard deviation of the parent coefficient is rather small. Moreover, most of the noise power is concentrated in the finer scales, namely, the subbands at levels 1 and 2. Therefore, in order to further decrease the noise residual, the signal variances are re-estimated using (6.9) from the denoised coefficients in the subbands at levels 1 and 2. Using these variances, the noisy coefficients in the finer scales are filtered again. Overall, we have a decrease in the signal distortion as well as the noise residual, hence leading to an improvement in the visual quality of the denoised image, as illustrated later through simulations in Section 6.4.

6.3 Obtaining the Bayesian MMSE Estimates

In this section, we describe the proposed Bayesian estimator for obtaining a set of approximately noise-free coefficients that are used to obtain the signal variances. Natural images comprise mostly homogeneous regions and a few signal features such as edges and textures. Since the homogeneous areas contribute to the wavelet coefficients that are close to zero, while the edges and textures to a few large-valued coefficients, the global distribution of the wavelet coefficients is symmetric having a sharp peak around zero with heavy tails [47]. Recently, the normal inverse Gaussian (NIG) PDF has been reported to be highly effective in modelling heavy-tailed processes [37,73,74]. Hence, we develop a Bayesian estimator based on modelling the global distribution

of the wavelet coefficients with the symmetric NIG (SNIG) PDF. It should be noted that the previously assumed local Gaussian assumption does not contradict the SNIG PDF used in this section, since the latter is utilized for describing the global statistics of the wavelet coefficients which are obviously non-Gaussian, while the former is used for modelling the local distribution of the coefficients. In order to justify the use of the SNIG PDF and compare its efficacy with that of the well-known prior distributions, such as the GG and Bessel-K form (BKF) PDFs, a set of experiments is carried out using thirty representative images. Among these images, the *Boat*, *House*, and *Fingerprint* are taken from [108], and the rest from the well-known image databases, the Waterloo Bragzone [64] and the USC-SIPI database [109]. The *Frog* and *Mountain* images are of size 621×498 and 640×480, respectively, and the rest consists of images of 256×256 and 512×512 pixels. Each image is subjected to a 3-level wavelet decomposition followed by a process of fitting the SNIG, GG and BKF PDFs to the coefficients in each subband. The parameters of the SNIG PDF are obtained using the proposed ML-based method (described later in this section), whereas those of the BKF and GG PDFs by employing the methods of [93] and [85], respectively. The Kolmogorov-Smirnov (KS) statistic [53] is used to quantify the goodness-of-fit provided by the various PDFs. Table 6.2 lists the average values of this statistic for the various PDFs. It is evident from the table that in general the SNIG PDF is better at modelling the wavelet coefficients as compared to the GG and BKF PDFs.

To show the effectiveness of the SNIG PDF graphically, the various PDFs are plotted along with the empirical ones for the various subbands of three representative noise-free images, namely, *Lena*, *Barbara*, and *Boat*. The three images and the corresponding plots are shown in Figs. 6.1, 6.2 and 6.3. It is observed that in general the SNIG PDF provides an excellent fit to the modes as well as the tails of the empir-

Table 6.2: Average values of the KS statistics for various images. For each level, the first, second and third rows show the corresponding average values obtained using the SNIG, GG and BKF PDFs, respectively.

Level	LH	HL	HH
3	0.0309	0.0264	0.0218
	0.0269	0.0239	0.0198
	0.0980	0.0664	0.0852
2	0.0175	0.0189	0.0142
	0.0214	0.0232	0.0173
	0.1155	0.1117	0.1211
1	0.0128	0.0129	0.0096
	0.0198	0.0214	0.0113
	0.1725	0.3199	0.1256

(a) (b) (c)

Figure 6.1: Noise-free images: (a) *Lena*, (b) *Barbara* and (c) *Boat*.

ical distributions. The values of α estimated for the various subbands for the three representative images are provided in Table 6.3. It can be seen that α increases with decreasing subband level. The global distribution of the wavelet subbands becomes more heavy-tailed for those at the lower levels. The results of Table 6.3 indicate that the SNIG PDF is highly suitable for capturing the heavy-tailed character of the global distribution of the wavelet coefficients, thus further motivating the use of this PDF as a prior model.

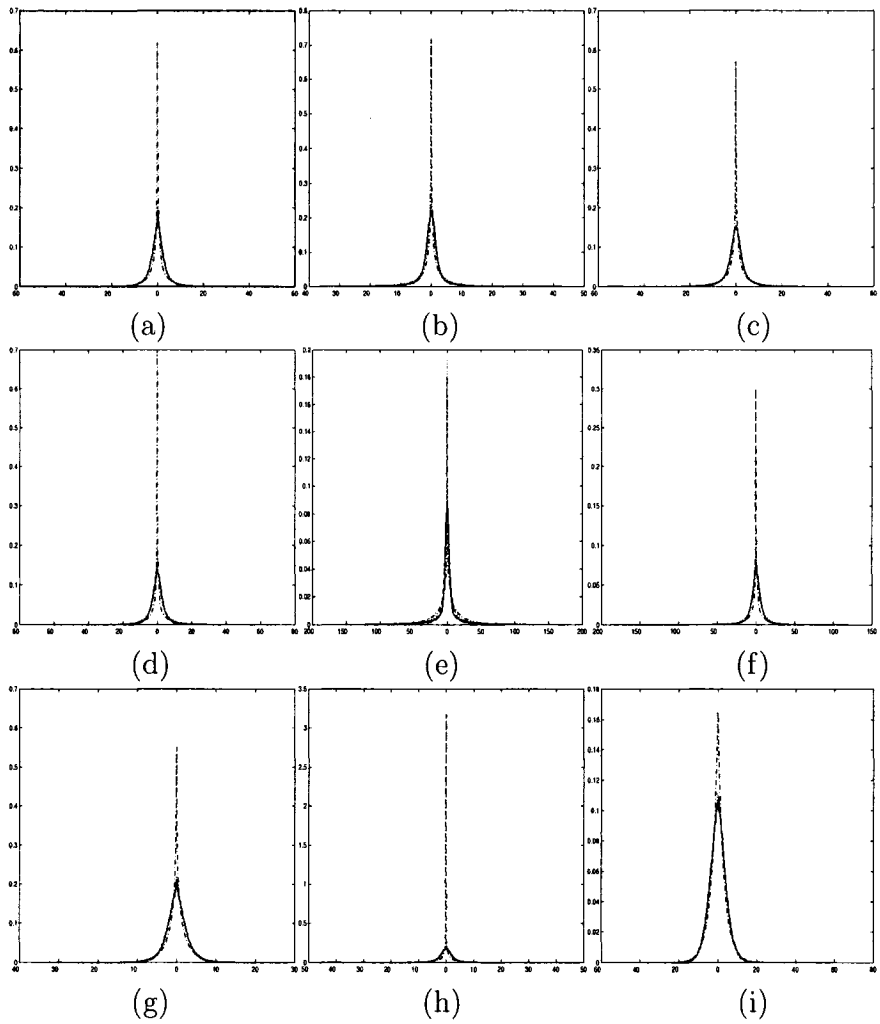

Figure 6.2: Each column shows the plots corresponding to the subbands at level 1 of the *Lena*, *Barbara*, and *Boat* images, respectively. The first, second and third rows show the plots corresponding to the horizontal, vertical and diagonal subbands, respectively. The solid, broken, dotted and dash-dot lines correspond to the empirical, SNIG, GG and BKF PDFs, respectively.

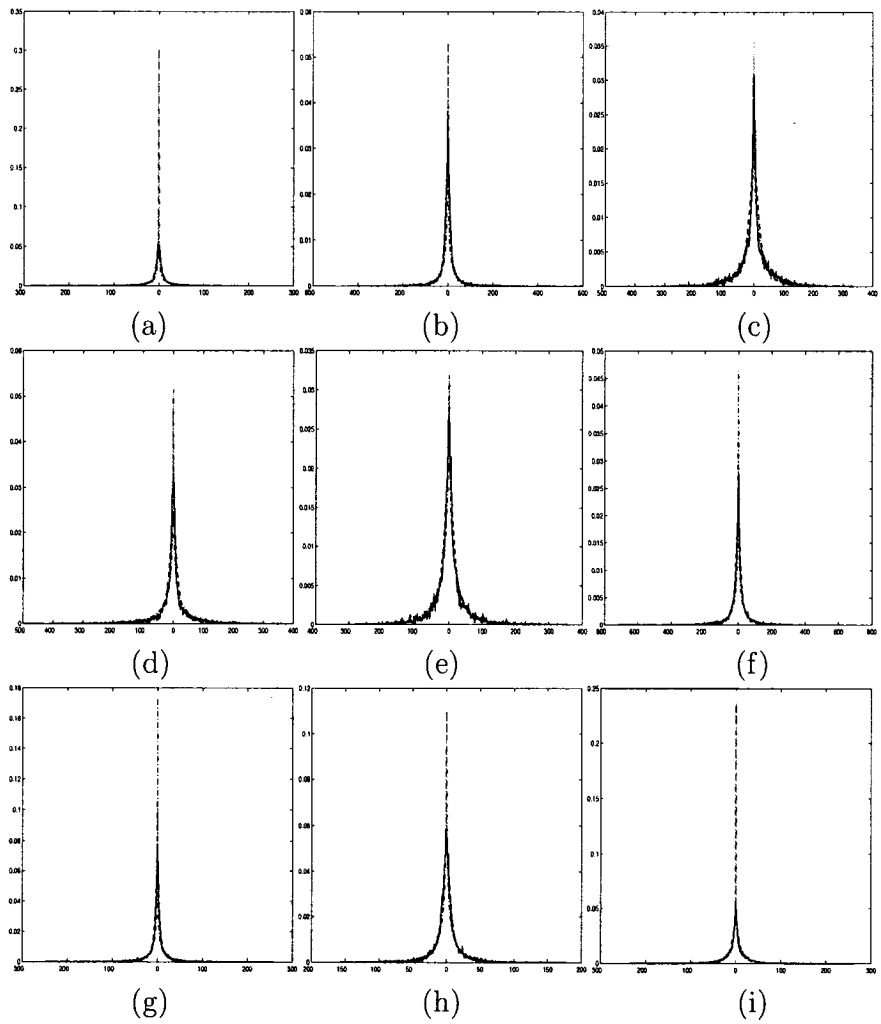

Figure 6.3: Each column shows the plots corresponding to the subbands at level 3 of the *Lena*, *Barbara*, and *Boat* images, respectively. The first, second and third rows show the plots corresponding to the horizontal, vertical and diagonal subbands, respectively. The solid, broken, dotted and dash-dot lines correspond to the empirical, SNIG, GG and BKF PDFs, respectively.

Table 6.3: Values of α estimated from the various subbands of the *Lena*, *Barbara* and *Boat* images. For each case, the first, second and third rows show the values obtained from the corresponding subband at levels 1, 2 and 3, respectively.

Image	LH	HL	HH
Lena	0.1572	0.0593	0.2867
	0.0181	0.0096	0.0194
	0.0062	0.0050	0.0067
Barbara	0.0671	0.0160	0.0812
	0.0094	0.0099	0.0115
	0.0030	0.0061	0.0122
Boat	0.1202	0.0312	0.2967
	0.0159	0.0059	0.0342
	0.0065	0.0034	0.0092

We need to estimate the parameters α and δ from the noisy coefficients to employ the SNIG PDF in denoising. An ML-based method is introduced for estimating the parameters of the SNIG PDF. For estimating the parameters from the noisy coefficients in a subband, let a vector be formed comprising the coefficients in that subband. Let us denote the number of coefficients in the subband by N_b, and the probability corresponding to the n-th coefficient by $P_g(n)$. The proposed estimator is then given by

$$\widehat{\alpha}, \widehat{\delta} = \arg\max_{\alpha,\delta} \sum_{n=1}^{N_b} \ln P_g(n) \tag{6.15}$$

where

$$P_g(n) = \frac{1}{\sqrt{2\pi}\sigma} \int_{-\infty}^{\infty} P_{\alpha,\delta}(g(n) - t) e^{-\frac{t^2}{2\sigma^2}}\, dt \tag{6.16}$$

By replacing $\frac{t}{\sqrt{2}\sigma}$ with a new variable z, (6.16) can be written as

$$P_g(n) = \frac{1}{\sqrt{\pi}} \int_{-\infty}^{\infty} P_{\alpha,\delta}(g(n) - \sqrt{2}\sigma z) e^{-z^2}\, dz \tag{6.17}$$

The integral in (6.17) can be approximated by using the Gauss-Hermite quadra-

ture [53] as

$$\int_{-\infty}^{\infty} P_{\alpha,\delta}(g(n) - \sqrt{2}\sigma z)e^{-z^2}\, dz \cong \sum_{j=1}^{Q} w_j P_{\alpha,\delta}(g(n) - \sqrt{2}\sigma x_j) \tag{6.18}$$

where x_j is the r-th root of the Hermite polynomial of order Q, and w_j is the weight associated with this root. The approximation error corresponding to (6.18) is given by $\frac{Q!\sqrt{\pi}}{2^Q(2Q!)} f^{2Q}(\nu)$, where $f(\nu) = P_{\alpha,\delta}(g(n) - \sqrt{2}\sigma\nu)$, and f^{2Q} is the $2Q$-th derivative of f. Since f can be expressed in the form of a polynomial, the error is considered small [110]. The proposed ML estimator is given by

$$\widehat{\alpha}, \widehat{\delta} = \arg\max_{\alpha,\delta} \sum_{n=1}^{N_b} \ln(\frac{1}{\sqrt{\pi}} \sum_{j=1}^{Q} w_j P_{\alpha,\delta}((g(n) - \sqrt{2}\sigma x_j)) \tag{6.19}$$

Note that the integral is computed at a limited number of points, thus resulting in a reduction of the complexity associated with the process of maximization. Moreover, we have found it sufficient to use the center values corresponding to the bins of a N_g-point histogram of the subband, where $N_g = \sqrt{N_b}$, instead of all the N_b coefficients in the subband, thus providing an additional reduction in the complexity of the maximization process. The standard deviation of the noise is obtained as [55]

$$\widehat{\sigma} = \frac{MAD(g(p,m))}{0.6745}, \qquad g(p,m) \in HH_1 \tag{6.20}$$

A Bayesian MMSE estimator, using $\widehat{\alpha}$, $\widehat{\delta}$ and $\widehat{\sigma}$, is next developed to provide an estimate $\widehat{x}(g)$ from the noisy observations. The Bayesian estimate is given by [111]

$$\widehat{x}(g) = \frac{\int P_\eta(g-x)P_x(x)x dx}{\int P_\eta(g-x)P_x(x)dx} \tag{6.21}$$

Note that (6.21) does not have a closed-form expression for the SNIG PDF. Hence, the Bayesian estimates are obtained numerically using the fast method described in Chapter 2 [46].

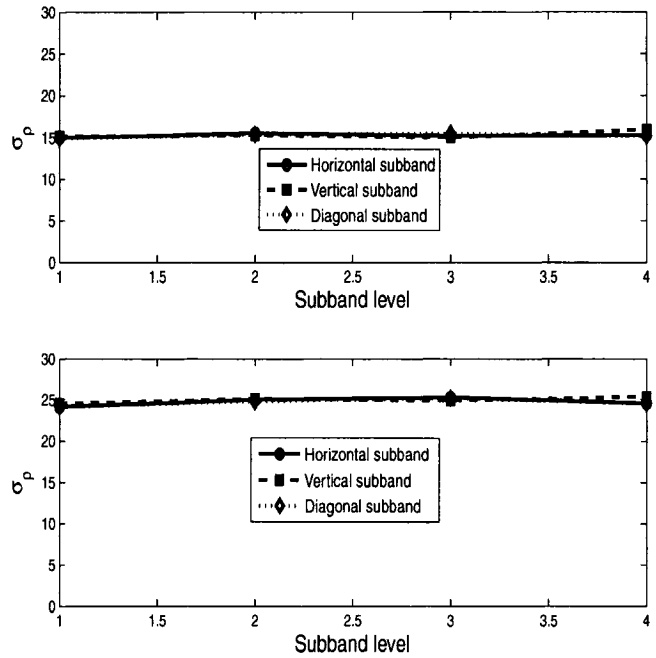

Figure 6.4: Plot of σ_ρ across the subband levels.

Assuming that the Bayesian MMSE estimates are approximately noise-free and using (6.9), we obtain the signal variances that are utilized by the proposed LMMSE estimator to reduce the noise from the wavelet coefficients. This assumption is verified through experiments, in which the values of the standard deviation of the noise removed from the various subbands of noisy *Lena*, *Barbara* and *Boat* (by using the proposed Bayesian MMSE estimator) are calculated for different noise levels. Next, the values obtained for the subbands at the same level and orientation are averaged. The averages are denoted by σ_ρ and plotted in Fig. 6.4 for the noise standard deviations of 15 and 25. It can be seen that the values of σ_ρ are close to the actual values of 15 and 25, thus indicating that the Bayesian MMSE estimates are approximately noise-free. The various steps involved in denoising an image using the proposed method are given in the following in the form of an algorithm.

Proposed Denoising Algorithm	
Step 1	Carry out the orthogonal wavelet decomposition of the noisy image.
Step 2	Estimate the parameters of the SNIG and Gaussian PDFs from the coefficients of the noisy image.
Step 3	Using (6.21) and the values of the parameters acquired in Step 2, obtain the Bayesian MMSE estimates of the noise-free coefficients i. e., $\widehat{x}$.
Step 4	Once $\widehat{x}$ is determined, obtain the variances of the Bayesian MMSE estimates of the coefficients in different subbands using (6.9).
Step 5	Using (6.12) and the values of variances obtained in Step 4, obtain the LMMSE estimates of the noise-free coefficients, namely, $\widetilde{x}$ from (6.13).
Step 6	Obtain the estimates of the variances of the LMMSE filtered coefficients in subbands at levels 3, 2 and 1 using (6.9), where $\widehat{x}$ is replaced by $\widetilde{x}$.
Step 7	Using (6.12) and the variances obtained in Step 6, determine the LMMSE estimates of the noise-free coefficients in the subbands at levels 1 and 2 from (6.13).
Step 8	Perform the inverse wavelet transform to obtain the denoised image using the LMMSE estimates of the noise-free coefficients obtained in Step 7 for the subbands at levels 2 and 1 and in Step 5 for those of the higher levels.

6.4 Simulation Results

Experiments are carried out using eight typical noise-free images, namely, *Aerial*, *Barbara*, *Boat*, *Bridge*, *Brodatz*, *Fingerprint*, *Lena*, and *Mandrill*. The *Boat* and *Fingerprint* images are taken from [108], the *Aerial* and *Brodatz* images from [109], and the rest of the images from the Waterloo Bragzone [64]. A 4-level wavelet decomposition is carried out using the Daubechies' *Symlet* wavelet [47] of order 8. For estimating the parameters of the SNIG PDF, the value of Q in (6.19) is set to 20. The PSNR is used as a performance criterion and calculated (for a particular noise standard deviation) by averaging the values obtained from repeating the experiments four times. For the case of orthogonal wavelet transform, the performance of the proposed method is compared with that of the Bayes-shrink [44], LCHMM [62], Bi-

shrink [94], GSM [97], LAWML and LAWMAP [71], Th-Wiener [72], Arb-Win [101], and ABE rule [103]. Among these methods, the results for the GSM method [97] are obtained with the software provided by its authors in [108]. Table 6.4 shows the values of the PSNR (in dB) for the various methods using the orthogonal DWT. It can be observed from this table that the proposed method performs better than the other techniques in most of the cases. For qualitative comparison, the noisy *Lena* image (for $\sigma = 25$) and the corresponding denoised images obtained by using the various methods are shown in Figs. 6.5 and 6.6. It can be seen from these figures that the proposed method provides images that are of better visual quality than that provided by most of the other techniques. The orthogonal DWT lacks shift-invariance resulting in artifacts such as 'specks' in the smooth regions, and 'ringing' around the edges. However, the proposed method smooths much of these distortions. To illustrate this, a zoomed-in section of the denoised image obtained by the proposed method along with that obtained by three other methods is given in Fig. 6.7. It is seen from the figure that compared to the other methods, the artifacts are relatively more smoothed by the proposed denoising technique. Overall, the proposed method provides an image having a smoother look with less distortions in the homogeneous regions and around the edges. The resulting visual quality is better than that of the other methods, and can be attributed to the use of the proposed modified LMMSE estimator that utilizes both intra and inter-scale dependencies in contrast to the other methods employing LMMSE estimators that use only the intra-scale dependency. In order to show that there is an improvement in the performance achieved by using the modified LMMSE estimator in the proposed method, over that of using only the Bayesian MMSE estimator or the MMSE in conjunction with the LMMSE estimator,

Table 6.4: PSNR values for the various methods using orthogonal wavelet transform

Method \ σ	10	15	20	25
Lena				
Proposed	34.70	32.80	31.42	30.39
3 x 3 LAWML	33.72	31.37	29.63	28.22
3 x 3 LAWMAP	34.25	32.33	31.00	29.96
5 x 5 LAWML	34.13	31.99	30.46	29.24
5 x 5 LAWMAP	34.31	32.36	31.01	29.98
Bayes-shrink	33.56	31.70	30.43	29.54
Th-Wiener	34.5	-	-	30.1
Bi-shrink	34.36	32.36	31.19	30.15
Arb-Win	34.49	32.48	31.06	29.94
ABE rule	32.74	30.48	28.74	27.38
LCHMM	34.50	32.50	31.20	30.10
GSM	34.66	32.77	31.43	30.39
Barbara				
Proposed	33.18	30.83	29.20	27.98
3 x 3 LAWML	32.32	29.72	27.93	26.53
3 x 3 LAWMAP	32.46	30.03	28.39	27.21
5 x 5 LAWML	32.54	30.09	28.43	27.15
5 x 5 LAWMAP	32.57	30.19	28.59	27.42
Bayes-shrink	31.58	29.37	27.81	26.62
Th-Wiener	32.9	-	-	27.8
Bi-shrink	32.25	29.97	28.36	27.16
Arb-Win	32.73	30.34	28.73	27.50
ABE rule	31.28	28.79	27.03	25.71
LCHMM	33.10	30.80	29.20	28.00
GSM	33.13	30.68	29.03	27.83
Aerial				
Proposed	30.22	27.93	26.43	25.35
5 x 5 LAWMAP	29.80	27.60	26.12	25.01
GSM	30.27	27.76	26.17	25.04
Boat				
Proposed	32.76	30.83	29.47	28.42
5 x 5 LAWMAP	32.50	30.56	29.18	28.15
Bi-shrink	32.42	30.55	29.18	28.14
GSM	32.84	30.83	29.42	28.36
Bridge				
Proposed	30.30	28.02	26.55	25.54
5 x 5 LAWMAP	29.96	27.80	26.39	25.36
GSM	30.29	27.83	26.35	25.33
Brodatz				
Proposed	29.87	27.56	26.02	24.89
5 x 5 LAWMAP	29.48	27.21	25.68	24.56
GSM	29.79	27.27	25.71	24.60
Fingerprint				
Proposed	31.75	29.54	28.04	26.91
5 x 5 LAWMAP	31.28	29.04	27.52	26.40
GSM	31.36	29.04	27.56	26.38
Mandrill				
Proposed	29.61	27.37	25.87	24.70
5 x 5 LAWMAP	29.16	27.14	25.72	24.66
GSM	29.91	27.39	25.76	24.59

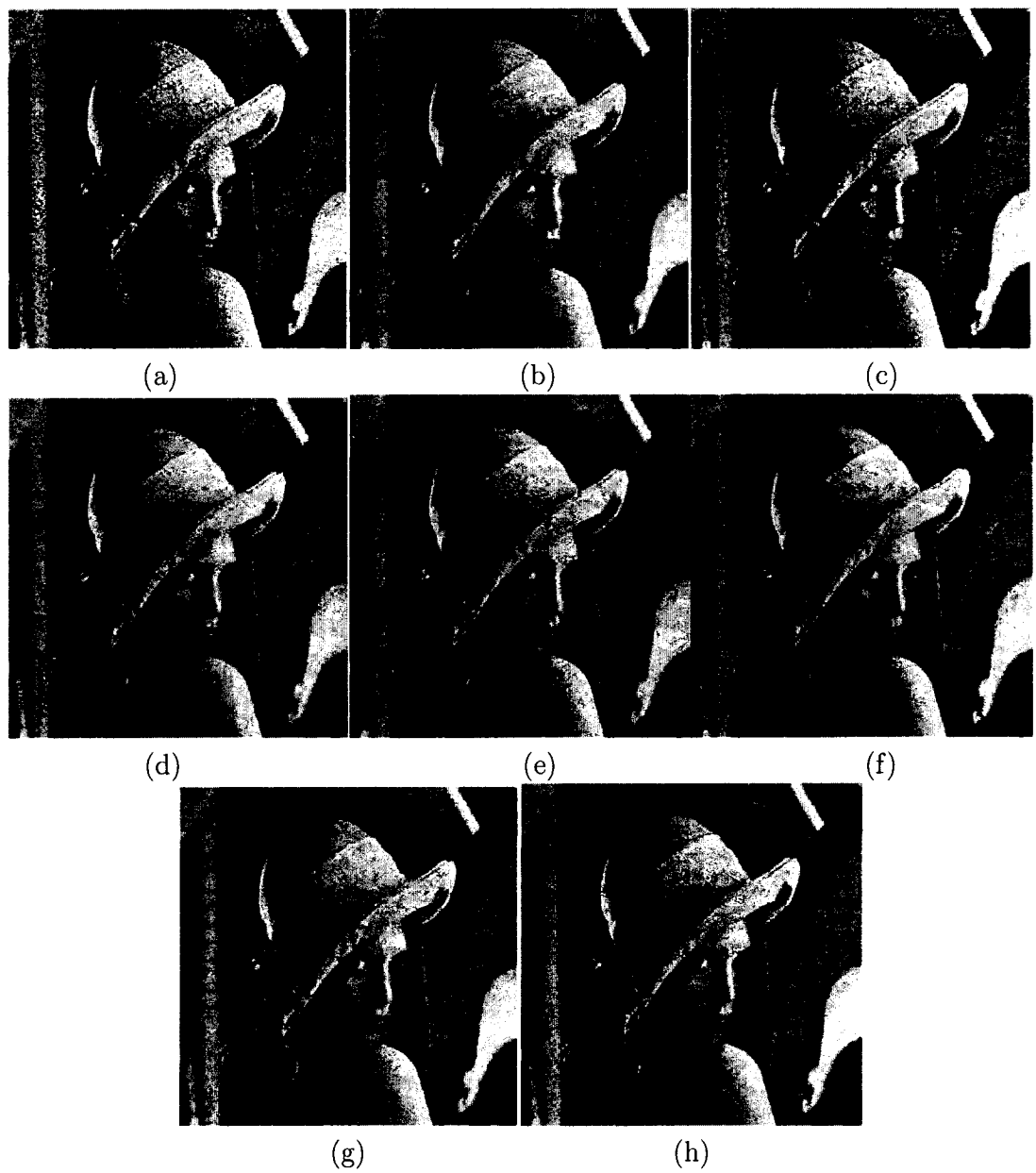

Figure 6.5: (a) Noisy *Lena* image. Denoised images using (b) proposed method, (c) Bayes-shrink, (d) ABE rule, (e) 3×3 LAWMAP, (f) 5×5 LAWMAP, (g) Arb-Win, and (h) GSM.

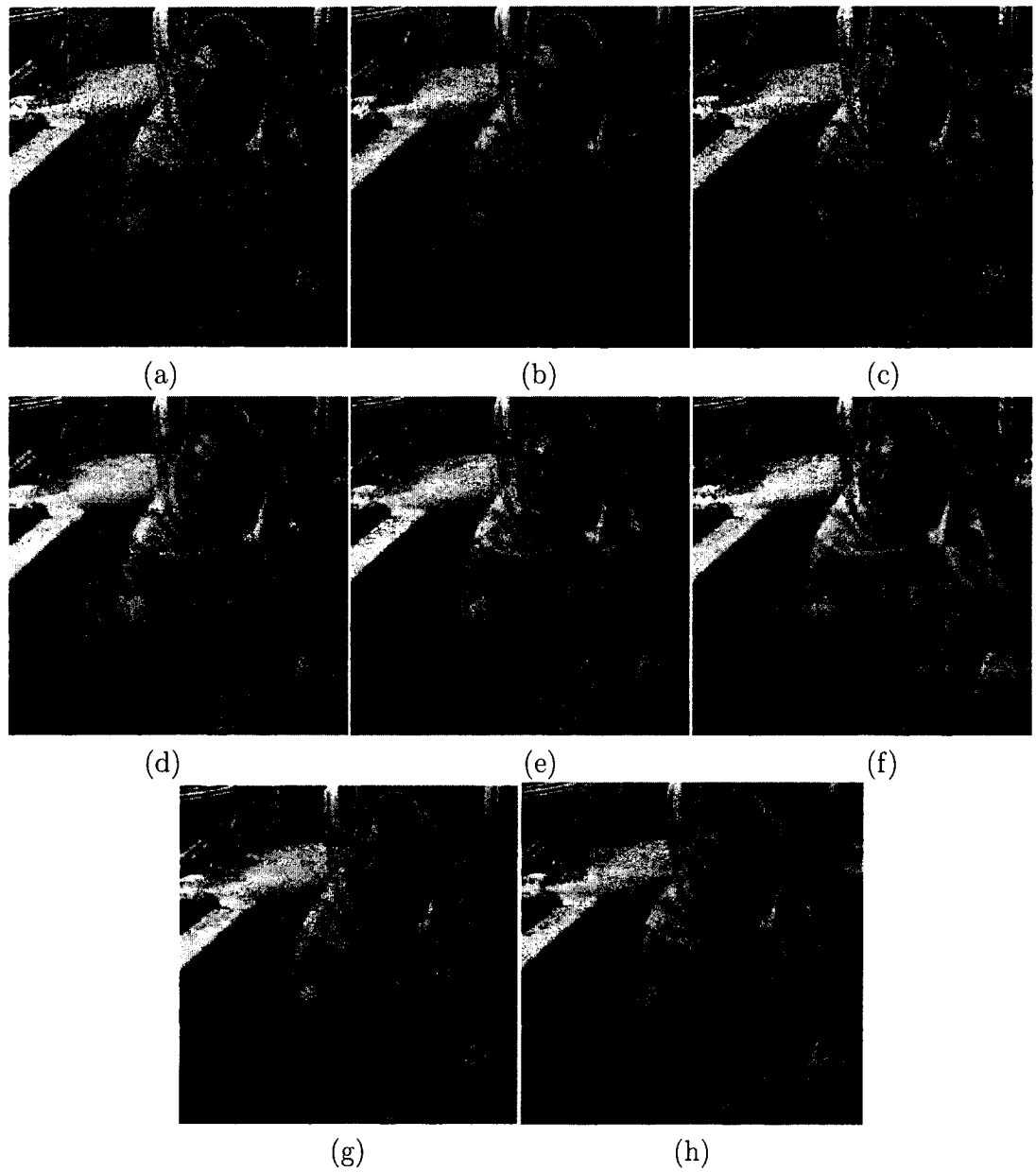

Figure 6.6: (a) Noisy *Barbara* image. Denoised images using (b) proposed method, (c) Bayes-shrink, (d) ABE rule, (e) 3×3 LAWMAP, (f) 5×5 LAWMAP, (g) Arb-Win, and (g) GSM.

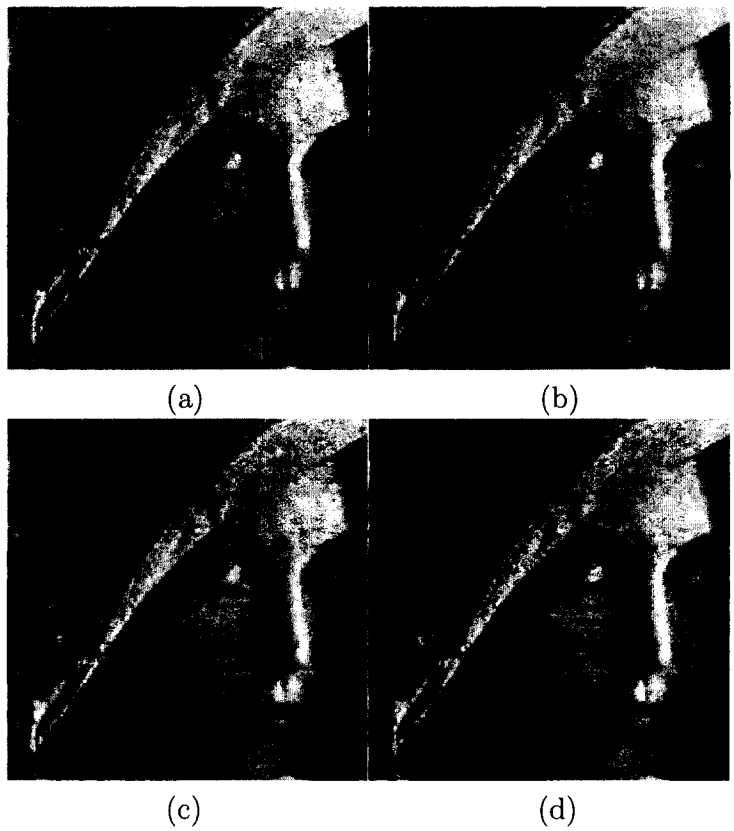

Figure 6.7: Zoomed-in section of denoised *Lena* image obtained using (a) proposed method, (b) 3×3 LAWMAP, (c) 5×5 LAWMAP, (d) Arb-Win.

we obtain the PSNR values for the two latter cases using three test images, *Lena*, *Barbara* and *Boat*. For this purpose, the images are corrupted with noise having various standard deviations. The noisy images are then denoised using only the Bayesian MMSE estimator, or the MMSE in conjunction with the LMMSE estimator in the proposed method. The corresponding PSNR values along with those of the proposed method using the MMSE and modified LMMSE estimators are listed in Table 6.5. From this table, it is clear that a significant performance improvement is achieved by the addition of the LMMSE estimator. On average, the gain in PSNR over using the Bayesian MMSE estimator alone is 1.35 dB. Note that the modified LMMSE estimator utilizes signal variances obtained using local neighbors and the standard deviation of the parent. Thus, both intra-scale and inter-scale information are exploited in the LMMSE estimator that contribute to this improvement in performance. The average improvement introduced by the modification in the LMMSE estimator over that of using the non-modified one is 0.13 dB. This small improvement obtained by incorporating the inter-scale dependency through the use of the parent coefficient's standard deviation is in agreement with the observation of Liu and Moulin in [30], where it is shown that that incorporating the inter-scale dependency on top of the intra-scale dependency results in a marginal improvement in performance. It should also be noted that the performance of the LMMSE estimator is considerably improved by using signal variances estimated from the Bayesian MMSE estimates that are approximately noise-free. This can be observed by comparing the results of the proposed method for the *Lena* and *Barbara* images with those obtained by the Th-Wiener [72] where the variances are obtained from thresholded coefficients, or those of LAWML [71] where the variances are obtained directly from the noisy coefficients. In order to investigate the effect of repeating the proposed method on the objective as well as the subjective

Table 6.5: PSNR values for the proposed method using the Bayesian MMSE estimator only, MMSE and LMMSE estimators, and MMSE and modified LMMSE estimators for the images, *Lena*, *Barbara* and *Boat*

Estimators used in the proposed method	Standard deviation of noise			
	10	15	20	25
Lena				
MMSE only	33.89	32.01	30.71	29.75
MMSE and LMMSE	34.39	32.59	31.26	30.28
MMSE and modified LMMSE	34.63	32.75	31.37	30.36
Barbara				
MMSE only	31.84	29.49	27.89	26.70
MMSE and LMMSE	32.88	30.68	29.12	27.93
MMSE and modified LMMSE	33.02	30.73	29.20	27.98
Boat				
MMSE only	32.16	30.22	28.83	27.82
MMSE and LMMSE	32.63	30.72	29.40	28.34
MMSE and modified LMMSE	32.76	30.83	29.47	28.42

quality of the denoised image, the proposed method is repeatedly applied to the noisy *Lena*, *Barbara* and *Boat* images corrupted with noise of various standard deviations. In view of the space considerations, the results for only the *Lena* image for different number of repeatations for a noise standard deviation of 25 are shown in Fig. 6.8. It is seen that repeated application provides little improvement either in terms of the objective or the subjective quality. Moreover, it requires additional computation, which is obviously not worthwhile.

As mentioned earlier, an orthogonal DWT is not shift-invariant. Since the redundant wavelet transforms are shift-invariant, denoising methods employing such transforms can offer a performance better than that using the orthogonal DWT. However, the lack of the shift-invariance property associated with the orthogonal DWT can be overcome by using the cycle-spinning technique proposed in [61]. It has been shown in [62] that by implementing the orthogonal DWT-based denoising method in cycle-spinning mode, a performance equivalent to those using the traditional redundant

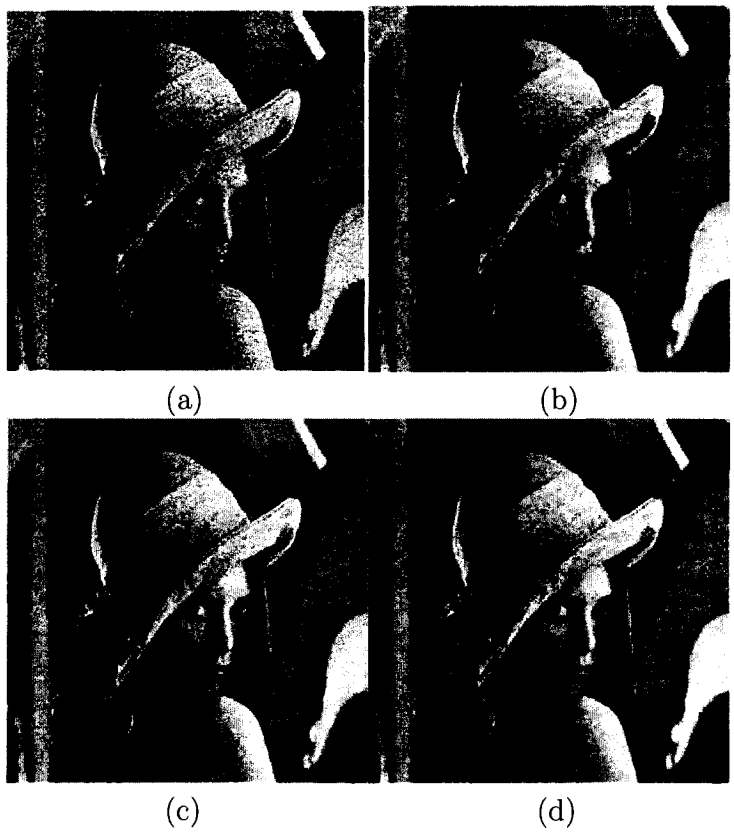

Figure 6.8: Denoised *Lena* image obtained by repeated application of the proposed method. (a) Original noisy image (PSNR=20.17 dB), (b) Denoised image after the first application (PSNR=30.38 dB), (c) Denoised image after the second application (PSNR=30.50 dB), (d) Denoised image after the third application (PSNR=30.50 dB).

wavelet transforms, for example, the stationary wavelet transform (SWT), can be achieved. In view of this, we consider the proposed method with cycle-spinning, where the noisy image is circularly shifted by zero, one, two and three pixels in both the horizontal and vertical directions. It should be mentioned that in the proposed method the estimation of SNIG parameters is carried out for the zero shift only. Recently, a new redundant wavelet transform called the dual-tree complex wavelet transform (DT-CWT) has been proposed [87], that in addition to being shift-invariant and computationally less demanding than the SWT, provides better directional and

rotational selectivity. Therefore, we also extend our method to the DT-CWT domain. The results of our method are compared with those of [62], [98], [97], [99], and [104]. The results for [97] and [99] are obtained using the softwares provided in [108] and [92], respectively. Table 6.6 contains the PSNR values obtained using the various methods. It can be seen that the values of the PSNR obtained by using the proposed method in DT-CWT domain are higher than that obtained by the other methods except for that of [97] in which case the PSNR values are comparable. Fig. 6.9 and 6.10 show the denoised images obtained by using the proposed method with cycle-spinning and DT-CWT for the noisy *Lena* and *Barbara* (for $\sigma = 25$) as well as the corresponding denoised images obtained with the Probshrink [99] and GSM [97] methods. It can be observed that the proposed method provides denoised images that are of improved visual quality and comparable to that of [97]. In comparison to the GSM method [97], the proposed method requires less computational time. For example, on an Intel Pentium IV 2.4 GHz personal computer with 768 MB RAM, the average CPU times (in MATLAB) to process the images of 256×256 and 512×512 pixels for our method are 9.17 secs and 26 secs, respectively. The corresponding CPU times required by the GSM method [97], using the software available in [108], are 27.35 secs and 123.64 secs, respectively.

The comparatively low CPU time of the proposed method can be explained as follows. The proposed method has only two steps. For an image of $D_x \times D_y$ pixels, the complexity associated with the Bayesian MMSE estimation and LMMSE estimation steps are given by $O(C_B)$ and $O(C_L)$, respectively, where $C_B = D_k D_I log_2 D_I$, $C_L = D_k M D_I^2$, $D_k = D_c D_L$, the redundancy factor $D_L = 4$, the number of orientations $D_c = 3$, $D_I = \sqrt{D_x \times D_y}$, and the window size $M = 9$. The overall complexity of the proposed method is roughly $O(C_L)$ as $C_L >> C_B$. On the other hand, the

complexity of the GSM method is roughly $O(D_I^2 R_D)$, R_D being $2N_n K_o S_z$, where the neighborhood size $N_n = 10$, the number of orientations $K_o = 8$, and the length of the sampling grid $S_z = 13$. Since $R_D >> D_k M$, it is obvious that the proposed method has a complexity that is much smaller than that of the GSM method, and hence, requires a relatively low CPU time.

Table 6.6: PSNR values for the various methods using redundant wavelet transform

Method \ σ	10	15	20	25
Lena				
Proposed (cycle-spinning)	35.06	33.17	31.85	30.76
Proposed (DT-CWT)	35.46	33.62	32.27	31.36
LCHMM-SI	35.00	33.00	31.70	30.60
SAOE	34.90	33.00	31.92	30.60
Proposed in [98]	34.75	33.03	31.87	30.89
GSM	35.63	33.67	32.68	31.70
Probshrink	35.09	33.26	31.92	30.89
Barbara				
Proposed (cycle-spinning)	33.70	31.40	29.75	28.45
Proposed (DT-CWT)	34.38	32.10	30.42	29.22
LCHMM-SI	33.60	31.40	29.70	28.50
SAOE	33.30	31.10	29.40	28.20
GSM	34.47	32.20	30.58	29.32
Probshrink	33.83	31.44	29.77	28.47
Aerial				
Proposed (cycle-spinning)	30.69	28.38	26.87	25.78
Proposed (DT-CWT)	31.01	28.60	26.94	25.85
GSM	31.08	28.72	27.17	26.03
Probshrink	31.08	27.76	26.17	25.04
Boat				
Proposed (cycle-spinning)	33.24	31.31	29.92	28.90
Proposed (DT-CWT)	33.48	31.50	30.11	29.01
Proposed in [98]	33.26	31.22	30.00	28.95
GSM	33.58	31.69	30.36	29.33
Probshrink	33.23	31.29	29.92	28.87
Bridge				
Proposed (cycle-spinning)	30.65	28.35	26.88	25.88
Proposed (DT-CWT)	31.04	28.59	27.05	25.96
GSM [97]	30.95	28.59	27.12	26.08
Probshrink [99]	30.52	28.14	26.66	25.65
Brodatz				
Proposed (cycle-spinning)	30.32	27.75	26.46	25.35
Proposed (DT-CWT)	30.51	28.10	26.55	25.39
GSM	30.46	28.08	26.53	25.41
Probshrink	29.96	27.56	26.05	24.95
Fingerprint				
Proposed (cycle-spinning)	32.25	30.10	28.59	27.42
Proposed (DT-CWT)	32.37	30.16	28.65	27.74
GSM	32.44	30.14	28.59	27.44
Probshrink	31.93	29.70	28.13	26.94
Mandrill				
Proposed (cycle-spinning)	29.98	27.73	26.18	25.07
Proposed (DT-CWT)	30.67	28.23	26.56	25.37
GSM	30.55	28.15	26.58	25.44
Probshrink	30.00	27.61	26.00	24.85

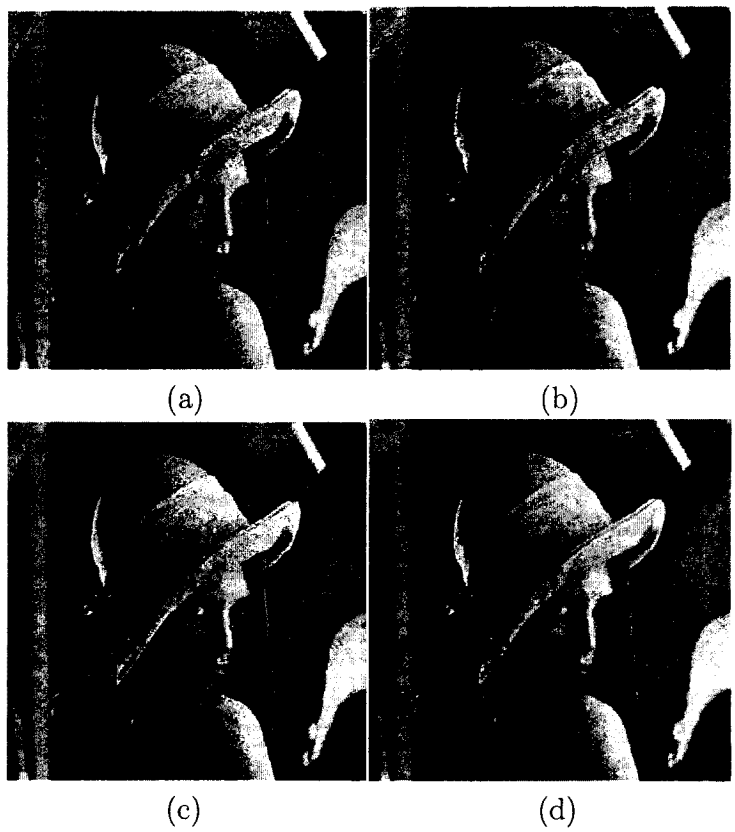

Figure 6.9: Denoised *Lena* images using (a) proposed method (with cycle-spinning), (b) proposed method (with DT-CWT), (c) Probshrink, and (d) GSM.

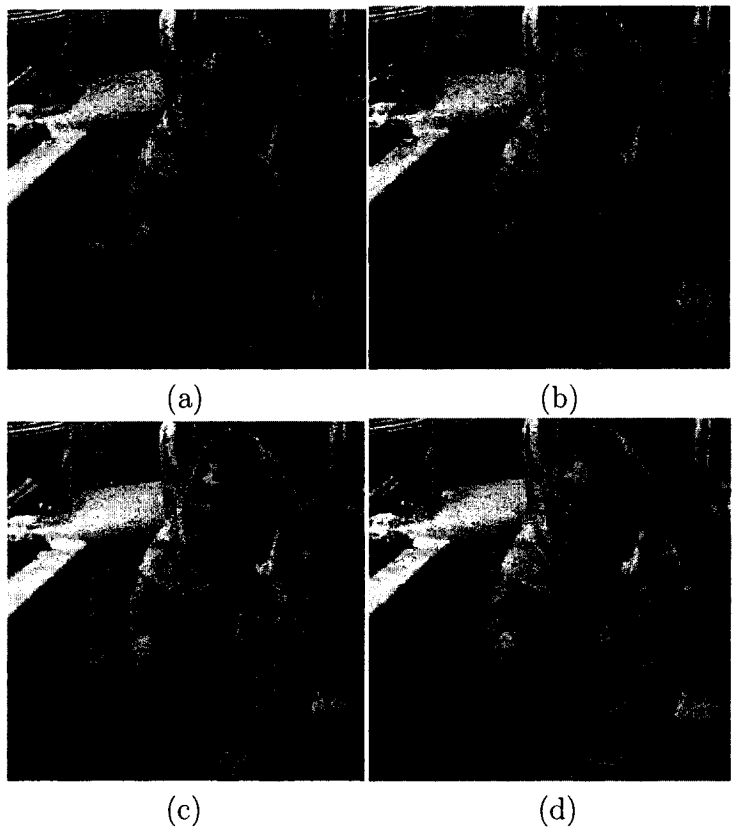

Figure 6.10: Denoised *Barbara* images using (a) proposed method (with cycle-spinning), (b) proposed method (with DT-CWT), (c) Probshrink, and (d) GSM.

6.5 Conclusion

A new spatially-adaptive method using wavelet transform has been proposed in this chapter for reducing noise in images corrupted by additive white Gaussian noise. It has been shown that the SNIG PDF is very well suited to model the wavelet coefficients. A maximum likelihood-based technique has been proposed for estimating the parameters of the PDF, wherein the Gauss-Hermite quadrature approximation has been used to carry out the maximization process in a computationally efficient manner. A Bayesian minimum mean squared error estimator has been developed using the PDF. The Bayesian estimates have been employed as preliminary estimates of the noise-free coefficients, which are utilized to obtain the signal variances, using a relatively small local neighborhood, thus reducing the computational load. A modified linear minimum mean squared error estimator that takes into consideration both the intra-scale and inter-scale information has been introduced. Experiments using typical noise-free images corrupted with simulated noise have been carried out to investigate the performance of the proposed method, and compared it with those of some of the existing denoising techniques. It has been shown that the proposed method not only performs better than several standard methods in terms of the peak signal-to-noise ratio, but also provides images with good visual quality. Besides, the proposed method gives a performance competitive to that of the state-of-the-art GSM method with a considerably less computational complexity.

Chapter 7

Conclusion

7.1 Concluding Remarks

Synthetic aperture radar (SAR) and ultrasound are powerful imaging systems that are extensively used in remote sensing and medical diagnosis, respectively. A major problem with these systems is that the resulting images are inherently corrupted by speckle noise. The objective of this thesis has been to develop efficient wavelet-based techniques for reducing the speckle substantially in the SAR and medical ultrasound images as compared to that achieved by the existing methods, without unduly increasing the computational cost. The performance improvement has been achieved by using efficient statistical models for developing Bayesian MMAE, MMSE and MAP estimators and incorporating the spatial dependence of the wavelet coefficients with the Bayesian estimation processes. Fast and efficient techniques have been proposed for estimating the model parameters, while incorporating the dependencies of the wavelet coefficients.

An efficient method, that uses the Cauchy PDF to model the coefficients corresponding to the log-transformed reflectivity has been introduced, for despeckling the SAR images. By using the spatial information to modify the Bayesian estimates,

a considerable improvement in denoising has been achieved. This improvement is due to the incorporation of the spatial dependencies with the Bayesian estimation processes.

It has been shown through experimental studies that the symmetric normal inverse Gaussian (SNIG) PDF is highly suitable for modelling the wavelet coefficients of the log-transformed reflectivity corresponding to both the SAR and medical ultrasound images. Efficient methods have been developed using the SNIG PDF for reducing the speckle in these kinds of images. By using the SNIG PDF, it is possible to achieve a substantial reduction in the speckle as compared to the existing methods with a moderate increase in the complexity. The proposed techniques, although homomorphic, cause very little bias. It is worth mentioning that among the two methods to despeckle the SAR images, the one utilizing the SNIG PDF is the most effective.

An alternative fast and robust technique to despeckle the medical ultrasound images, that takes the heavy-tailedness of the log-transformed speckle into account, has been introduced. By incorporating the heavy-tailedness of the log-transformed speckle in the Bayesian estimator, a better performance in denoising has been achieved over that obtained by the commonly-used Gaussian model. The proposed methods for despeckling the ultrasound images are robust enough to withstand the wide variability of the image features and to accommodate the processing of the images on a case-by-case basis.

Finally, it has been shown that the SNIG PDF is also highly suitable for modelling the wavelet coefficients corresponding to the natural images, and this has been used to advantage for developing an efficient method for the classical case in reducing the AWGN from these images.

7.2 Scope for Further Work

The research work undertaken in this thesis can be extended in several respects. One interesting area of investigation would be the development of efficient despeckling techniques using the SNIG PDF for reducing the partially-developed speckle, observed in highly heterogeneous regions of the image. Another challenging problem is the direct incorporation of the speckle correlation in the Bayesian estimators.

As mentioned in this thesis, the distribution of the log-transformed speckle noise is actually given by a Fisher-Tippet PDF. Therefore, it is worthwhile investigating as to whether it is possible to develop an effective despeckling technique that incorporates the Fisher-Tippet PDF in modelling the wavelet coefficients of the log-transformed speckle noise. An obvious challenge is to develop a Bayesian estimator that uses the Fisher-Tippet PDF in closed form, so as to reduce the computational cost. Even though non-homomorphic methods for despeckling can be developed using the SNIG PDF, a problem with such an approach is the dependency of the noise on the signal. Therefore, it is necessary to develop an efficient method to discriminate between the signal and noise coefficients, in order to denoise the corrupted signal.

References

[1] R. C. Gonzalez and R. E. Woods, *Digital Image Processing.* USA: Prentice Hall Ltd., 2002.

[2] S. Kuttikkad and R. Chellappa, "Statistical modeling and analysis of high-resolution synthetic aperture radar images," *Statistics and Computing*, vol. 10, pp. 133–145, 2000.

[3] J. C. Bamber and C. Daft, "Adaptive filtering for reduction of speckle in ultrasonic pulse-echo images," *Ultrasonics*, pp. 41–44, 1986.

[4] E. R. Ritenour, T. R. Nelson, and T. Raff, "Application of median filter to digital radiographic images," in *Proc. of ICASSP*, 1984, pp. 251–254.

[5] J. S. Lee, "Speckle analysis and smoothing of synthetic aperture radar images," *Computer Graphics and Image Processing*, vol. 17, pp. 24–32, 1981.

[6] ——, "Refined filtering of image noise using local statistics," *Computer Graphics and Image Processing*, vol. 15, pp. 380–389, 1981.

[7] ——, "A simple speckle smoothing algorithm for synthetic aperture radar images," *IEEE Trans. on Systems, Man and Cybernetics*, vol. 13, pp. 85–89, 1983.

[8] V. S. Frost, J. A. Stiles, K. S. Shanumugan, and J. C. Holtzman, "A model for radar images and its application to adaptive digital filtering of multiplicative noise," *IEEE Trans. PAMI*, vol. 4, pp. 157–165, 1986.

[9] D. T. Kuan, A. A. Sawchuk, T. C. Strand, and P. Chavel, "Adaptive noise smoothing filter for images with signal dependent noise," *IEEE Trans. PAMI*, vol. 7, pp. 165–177, 1987.

[10] D. T. Kuan, "Adaptive restoration of images with speckle," *IEEE Trans. Acoustics, Speech and Signal Processing*, vol. 35, pp. 373–383, 1987.

[11] A. Lopes, E. Nezry, R. Touzi, and H. Laur, "Structure detection and statistical adaptive speckle filtering of SAR images," *Int. Journal of Remote Sensing*, vol. 14, pp. 1735–1758, 1993.

[12] A. Lopes, R. Touzi, and E. Nezry, "Adaptive speckle filters and scene heterogenity," *IEEE Trans. on Geoscience and Remote Sensing*, vol. 28, pp. 992–1000, 1990.

[13] M. Karaman, M. A. Kutay, and G. Bozdagi, "An adaptive speckle suppression filter for medical ultrasound imaging," *IEEE Trans. on Medical Imaging*, vol. 14, pp. 283–292, 1995.

[14] T. Loupas, W. N. Mcdicken, and P. L. Allan, "An adaptive weighted median filter for speckle suppression in medical ultrasonic images," *IEEE Trans. Circuits and Systems*, vol. 36, pp. 129–135, 1989.

[15] J. S. Lee and I. Jurkevich, "Speckle filtering of synthetic aperture radar images: A review," *Remote Sensing Reviews*, vol. 8, pp. 313–340, 1994.

[16] A. K. Jain, *Fundamentals of Digital Image Processing.* Englewood Cliffs, USA: Prentice-Hall Ltd., 1989.

[17] B. Vidakovic, *Statistical Modeling by Wavelets.* New York, USA: John Wiley and Sons, 1999.

[18] R. Ogden, *Essential Wavelets for Statistical Applications and Data Analysis.* Boston MA, USA: Birkhauser, 1997.

[19] M. Crouse, R. Nowak, and R. Baraniuk, "Wavelet-based statistical signal processing using hidden Markov models," *IEEE Trans. on Signal Processing*, vol. 46, pp. 886–902, 1998.

[20] H. Guo, J. E. Odegard, M. Lang, R. Gopinath, I. W. Selesnick, and C. S. Burrus, "Wavelet-based speckle reduction with application to SAR based ATD/R," in *Proc. of ICIP*, 1994, pp. 75–79.

[21] X. Zong, A. F. Laine, and E. A. Geiser, "Speckle reduction and contrast enhancement of echocardiograms via multiscale nonlinear processing," *IEEE Trans. on Medical Imaging*, vol. 17, pp. 532–540, 1998.

[22] X. Hao, S. Gao, and X. Gao, "A novel multiscale nonlinear thresholding method for ultrasound speckle suppression," *IEEE Trans. on Medical Imaging*, vol. 18, pp. 787–794, 1999.

[23] L. Gagnon and A. Jouan, "Speckle filtering of SAR images- a comparative study between complex wavelet-based and standard filters," in *Proc. of SPIE*, vol. 3169, 1997, pp. 80–91.

[24] J. R. Sveinsson and J. A. Benediktsson, "Almost translation inavriant wavelet transformations for speckle reduction of SAR images," *IEEE Trans. on Geoscience and Remote Sensing*, vol. 41, pp. 2404–2408, 2003.

[25] E. H. Ng, K. T. Wong, and J. C. L. Lam, "Speckle noise reduction via rotated elliptical-thresholding in a homomorphic complex wavelet domain," in *Proc. of ICIP*, 2005, pp. 585–588.

[26] S. Gupta, R. C. Chauhan, and S. C. Saxena, "Wavelet-based statistical approach for speckle reduction in medical ultrasound images," *Medical and Biological Engineering and Computing*, vol. 42, pp. 189–192, 2004.

[27] Z. Zeng and I. Cumming, "Bayesian speckle noise reduction using the discrete wavelet transform," in *Proc. of IGARSS*, 1998, pp. 7–9.

[28] A. Achim, P. Tsakalides, and A. Bezarianos, "Novel Bayesian multiscale method for speckle removal in medical ultrasound images," *IEEE Trans. on Medical Imaging*, vol. 20, pp. 772–783, 2001.

[29] ——, "SAR image denoising via Bayesian wavelet shrinkage based on heavy-tailed modeling," *IEEE Trans. on Geoscience and Remote Sensing*, vol. 41, pp. 1413–1421, 2003.

[30] J. Liu and P. Moulin, "Information theoretic analysis of interscale and intrascale dependencies between image wavelet coefficients," *IEEE Trans. on Image Processing*, vol. 10, pp. 1647–1658, 2001.

[31] S. Fukuda and H. Hirosawa, "Suppression of speckle in synthetic aperture radar images using wavelet," *Int. Journal of Remote Sensing*, vol. 19, pp. 507–519, 1998.

[32] Y. Hawwar and A. Reza, "Spatially adaptive multiplicative noise image denoising technique," *IEEE Trans. on Image Processing*, vol. 11, pp. 1397–1404, 2002.

[33] M. I. H. Bhuiyan, M. O. Ahmad, and M. N. S. Swamy, "A new wavelet-based method for despeckling SAR images," in *Proc. of IEEE NEWCAS Conference*, 2005, pp. 345–348.

[34] A. Pizurica, W. Philips, I. Lemahieu, and M. Acheroy, "Despeckling SAR images using wavelets and a new class of adaptive shrinkage estimators," in *Proc. of ICIP*, 2001, pp. 233–236.

[35] H. Xie, L. Pierce, and F. T. Ulaby, "SAR speckle reduction using wavelet denoising and Markov random field modeling," *IEEE Trans. on Geoscience and Remote Sensing*, vol. 40, pp. 2196–2212, 2002.

[36] S. Foucher, G. B. Benie, and J. M. Boucher, "Multiscale MAP filtering of SAR images," *IEEE Trans. on Image Processing*, vol. 10, pp. 49–60, 2001.

[37] S. SolbØ and T. Eltoft, "Homomorphic wavelet-based statistical despeckling of SAR images," *IEEE Trans. on Geoscience and Remote Sensing*, vol. 42, pp. 711–721, 2004.

[38] ——, "Γ-WMAP: A statistical speckle filter operating in the wavelet domain," *Int. Journal of Remote Sensing*, vol. 25, pp. 1019–1036, 2004.

[39] F. Argenti, T. Bianchi, and L. Alparone, "Multiresolution MAP despeckling of SAR images based on locally adaptive generalized Gaussian pdf modelling," *IEEE Trans. on Image Processing*, vol. 15, pp. 3385–3399, 2006.

[40] F. Argenti, L. Alparone, and S. Baronti, "Speckle removal from SAR images in the undecimated wavelet domain," *IEEE Trans. on Geoscience and Remote Sensing*, vol. 40, pp. 2363–2374, 2002.

[41] A. Pizurica, W. Philips, I. Lemahieu, and M. Acheroy, "A versatile wavelet domain noise filtration technique for medical imaging," *IEEE Trans. on Medical Imaging*, vol. 22, pp. 323–331, 2003.

[42] F. Argenti and G. Toricelli, "Speckle suppression in ultrasonic images based on undecimated wavelets," *EURASIP Journal of Applied Signal Processing*, vol. 5, pp. 470–478, 2003.

[43] N. Gupta, M. N. S. Swamy, and E. I. Plotkin, "Despeckling of medical ultrasound images using data and rate adaptive lossy compression," *IEEE Trans. on Medical Imaging*, vol. 24, pp. 743–754, 2005.

[44] S. G. Chang, B. Yu, and M. Vetterli, "Adaptive wavelet thresholding for image denoising and compression," *IEEE Trans. on Image Processing*, vol. 9, pp. 1532–1546, 2000.

[45] M. I. H. Bhuiyan, M. O. Ahmad, and M. N. S. Swamy, "A new homomorphic Bayesian wavelet-based MMAE filter for despeckling SAR images," in *Proc. of IEEE International Symposium on Circuits and Systems*, 2005, pp. 4935–4938.

[46] ——, "Spatially-adaptive wavelet-based method using the Cauchy prior for denoising the SAR images," *IEEE Tran. on Circuits, Systems and Video Technology*, pp. 500–507, 2007.

[47] S. Mallat, "A theory for multiresolution signal decomposition: The wavelet representation," *IEEE Trans. PAMI*, vol. 11, pp. 674–693, 1989.

[48] C. Oliver and S. Quegan, *Understanding Synthetic Aperture Radar Images.* Raleigh, NC, USA: SciTech Publishing Inc., 2004.

[49] H. Xie, L. Pierce, and F. T. Ulaby, "Statistical properties of logarithmically transformed speckle," *IEEE Trans. on Geoscience and Remote Sensing*, vol. 40, pp. 721–727, 2002.

[50] J. Ilow and D. Hatzinakos, "Application of the empirical characteristic function to estimation and detection problems," *Signal Processing*, vol. 65, pp. 199–219, 1998.

[51] H. H. Arsenault and G. April, "Properties of speckle integrated with a finite aperture and logarithmically transformed," *Journal of Optical Society of America*, vol. 66, pp. 1160–1163, 1976.

[52] H. V. Poor, *An Introduction to Signal Detection and Estimation.* New York, USA: Springer-Verlag, 1988.

[53] W. H. Press, S. A. Teukolsky, W. T. Vellerling, and B. P. Flannery, *Numerical Recipes in C: The Art of Scientific Computing.* UK: Cambridge University Press, 1999.

[54] A. Hyvarinen, "Sparse code shrinkage: Denoising of nongaussian data by maximum likelihood estimation," *Neural Computation*, vol. 11, pp. 1739–1768, 1999.

[55] D. L. Donoho, "Denoising by soft-thresholding," *IEEE Trans. on Information Theory*, vol. 41, pp. 613–627, 1995.

[56] R. W. Buccigrosi and E. P. Simoncelli, "Image compression via joint statistical characterization in the wavelet domain," *IEEE Trans. on Image Processing*, vol. 8, pp. 1688–1701, 1999.

[57] Y. Yoo, A. Ortega, and B. Yu, "Image subband coding using context-based classification and adaptive quantization," *IEEE Trans. on Image Processing*, vol. 8, pp. 1702–1715, 1999.

[58] S. G. Chang, B. Yu, and M. Vetterli, "Spatially adaptive wavelet thresholding with context modeling for image denoising," *IEEE Trans. on Image Processing*, vol. 9, pp. 1522–1531, 2000.

[59] J. Zhong and R. Ning, "Image denoising based on wavelets and multifractals for singularity detection," *IEEE Trans. on Image Processing*, vol. 14, pp. 1435–1447, 2005.

[60] I. Daubechies, *Ten Lectures on Wavelets.* Philadelphia, USA: SIAM, 1992.

[61] R. R. Coifman and D. L. Donoho, "Translation invariant denoising," *Wavelets and Statistics, Springer-Verlag, Berlin, Germany*, 1995.

[62] G. Fan and X. Xia, "Image denoising using a local contextual hidden Markov model in the wavelet domain," *IEEE Signal Processing Letters*, vol. 8, pp. 125–128, 2001.

[63] Centre for vision, speech and signal processing. University of Surrey, UK. [Online]. Available: http://www.ee.surrey.ac.uk/Research/VSSP/demos/corners/originals.html.

[64] Waterloo BragZone. University of Waterloo, Canada. [Online]. Available: http://links.uwaterloo.ca/bragzone.base.html.

[65] Z. Wang, A. C. Bovik, H. R. Sheikh, and E. P. Simoncelli, "Image quality aasessment: From error visibility to structural similarity," *IEEE Trans. on Image Processing*, vol. 13, pp. 600–612, 2004.

[66] K. Hirakawa and T. W. Parks, "Image denoising using total least squares," *IEEE Trans. on Image Processing*, vol. 15, pp. 2730–2742, 2006.

[67] Jet Propulsion Laboratory. AIRSAR program. [Online]. Available: http://airsar.jpl.nasa.gov/.

[68] M. I. H. Bhuiyan, M. O. Ahmad, and M. N. S. Swamy, "Wavelet-based spatially adaptive method for despeckling SAR images," in *Proc. of IEEE International Symposium on Circuits and Systems*, 2006, pp. 1719–1722.

[69] S. M. Kay, *Fundamentals of Statistical Signal Processing: Estimation Theory.* Englewood Cliffs, USA: Prentice-Hall Ltd., 1993.

[70] S. Ghael, A. Sayeed, and R. Baraniuk, "Improved wavelet denoising via empirical Wiener filtering," in *SPIE Tech. Conf. Wavelet Applications in Signal processing*, 1997.

[71] M. K. Mihcak, I. Kozintsev, and K. Ramchandran, "Low-complexity image denoising based on statistical modeling of wavelet coefficient," *IEEE Signal Processing Letters*, vol. 6, pp. 300–303, 1999.

[72] M. Kazubek, "Wavelet domain image denoising by thresholding and Wiener filtering," *IEEE Signal Processing Letters*, vol. 10, pp. 324–326, 2003.

[73] A. Hanssen and T. A. Oigard, "The normal inverse Gaussian distribution for heavy-tailed processes," in *Proc. IEEE-EURASIP Workshop on Nonlinear Signal and Image processing*, 2001.

[74] M. I. H. Bhuiyan, M. O. Ahmad, and M. N. S. Swamy, "A new method for denoising of images in the dual-tree complex wavelet domain," in *Proc. of NEWCAS*, 2006, pp. 75–79.

[75] Diethelm Wuertz and many others. fBasics: Rmetrics - Marketes and Basic Statistics . [Online]. Available: http://cran.r-project.org/src/contrib/Descriptions/fBasics.html.

[76] J. P. Nolan. Information on stable distributions. [Online]. Available: http://academic2.american.edu/~jpnolan/stable/stable.html.

[77] J. R. Michael, "The stabilized probability plot," *Biometrika*, vol. 70, pp. 11–17, 1983.

[78] J. Press, *Applied Multivariate Analysis I.* Krieger, Malabar, FL, 1982.

[79] F. Sattar, L. Floreby, G. Salomonsson, and B. Lovstrom, "Image enhancement based on a nonlinear multiscale method," *IEEE Trans. on Image Processing*, vol. 6, pp. 888–895, 1997.

[80] M. I. H. Bhuiyan, M. O. Ahmad, and M. N. S. Swamy, "Wavelet-based despeckling of medical ultrasound images with the symmetric normal inverse Gaussian prior," in *Proc. of ICASSP*, 2007, pp. 721–724.

[81] ——, "Spatially-Adaptive thresholding in wavelet domain for despeckling of ultrasound images," *Submitted to IET Image Processing*, 2007.

[82] ——, "On the performance of non-gaussian distributions in modelling the wavelet coefficients of medical ultrasound images," in *Proc. of IEEE International Conference on Electronics, Circuits and Systems (Accepted)*, 2007.

[83] J. W. Goodman, "Some fundamental properties of speckle," *Journal of Optical Society of America*, vol. 66, pp. 1145–1150, 1976.

[84] T. Eltoft, "Modeling the amplitude statistics of ultrasonic images," *IEEE Trans. on Medical Imaging*, vol. 25, pp. 229–240, 2006.

[85] M. N. Do and M. Vetterli, "Wavelet-based texture retrieval using generalized Gaussian density and Kullback-Leibler distance," *IEEE Trans. on Image Processing*, vol. 11, pp. 146–158, 2001.

[86] M. Simard, G. Degrandi, K. P. B. Thomson, and G. B. Benie, "Analysis of speckle noise contribution on wavelet decomposition of SAR images," *IEEE Trans. on Geoscience and Remote Sensing*, vol. 36, pp. 1953–1962, 1998.

[87] I. W. Selesnick, R. G. Baraniuk, and N. Kingsbury, "The dual-tree complex wavelet transform-A coherent framework for multiscale signal and image processing," *IEEE Signal Processing Magazine*, vol. 22, pp. 123–151, 2005.

[88] A. F. Abdelnour and I. Selesnick, "Symmetric nearly shift invariant tight frame wavelets," *IEEE Trans. on Signal Processing*, vol. 1, pp. 231–239, 2005.

[89] O. V. Michailovich and A. Tanenbaum, "Despeckling of medical ultrasound images," *IEEE Trans. on Ultrasonics, Ferroelectrics, and Frequency Control*, vol. 53, pp. 64–78, 2006.

[90] M. I. H. Bhuiyan, M. O. Ahmad, and M. N. S. Swamy, "New spatially adaptive wavelet-based method for the despeckling of medical ultrasound images," in *Proc. of ISCAS*, 2007, pp. 2347–2350.

[91] N. Kingsbury, "Image processing with complex wavelets," *Philos. Trans. R. Soc. London A*, vol. 357, pp. 2543–2560, 1999.

[92] Aleksandra Pizurica. Wavelet domain image denosing software. [Online]. Available: http://telin.rug.ac.be/~sanja/.

[93] J. Fadili and L. Boubchir, "Analytical form for a Bayesian wavelet estimator of images using the Bessel k form densities," *IEEE Trans. Image processing*, vol. 14, pp. 231–240, 2005.

[94] L. Sendur and I. W. Selesnick, "Bivariate shrinkage with local variance estimation," *IEEE Signal Processing Letters*, vol. 9, pp. 438–441, 2002.

[95] ——, "Bivariate shrinkage functions for wavelet-based denoising exploiting interscale dependency," *IEEE Trans. on Signal Processing*, vol. 50, pp. 2744–2756, 2002.

[96] L. Zhang and P. Bao, "Denoising by spatial correlation thresholding," *IEEE Trans. on Circuits and Systems for Video Technology*, vol. 13, pp. 535–538, 2003.

[97] J. Portilla, V. Strela, M. J. Wainwright, and E. P. Simoncelli, "Image denoising using scale mixtures of Gaussians in the wavelet domain," *IEEE Trans. on Image Processing*, vol. 12, pp. 1338–1351, 2003.

[98] A. Achim and E. Kuruoglu, "Image denoising using a local bivariate α-stable distribution in the complex wavelet domain," *IEEE Signal Processing Letters*, vol. 12, pp. 17–20, 2005.

[99] A. Pizurica and W. Philips, "Estimating the probability of the presence of a signal of interest in multiresolution single and multiband image denoising," *IEEE Trans. Image processing*, vol. 15, pp. 654–665, 2006.

[100] S. M. M. Rahman and M. K. Hasan, "Wavelet-domain iterative center weighted median filter for image denoising," *Signal Processing*, vol. 83, pp. 1001–1012, 2003.

[101] I. K. Eom and Y. S. Kim, "Wavelet-based denoising with nearly arbitrarily shaped windows," *IEEE Signal Processing Letters*, vol. 11, pp. 937–940, 2004.

[102] P. Shui, "Image denoising algorithm via doubly local Wiener filtering with directional windows in wavelet domain," *IEEE Signal Processing Letters*, vol. 12, pp. 681–684, 2005.

[103] M. A. T. Figueiredo and R. D. Nowak, "Wavelet-based image estimation: An empirical Bayes approach using Jeffreyes' noninformative prior," *IEEE Trans. on Image Processing*, vol. 10, pp. 1322–1331, 2001.

[104] X. Li and M. Orchard, "Spatially adaptive denoising under overcomplete expansion," in *Proc. of IEEE Int. Conf. on Image Processing*, 2000, pp. 300–303.

[105] L. Zhang, P. Bao, and X. Wu, "Multiscale LMMSE-based image denoising with optimal wavelet selection," *IEEE Trans. on Circuits and Systems for Video Technology*, vol. 15, pp. 469–481, 2005.

[106] Z. Cai, T. H. Cheng, C. Lu, and K. R. Subramanian, "Efficient wavelet-based image denoising algorithm," *Electronics Letters*, vol. 37, pp. 683–684, 2001.

[107] L. Lin, W. H. Holmes, and E. Ambikairajah, "Speech denoising using perceptual modification of Wiener filtering," *IEE Electronics Letters*, vol. 38, pp. 1486–1487, 2002.

[108] J. Portilla. BLS-GSM Image Denoising. [Online]. Available: http://decsai.ugr.es/~javier/denoise/index.html.

[109] The USC-SIPI image database. University of Southern California, USA. [Online]. Available: http://sipi.usc.edu/services/database/Database.html.

[110] J. C. Naylor and A. F. M. Smith, "Applications of a method for the efficient computation of posterior distributions," *Applied Statistics*, vol. 31, pp. 214–225, 1982.

[111] M. I. H. Bhuiyan, M. O. Ahmad, and M. N. S. Swamy, "Wavelet-based image denoising with the normal inverse Gaussian prior and LMMSE estimator," *Provisionally accepted in IET Image Processing*, 2007.